INFORMATION TO USERS

This manuscript has been reproduced from the microfilm master. UMI films the text directly from the original or copy submitted. Thus, some thesis and dissertation copies are in typewriter face, while others may be from any type of computer printer.

The quality of this reproduction is dependent upon the quality of the copy submitted. Broken or indistinct print, colored or poor quality illustrations and photographs, print bleedthrough, substandard margins, and improper alignment can adversely affect reproduction.

In the unlikely event that the author did not send UMI a complete manuscript and there are missing pages, these will be noted. Also, if unauthorized copyright material had to be removed, a note will indicate the deletion.

Oversize materials (e.g., maps, drawings, charts) are reproduced by sectioning the original, beginning at the upper left-hand corner and continuing from left to right in equal sections with small overlaps.

Photographs included in the original manuscript have been reproduced xerographically in this copy. Higher quality 6" x 9" black and white photographic prints are available for any photographs or illustrations appearing in this copy for an additional charge. Contact UMI directly to order.

ProQuest Information and Learning
300 North Zeeb Road, Ann Arbor, MI 48106-1346 USA
800-521-0600

UMI®

Reproduced with permission of the copyright owner. Further reproduction prohibited without permission.

A

MULTIRESOLUTION APPROACHES FOR IDENTIFYING ANATOMICAL STRUCTURES

by

Yongqing Xiang

A dissertation submitted to the Graduate Faculty in Computer Science in partial fulfillment of the requirements for the degree of Doctor of Philosophy, The City University of New York.

2001

UMI Number: 3008885

Bell & Howell Information and Learning Company
300 North Zeeb Road
P.O. Box 1346
Ann Arbor, MI 48106-1346

This manuscript has been read and accepted for the Graduate Faculty in Computer Science in satisfaction of the dissertation requirement for the degree of Doctor of Philosophy.

4/17/2001
Date

Theodore Raphan
Chairman of Examining Committee

4/18/2001
Date

Executive Officer

Professor Michael Anshel

Professor Bernard Cohen

Dr. Mitchell Schaffler

Professor John Simpson

Professor Theodore Raphan (Advisor)

Professor George Wolberg

Supervisory Committee

The City University of New York

Abstract

MULTIRESOLUTION APPROACHES FOR IDENTIFYING ANATOMICAL STRUCTURES

by

Yongqing Xiang

Advisor: Professor Theodore Raphan

One approach to understanding human and animal behavior rests on the visual identification of anatomical structures that relate structural patterns to development, adaptation, physiology, and function. In the study of stained brain sections, the goal is to visually identify neuro-anatomical nuclei and sub-nuclei. This identification is often made based on personal expertise in the area, and is subject to great inter-observer variability. In many instances, stained anatomical images are identified within a localized region by size, shape and distribution of elemental structures. These properties are closely linked to localized texture, which is presumably used as a measure for identifying anatomical structures. In this research, we investigated the identification of neuro-anatomical structure using a multiresolution approach based on Gabor wavelet transform.

This transform was utilized because of its inherent dependence on orientation of the structural elements, its spatial localization and the fact that local texture can be extracted.

A multiresolution texture feature vector was constructed which consists of localized texture energies along different orientations and under different scales. Based on this texture energy feature, brain scan images were segmented using partitional clustering in the feature space. The characteristics of the cluster center could be viewed as a quantitative property of the underlying anatomical structure it represents. We have been able to identify the abducens and the vestibular nuclei in brainstem images. By using a revised texture feature, which uses the mean texture energy and standard deviation within each frequency band, we have been able to further segment a nucleus into sub-regions. Cluster relaxation and other performance enhancement techniques were implemented in order to make the system a potential tool for identifying, segmenting and quantifying anatomical structures. As a further demonstration of the wide range of applicability of the method in discriminating orientation, anatomical structures related to bone have been assessed as an avenue for future research. Results indicate that the texture features we defined may be important for anatomical analysis where texture is important for understanding the underlying anatomical organization.

ACKNOWLEDGEMENTS

I would like to express my deepest gratitude to my mentor, Professor Theodore Raphan, for his guidance and encouragement throughout the course of this research. I am particularly grateful for the many hours of technical discussions with him and the valuable suggestions he has made to this study, including the choice of this interesting research area, and his meticulous attention to the details in the writing of this thesis.

I would also like to thank all the members of my doctoral examination committee, Professors Mike Anshel (City College), Bernard Cohen (Mt. Sinai School of Medicine), John I. Simpson (New York University Medical School), George Wolberg (City College), and (Dr. Mitch Schaffler, Mount Sinai School of Medicine) for the time and effort each has taken to read and give constructive comments.

A number of individuals provided valuable help to make this study possible, which are greatly appreciated. In particular, Dr. Jean Buettner provided the initial sample images of neural tissues, which were instrumental in this study. Her insightful expertise in neuroanatomy also gave me the initial constraints on which to base the texture-based approach. Dr. Sergei Yakushin provided a set of slides of monkey brain, so that we can test the system with our own images. Dr. Mitch Schaffler gave us important information and suggestions to help this study extend its application to bone structure analysis. He gave us bone slides, which we scanned and subjected to the wavelet analysis. I would also like to thank Dr. Vanessa Yingling for many helpful discussions regarding the structure of bone.

I would especially like to thank Dr. Bernard Cohen for his encouragement and suggestions, especially in the early stages of the work, when the ideas for this work were first being formulated.

I would also like to thank Dr. Stanley Habib and Dr. Ted Brown, past and present Executive Officers of the Computer Science department of the Graduate Center of CUNY and Dr. Aaron Tenenbaum, Chairman of the Department of Computer and Information Science at Brooklyn College of CUNY for their support during the course of this study. The fellowship support from the Graduate Center and the tuition support from Brooklyn College were instrumental in helping me support myself during the course of this work.

I would especially like to thank my wife, Jing Shuai, for her irreplaceable help and support throughout the course of this work and my dear son William, who was born this past year and who has brought both joy and encouragement to my life.

Finally, I would like to acknowledge the financial support of the National Institute of Health under grants DC03284 (National Institute of Communicative Disorders and Stroke, NICDS), EY 04148 (National Eye Institute), and PSC-CUNY grant 6243600.

TABLE OF CONTENTS

LIST OF TABLES X

LIST OF ILLUSTRATIONS XI

CHAPTER 1. INTRODUCTION 1

CHAPTER 2. BACKGROUND 8

2.1 NEURO-ANATOMICAL STRUCTURES AND THEIR TEXTURAL FEATURES 8

2.2 TEXTURE ANALYSIS 17

2.3 SEGMENTATION OF TEXTURED IMAGES 24

CHAPTER 3. TEXTURE SEGMENTATION BASED ON GABOR WAVELETS 34

3.1 WAVELET TRANSFORM 34

3.1.1 Gabor Wavelet Transform 40

3.2 MULTI-RESOLUTION TEXTURE FEATURE SELECTION 49

3.2.1 Filter Selection 50

3.2.2 Features Using Texture Energy 53

3.2.3 Features Exploring Cell Distribution Patterns 56

3.3 SEGMENTATION BASED ON PARTITIONAL CLUSTERING 58

CHAPTER 4. IMPLEMENTATION ISSUES AND PERFORMANCE ENHANCEMENT 63

4.1 INTRODUCTION 63

4.2 MULTI-RESOLUTION IMPLEMENTATION AND COMPUTATIONAL EFFICIENCY 65

4.3 TEXTURE ENERGY ADJUSTMENT FOR NON-TEXTURED REGION BORDER 70

4.4 RELAXATION 76

4.4.1 Additional Features for Relaxation 76

4.4.2 Probabilistic Relaxation Labeling 77

CHAPTER 5. RESULTS 81

5.1 RESULTS APPLIED TO SIMULATED TEXTURE PATTERNS 81

5.1.1 Discriminating Properties of the Gabor Texture Feature *81*

5.1.2 Selecting the Highest Center Frequency *86*

5.1.3 Effects of Cell Shape on Texture Discrimination *89*

5.2 TEXTURE DISCRIMINATION OF THE ABDUCENS NUCLEUS 91

5.2.1 Identification of the Abducens Nucleus *91*

5.2.2 Effects of Orientation Resolution on Texture Discrimination *105*

5.2.3 Reconstruction of the Original Texture with Texture Features *106*

5.3 APPLICATION TO SEQUENCES OF BRAINSTEM IMAGES 109

5.3.1 Identification of the Abducens Nucleus *111*

5.3.2 Identification of the Vestibular Nuclei *112*

CHAPTER 6. APPLICATION OF TEXTURE FEATURE ANALYSIS TO UNDERSTANDING BONE STRUCTURE **144**

6.1 BACKGROUND 144

6.2 RESULTS 150

CHAPTER 7. CONCLUSION AND DISCUSSION **153**

7.1 CONTRIBUTION OF THE DISSERTATION 153

7.2 DISCUSSION ABOUT THE QUANTIFYING PROPERTIES OF THE TEXTURE FEATURE 154

7.2.1 Interpretation of the Texture Feature *155*

7.2.2 A Distance Definition for Comparing Feature Patterns *157*

7.2.3 A General Approach to the Textured Image Representation *160*

7.3 FUTURE RESEARCH 162

APPENDIX **163**

A. THE BASIC STRUCTURE OF THE COMPUTER PROGRAM 163

BIBLIOGRAPHY **166**

LIST OF TABLES

Table 4.1 Computation time when no multi-resolution implementation was used 69

Table 4.2 Computation time when multi-resolution implementation was used 69

Table 4.3 Filter size and image size comparisons between implementations with and without multi-resolution 69

Table 5.1 Data set of the first segmentation of the sample image "TAZ1437L" 95

Table 5.2 Data set of the second segmentation of the sample image "TAZ1437L" 97

Table 7.1 The combined distance of texture feature between the marked regions in each slide 159

Table A.1 Some of the Tseg classes and the summary of their functionality 164

LIST OF ILLUSTRATIONS

Fig. 2.1 Schematic diagram of the monkey brain 12

Fig. 2.2A Abducens nucleus in monkey brain 13

Fig. 2.2B Abducens nucleus in monkey brain, continued 14

Fig. 2.3A Vestibular nuclei in monkey brain 15

Fig. 2.3B Vestibular nuclei in monkey brain, continued 16

Fig. 2.4 The divided Fourier domain for angular and radial discrimination 23

Fig. 3.1 Illustration of a Gabor filter 43

Fig. 3.2 The Gabor filter set with half-peak support in the frequency domain 44

Fig. 3.3 A diagram illustrating the determination of σ_u and σ_v 45

Fig. 3.4 The effects of $tanh(x)$ 54

Fig. 3.5 An Overview of the texture segmentation algorithm 61

Fig. 3.6 Flowchart of the K-mean data clustering algorithm 62

Fig. 3.7 The criterion for clustering convergence 62

Fig. 4.1 The Nikon Eclipse E400 microscope with the MTI NC-81LX video camera mounted on the top 64

Fig. 4.2 The Gabor filtering scheme without considering computational efficiency 67

Fig. 4.3 The modified scheme exploring the multi-resolution nature of the Gabor filters 68

Fig. 4.4 Flow-chart of the blob-coloring algorithm 72

Fig. 4.5 Illustration of the orientational difference of texture energy along the border of textured and non-textured regions 73

Fig. 4.6 Result of the texture energy adjustment along the border region 76

Fig. 4.7 Effects of the probabilistic relaxation 80

Fig. 5.1 Four panels of simulated images of different cell distributions 84

Fig. 5.2A A plot of the texture energy comparison between panel (A) and (B) 85

Fig. 5.2B A plot of the texture energy comparison between panel (A) and (C) 85

Fig. 5.2C A plot of the texture energy comparison between panel (A) and (D) 86

Fig. 5.3 Choosing the appropriate starting high frequency band 88

Fig. 5.4 Effects of the cell shapes on texture feature 90

Fig. 5.5 Sample image "TAZ1427L" showing abducens nucleus and surrounding neural tissues 93

Fig. 5.6 Analysis and segmentation result of the sample image "TAZ1437L" 94

Fig. 5.7 Plot of the averaged texture feature of individual regions in Fig. 5.6(B), as the function of feature order 95

Fig. 5.8 Segmentation without the added features of the Gaussian smoothed pixel intensities 96

Fig. 5.9 Result of the second level segmentation of the sample image "TAZ1437L" 97

Fig. 5.10 Plot of the averaged texture features of the two sub-regions in Fig. 5.9 98

Fig. 5.11 Further subdivisions of the abducens nucleus 100

Fig. 5.12 Segmentation result of the sample image "TAZ1436R" 101

Fig. 5.13 Segmentation result of the sample image "TAZ1437X" 102

Fig. 5.14 Segmentation result of the sample image "TAZ1439L" 103

Fig. 5.15 Another view of the segmentation result of Fig 5.6, while tiny small regions (pixel count < 300) were sifted out 104

Fig. 5.16 Effects of higher orientation resolution on segmentation result 105

Fig. 5.17 Reconstruction of the original image from the output directly after Gabor wavelet transform 107

Fig. 5.18 Reconstruction of the original image from the data after the *tanh*() nonlinear transform 108

Fig. 5.19 Reconstruction of the original image from the data after taking the absolute values 108

Fig. 5.20 Reconstruction of the original image from the texture feature after the Gaussian feature smoothing 109

Fig. 5.21A~B Original images for slide #180 116

Fig. 5.21C~D Segmentation and data plot for slide #180 117

Fig. 5.22A~B Original images for slide #185 118

Fig. 5.22C~D Segmentation and data plot for slide #185 119

Fig. 5.23A~B Original images for slide #190 120

Fig. 5.23C~D Segmentation and data plot for slide #190 121

Fig. 5.24A~B Original images for slide #195 122

Fig. 5.24C~D Segmentation and data plot for slide #195 123

Fig. 5.25A~B Original images for slide #200 124

Fig. 5.25C~D Segmentation and data plot for slide #200 125

Fig. 5.26A~B Original images for slide #205 126

Fig. 5.26C~D Segmentation and data plot for slide #205 127

Fig. 5.27A~B Original images for slide #210 128

Fig. 5.27C~D Segmentation and data plot for slide #210 129

Fig. 5.28A~B Original images for slide #215 130

Fig. 5.28C~D Segmentation and data plot for slide #215 131

Fig. 5.29A~B Original images for slide #220 132

Fig. 5.29C~D Segmentation and data plot for slide #220 133

Fig. 5.30A~B Original images for slide #225 134

Fig. 5.30C~D Segmentation and data plot for slide #225 135

Fig. 5.31A~B Original images for slide #230 136

Fig. 5.31C~D Segmentation and data plot for slide #230 137

Fig. 5.32A~B Original images for slide #235 138

Fig. 5.32C~D Segmentation and data plot for slide #235 139

Fig. 5.33A~B Original images for slide #245 140

Fig. 5.33C~D Segmentation and data plot for slide #245 141

Fig. 5.34 The 5× magnification image of the abducens nucleus in slide #195 142

Fig. 5.35 The first level segmentation of Fig. 5.34 142

Fig. 5.36 The second level segmentation inside the abducens nucleus in Fig. 5.35 143

Fig. 6.1 Schematic of a long bone shaft and anatomy of cortical and trabecular bone 147

Fig. 6.2 Types of bone 148

Fig. 6.3 Bone samples showing predominantly orientational difference 151

Fig. 6.4 Bone samples showing predominantly density difference 151

Fig. 6.5 Difference in texture energy pattern of the two bone samples shown in Fig. 6.3 152

Fig. 6.6 Difference in texture energy pattern of the two bone samples shown in Fig. 6.4 152

Fig. 7.1 A quad-tree representation of textured image 161

Fig. A.1 Structural diagram of the Tseg application 165

CHAPTER 1. INTRODUCTION

An important purpose of anatomical investigation is to determine how anatomical structure is related to biological function under normal and pathological conditions. Anatomical investigations generally require visual examination of images obtained from Computerized Tomography (CT), Magnetic Resonance Imaging (MRI), as well as viewing sections of tissues after they have been prepared by fixatives and staining. These tissue sections may be at the light or electron microscopic level. The large amount of work done on low and high level image processing and analysis [1-4] offers the possibility of developing automated aids to anatomical investigation and giving objective measures of anatomical structure. Much work has been done in the application of image processing and computer vision techniques to CT scans and MRI [5, 6]. These applications are mainly concerned with identifying boundaries of gross anatomical structures such as the imaging of the heart [7], or detection of lesions in the brain [8]. Much less has been done in the application of these medical informatic methodologies to helping anatomists study anatomical structures where no clear anatomical boundaries are defined.

One important example is the identification of neuro-anatomical nuclei that give information about the function of the brain [9]. The neuro-anatomical techniques that have been developed can broadly be divided into light-microscopic and electron-microscopic methods. The image formations rely on the property that various parts of cells absorb stains to varying degrees and which can then be used to obtain information about anatomical structure at different levels. The most common early staining method utilized in light-microscopic techniques were the *Golgi* method, which uses a silver nitrate stain and the *Nissl* method, which uses basic aniline dyes for staining. It is believed that silver binds to the filamentous proteins within the cytoplasm of a cell. Therefore, the silver nitrate used in the *Golgi* method, not only stains the cell body but the dendrite and axon as well. While the *Golgi* stain fills the cell body, dendrite, and axon almost completely, it affects only about five percent of cells [10]. More modern approaches inject dye into a single neuron or use recombinant DNA techniques [10]. Examination of the stained tissue under a microscope by a trained neuro-anatomist has given information about the detailed morphology of cells, their axons and dendrites.

Other methodologies that utilize histological dyes such as toluidine blue, cresyl violet, and methylene blue to stain the ribonucleic acids of the ribosome in the cell body also give useful image information [11]. These dyes, utilized in the *Nissl* method afford the possibility of identifying the cellular organization of the gray matter and localizing the distribution of cells in a particular nucleus. Histo-chemical methods are used to determine the chemical and metabolic constituents of nerve cells by exploiting the capacity for neurotransmitters, receptor molecules and enzymes to fluoresce. There are other methods, which explore the connections between regions of nervous system. They include: *axon transection*, which exploits neuronal structural changes after cutting axon, and *axonal transport*, in which certain chemicals or fluorescent dyes are injected and either anterogradely or retrogradely transported to trace the fiber connection [12]. In particular, the method using retrograde axonal transport of horseradish peroxidase (HRP) has been valuable in subdividing a known nucleus (abducens) into different functional categories [13]. Generally, these methods can also be utilized in conjunction with the electron microscope to provide fine structural details of the nervous system. While the various staining techniques contain enormous information about the organization of the central nervous system, identifying nuclear groups from brain sections is still qualitative and requires substantial expertise in order to delineate different groups based on their visual appearance.

Recent advances in digital image capturing make it now feasible to have high-resolution micrographs which can be analyzed by computer [14]. Such micrographs are now commonly used by neuro-anatomists in the analysis of brain tissue, but still require hand analysis and qualitative judgements. Thus, despite the development of advanced neuro-anatomical techniques that generate images to help us understand the structure of the central nervous system and the availability of high speed computers to sample these images with relatively high resolution, automated methodologies to process and analyze these types of images have not been fully explored. One reason for this continued use of qualitative approaches even with computers is that no algorithmic procedure has been developed to mimic the judgements used by the anatomist.

These qualitative approaches could be enhanced by defining specific quantitative criteria based on the judgements generally used by anatomists. In this way, a methodology could be developed which transforms qualitative judgements into quantitative assignments of anatomical structures. For example, in *Nissl* stained material of the abducens nucleus, the dominant criteria for identifying cell groups would be (Dr. Jean Buettner, Personal communication): 1) the density of cell spacing, 2) the regularity of cell spacing, 3) The size of the cells, and 4) The location of the cells. The question then arises: can we develop a methodological approach that encompasses these criteria and transforms them into quantitative attributes that will define the structure of the nucleus? One simple way in which to analyze neuro-anatomical images is to view the criteria used by neuro-anatomists in identifying nuclear groups as a problem of identifying and categorizing texture. Texture represents essentially a spatial distribution of gray levels in a localized region and encompasses attributes such as density of cells, size of cells, and regularity of spacing. Therefore, an understanding of the distribution of texture as a function of position in neuro-anatomical images should give us information about the organization of nuclear groups.

Another example where imaging of anatomical tissue has been important in establishing a correlation between structure and function is in the area of bone analysis [15, 16]. The various construction and organization of the bone elements contribute to the biological and mechanical quality of the bone. In particular, the architecture of the trabecular network has been found to be highly correlated with the strength and other biomechanical characteristics of the bone [16]. The traditional bone histomorphometry is based on stereology, which measures two-dimensional sections by statistical sampling [17]. Although the measurements in many ways precisely represent some aspects of bone structure, it is very difficult to describe bone architectures directly and completely. Particularly, we are interested in how trabecular bone is organized, which is characterized by the interrelationship of rod-like struts of varied shapes and orientations. It is believed that, in the process of bone remodeling, the orientation of the trabeculae can be rapidly altered to accommodate changes in loading or shifts in alignment as the results of disease or fracture [18]. The measurement of these morphological forms in a quantitative way would provide information to facilitate the research of the biomechanical properties of bone, and to assist the diagnosis of bone diseases such as osteoporosis. Nevertheless, a direct measure of orientation has not yet been established. Since the appearances of cancellous bone elements are characterized by the variable density and orientation of trabeculae, when captured through a camera, the microscopic image of bone section takes on the form of a unique texture. Thus, we questioned whether texture based algorithms would also help in quantifying the organization of the trabecular bone network.

Since the structural analysis of both neural tissue and bone can be transformed into texture analysis in the image-processing domain, we can focus on the latest development in texture analysis techniques. An important approach in texture analysis in recent years has been the characterization of texture using multi-resolution techniques, particularly the localized spatial filters and the wavelet transform [19-25]. Wavelet transform is essentially a multi-resolution filtering technique. When the appropriate filters (wavelets) are used, the original image can be decomposed into different channels which contain spatially localized, scale and orientation selective frequency contents. This joint spatial/spatial-frequency representation given by the wavelet transform provides significant insight into the texture composition of the original image, which is not self-evident with other methods.

Recently, studies have focused on the cytoarchitecture of cells based on texture properties [26, 27]. However, to the best of this author's knowledge, there has been no work on segmenting neuronal nuclei of brain tissues at the light microscopic level. One purpose of this research was to establish an analytical framework and a practical system for developing an anatomical image analysis system. The system will utilize Gabor wavelet based texture feature together with spatial constraints to segment neural images into regions where specific nuclear groups (nuclei) can be identified. For nuclear groups that have similar texture components but are spatially disjoint, the spatial components of the feature vector help separate them effectively. In this thesis, the segmentation techniques were applied to identify the nuclear groups associated with the oculomotor and vestibular systems. In addition, the texture feature has been applied to bone structure analysis, where it proved to give effective information about the density and orientation of various bones and helped distinguish bone structures under normal and pathological conditions.

The organization of the thesis is as follows: In Chapter 2 (the background), we consider the texture properties associated with neuro-anatomical structures, and give a review of texture analysis methods. In Chapter 3, we derive a texture segmentation algorithm based on a texture feature derived from Gabor wavelets. A two-level segmentation scheme has been developed using partitional clustering. The first level segmentation will separate nuclei from other brain tissues, and the second level segmentation will utilize a different texture feature which better characterizes cell distributions so that sub-nuclei can be more readily recognized. While the basic concepts of using Gabor filter in texture analysis have been the subject of various studies, the design of the Gabor filter parameters varies depending on the application. In Chapter 4, we derive and implement a Gabor wavelets system for the neuronal nuclear group segmentation application. We derive the formula for determining the Gabor filter parameters and develop a heuristically based criterion to determine the highest frequency level for applying the Gabor wavelets. We also show how to enhance the implementation of the wavelet expansion algorithm to take advantage of the multiresolution property, so that the speed of the feature generation is greatly improved over standard methods. In addition, we developed a texture energy adjustment scheme so that the boundary between textured and non-textured (solid gray level) regions can be more accurately localized. Chapter 5 shows the results of our method applied to simulated image and practically obtained anatomical image that contain the abducens nucleus and the vestibular nuclei. In chapter 6, we consider features of bone anatomy and show that this method is also potentially important for giving information about orientation and structure of bone tissue. Conclusion, discussion and suggestion for future research are given in Chapter 7.

CHAPTER 2. BACKGROUND

2.1 Neuro-anatomical Structures and Their Textural Features

Neurons are the basic cells of the nervous system that are responsible for receiving and transmitting nerve impulses that innervate other cells such as the sensory and motor cells that are responsible for behavior. A nerve cell consists of a cell body, which contains a nucleus, and axons and dendrites extending from the body. The dendrites are the multi-branched portions that receive impulses, while the axons are the elongated structures that carry the impulse away from the body of the cell. Neurons transmit their impulses across nerve connections (synapses) using a neurotransmitter chemical.

The neurons of the brain can be classified functionally into three major groups: sensory, motor, and inter-neuronal. Sensory neurons carry information into the nervous system. Motor neurons carry commands to muscles and glands. All remaining cells are inter-neurons which process information locally or convey information from one site within the nervous system to another [11]. The number of neurons constituting the central nervous system is on the order of 100 billion. They are not distributed randomly, but rather clustered into discrete cellular groups called *nuclei*. The structures of these nuclei contribute to determining their functions and can tell us something about the behavior of the organism. Nuclear structure is determined by the size and shape as well as the distribution of the cells making up the nucleus.

To anatomically describe these structures, they have been represented by coordinates related to placing an animal in a stereotaxic apparatus, which holds the head rigidly by ear bars placed into the auditory miatus and bars placed between the teeth (Fig. 2.1, [28]). The horizontal plane is comprised of the interaural axis, i.e., axis through the ears, and an axis through the mouth and orthogonal to the interaural axis (Fig. 2.1). The vertical line at zero (Fig. 2.1) represents a vertical plane that contains the interaural axis. The horizontal line at zero (Fig. 2.1) represents a horizontal plane 10-mm above the interaural axis. The intersection of these two planes is a line parallel to the interaural axis and 10 mm above it. The intersection of this line with the midsagittal plane (a vertical plane whose normal is along the interaural axis and divides the brain into two approximately equal parts) is a point representing the origin of this stereotaxic coordinate frame. The anterior direction (A) is toward the front of the brain and the posterior direction (P) is toward the back (Fig. 2.1).

One area where function and structure is fairly well understood is the sensori-motor behavior of the vestibulo-ocular reflex (VOR) (See [29], for review) and nuclei related to this reflex will be considered in this dissertation. The angular vestibulo-ocular reflex is governed by a rapid direct pathway, having essentially no dynamics[1], and governed by the classic three-neuron arc [30]. Another pathway, which has slow dynamics and has been designated the indirect pathway, has been associated with velocity storage [31, 32]. The summed activities of these system pathways activate the oculomotor system, which in turn rotates the eyes. The brainstem nuclei that are involved in the generation of the slow phases of the VOR include the vestibular nuclei [33-35] and all of the oculomotor nuclei including the abducens, the third nerve, and the trochlear nuclei. The abducens nucleus activates the lateral rectus muscle, which is responsible for

---

[1] Informally, a system is said to have no dynamics if its input-output relationship can be described by a constant or a constant matrix.

abducting the eye or making it move horizontally away from the nose. The remaining oculomotor nuclei activate the other eye muscles, which are responsible for moving the eyes vertically and in roll (See [34-36], for review). It is becoming increasingly clear that the vestibular nuclei have a wide range of different functional units which have been designated as *vestibular only* (VO) or *vestibular plus saccade* (VPS) [34-36]. The VO neurons are involved in the implementation of velocity storage, while the VPS neurons appear to be involved in VOR function at a later stage of processing [35]. In addition, many of the cells of the vestibular nuclei project to the vestibulo-cerebellum (flocculus and nodulus) and vice versa to implement the spatial orientation aspects of the VOR [37, 38].

These brainstem nuclei are seen with *Nissl* stained images of the brainstem section of rhesus monkey. From P2.0 mm to P3.5 mm, at 9.5 magnification there is a pronounced aggregate of cells, which have been identified as the abducens nucleus (Fig. 2.2A and 2.2B). This cell group has the largest area around P3.0-P4.0 and at a level 3-5 mm below the horizontal zero (Fig. 2.2A and 2.2B). In each of the sections, there is an identifiable textured region (Fig. 2.2A(A,B) and Fig. 2.2B(C,D)), regions described by highlighted labels). Visually, this texture stands out from the immediate surrounding area where the texture is composed of brain tissues without cell formations. Further posterior (Fig 2.3A and 2.3B), the abducens nucleus is no longer identified as a nucleus. Between P5.5 and P8.5, ranging from levels 4-8 mm below the zero horizontal, the superior, medial, lateral and descending vestibular nuclei are identified (Fig. 2.3A and 2.3B). These nuclei are not as well defined spatially and the textural features are not as robust as those of the abducens.

More recently, there has been a re-examination of the organization of cell groups of the paramedian tract (PMT) [39-41]. These are clusters of cells scattered along the midline fiber tracts in the pons and medulla which project to the floccular region [42]. It has been shown that the abducens nucleus has a variety of cell types with at least three different grouping: abducens motoneurons, internuclear neurons, and those that project to the flocculus [13, 41, 43]. Lateral gaze requires contraction of the ipsilateral lateral rectus muscle, which is innervated by the motoneurons, and the contralateral medial rectus muscle, which is controlled to large degree through the internuclear neurons. The command for lateral gaze is transmitted from the abducens nucleus on one side to the part of the oculomotor nucleus on the contralateral side that contains medial rectus motor neurons by internuclear neurons. Thus, it is becoming increasingly clear that what had been thought to be homogeneous populations of neurons are more diverse. Although reconstruction of neural structures of up to hundreds of neurons (and even the reconstruction of sub-cellular organelles) have been done by a hand examination and analysis of images of sections of neural tissue taken with either light or electron microscopy [14], it is not clear that these groups of cells have well defined boundaries. One of the goals of this dissertation was to develop a methodology that will help anatomists to parse the various nuclei and subnuclei.

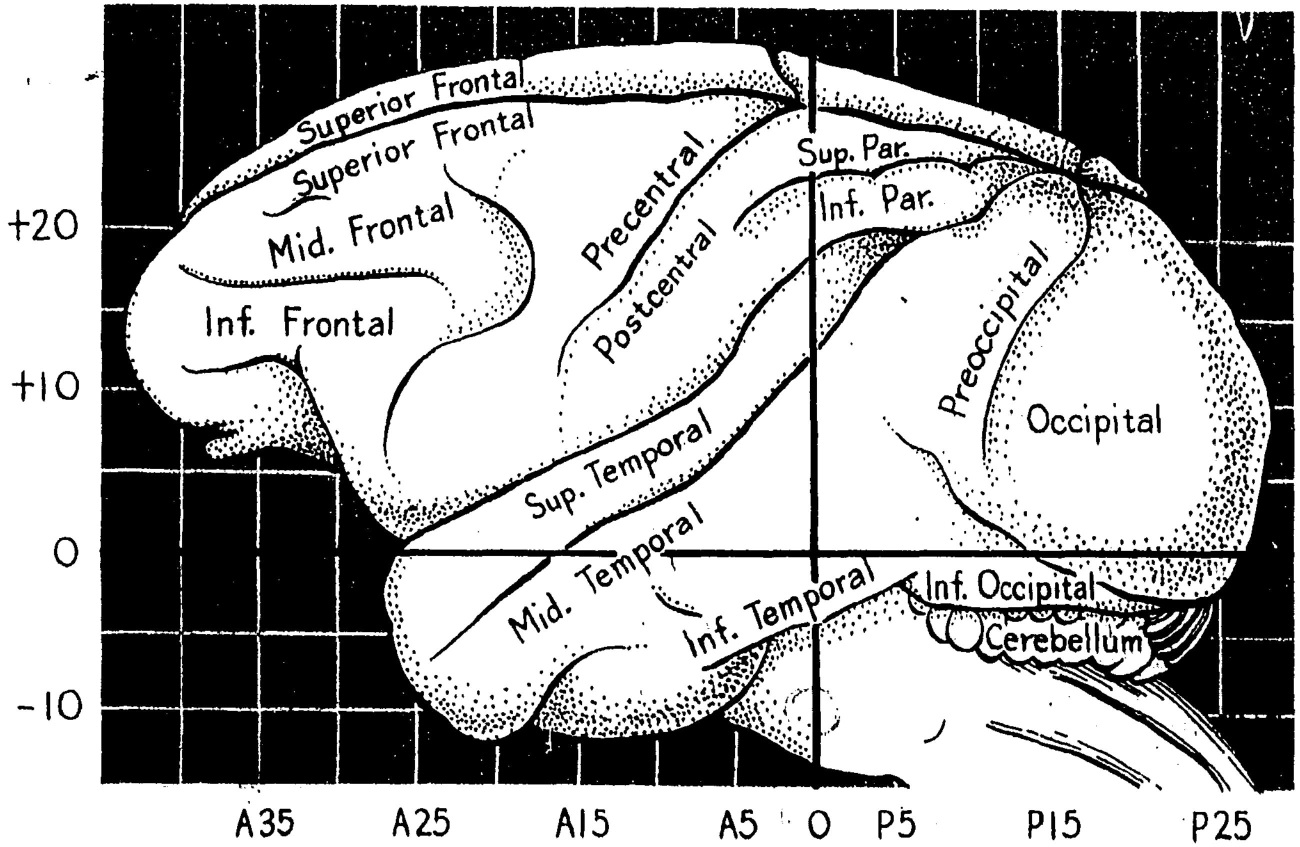

Fig. 2.1 Schematic diagram of the monkey brain showing lateral view with some intentional distortion at the superior surface for purposes of display. The vertical line at zero represents an interaural plane of reference from which plates of the Atlas are numbered anteriorly ("A") and posteriorly ("P") on a millimeter scale at 0.5 mm intervals. The horizontal lines represent planes of reference at right angles to the above. When this co-ordinate is used, the zero position is 10 mm above the interaural line. Each cross-section in the Atlas shows these vertical co-ordinates as well as the other dimension of the three-co-ordinate system, namely the left and right. The latter is expressed as "L" and "R" when related to the midline of the brain. Obviously, this dimension could not be included in this lateral view of the brain. (Taken from [28])

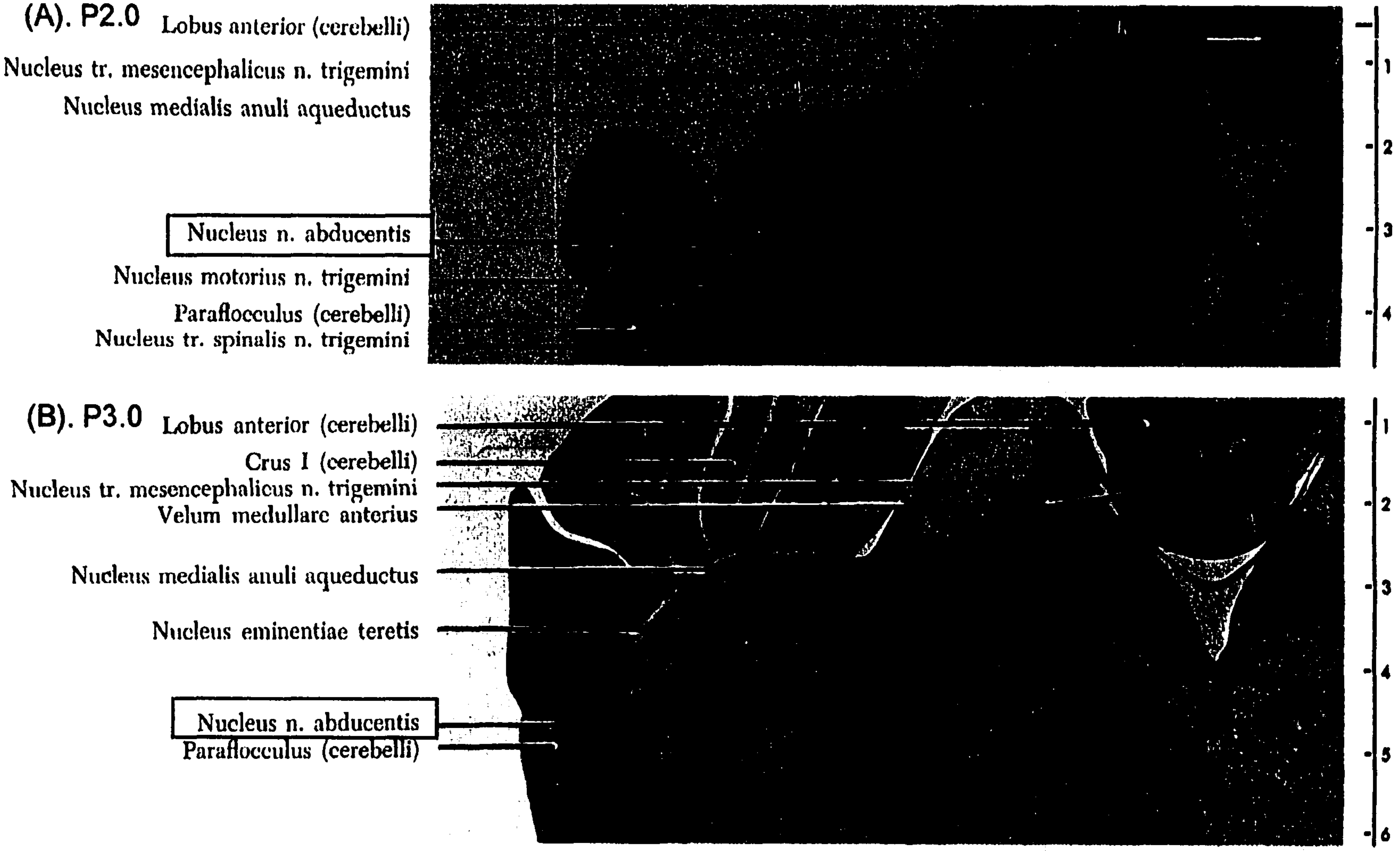

Fig. 2.2A Abducens nucleus in monkey brain (Nissl stained, 9.5 magnification), (A): Posterior 2.0mm, (B): Posterior 3.0mm, all relative to stereotaxic coordinates. (Adapted from [28])

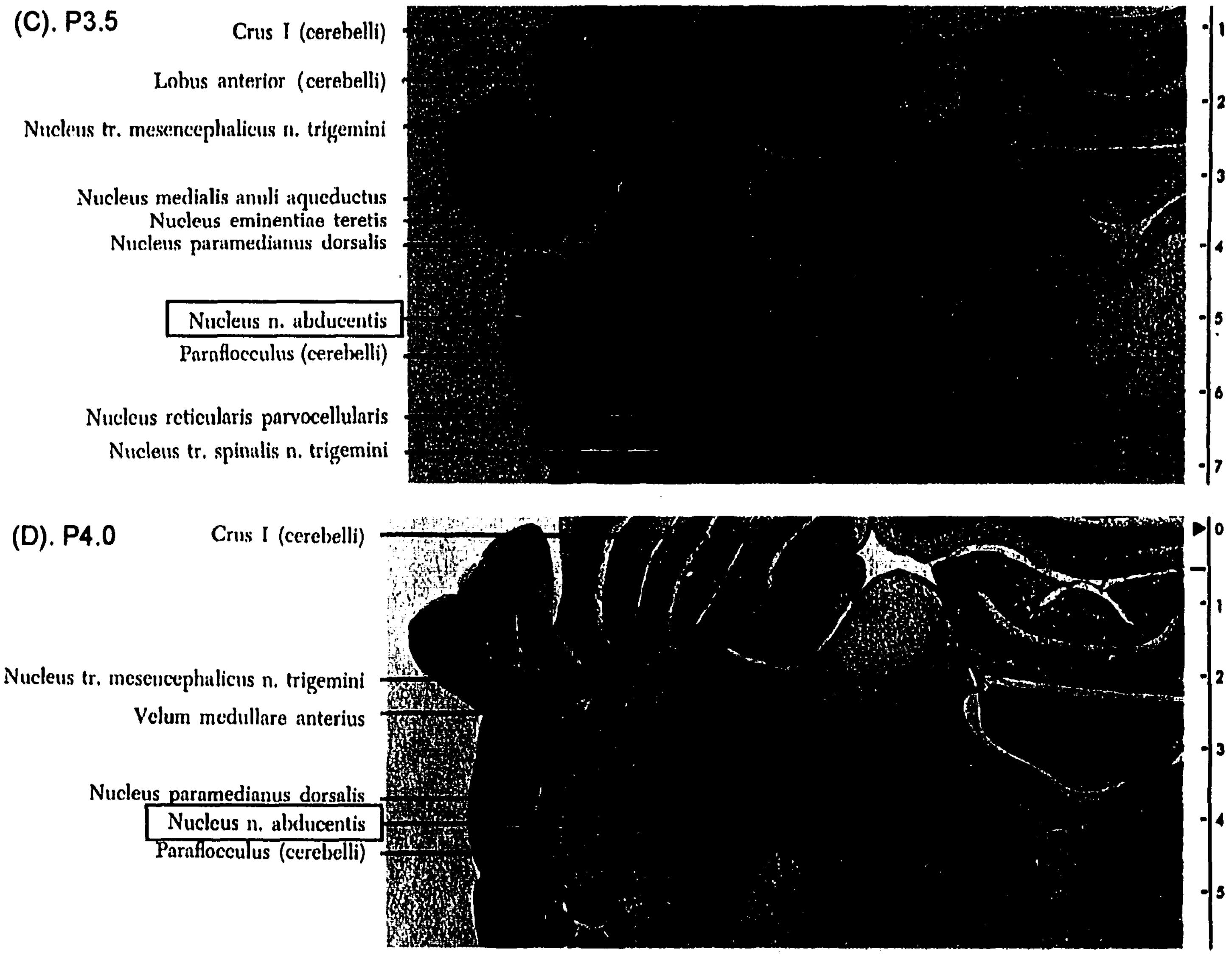

Fig. 2.2B Abducens nucleus in monkey brain, continued (Nissl stained, 9.5 magnification), (C): Posterior 3.5mm, (D): Posterior 4.0mm, all relative to stereotaxic coordinates. (Adapted from [28])

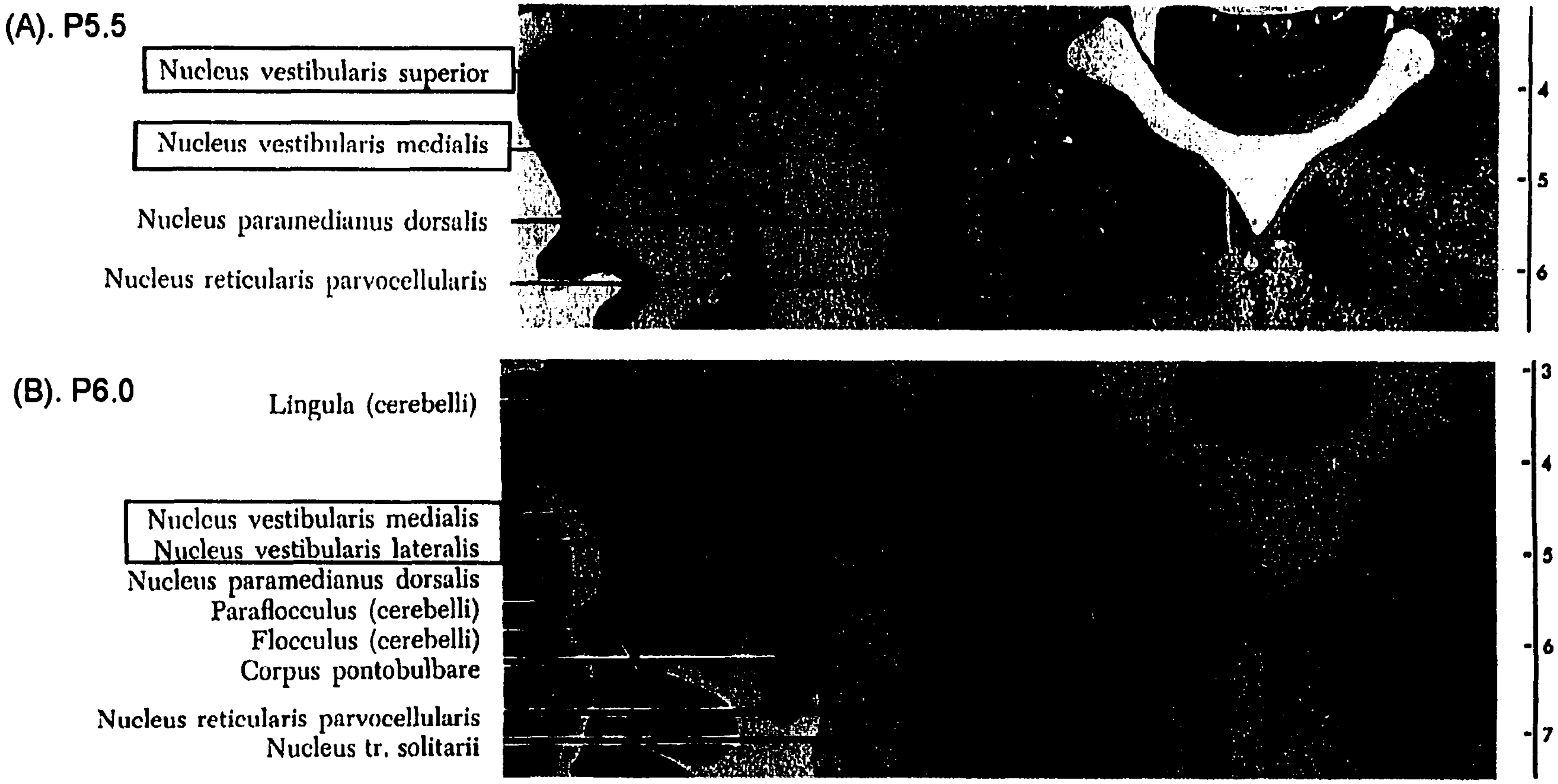

Fig. 2.3A Vestibular nuclei in monkey brain (Nissl stained, 9.5 magnification), (A): Posterior 5.5mm, (B): Posterior 6.0mm, all relative to stereotaxic coordinates. (Adapted from [28])

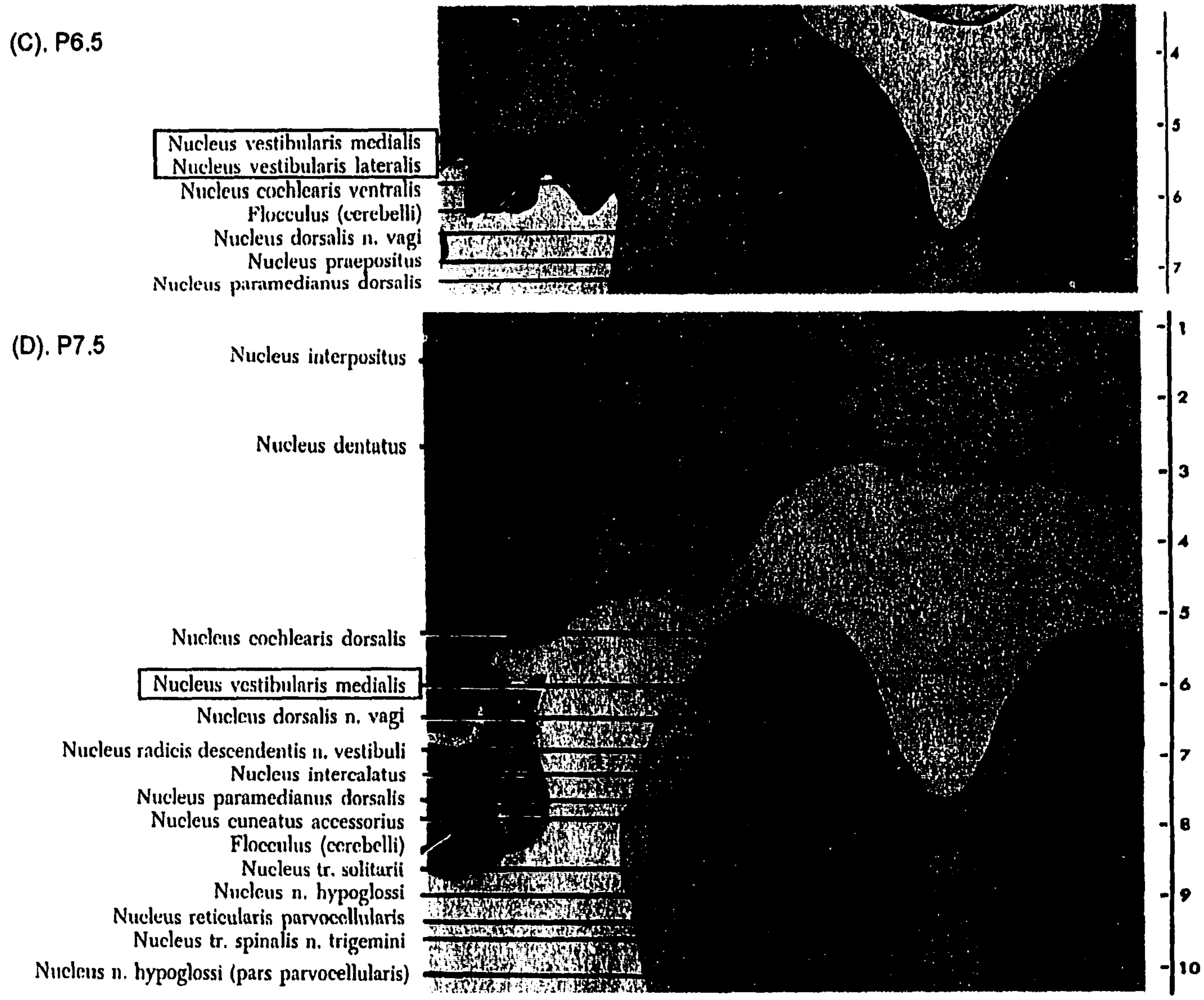

Fig. 2.3B Vestibular nuclei in monkey brain, continued (Nissl stained, 9.5 magnification), (C): Posterior 6.5mm, (D): Posterior 7.5mm, all relative to stereotaxic coordinates. (Adapted from [28])

2.2 Texture Analysis

For an image represented by gray level intensities, texture is defined as "an attribute representing the spatial arrangement of the gray levels of the pixels in a region" [44]. It plays a significant role in facilitating our perception of the shapes of surfaces and their layout in an image. There is a great diversity of textures in real world, some may consist of structured or randomly displaced basic elements, and some may be without fundamental constructing units. Texture with well-defined primitive structure and high regularity is referred to as *strong texture*, while texture without structure or having a structure that is distributed in a random or irregular way, is called *weak texture*. Both strong and weak textures have global and local properties and texture perceived in a global sense is termed macro-texture, while texture perceived in a local sense is termed micro-texture.

To quantify texture, it is necessary to identify texture features that will adequately describe the attribute of the spatial arrangement of gray levels and be able to discriminate between textures [2]. Based on the choice of features, texture analysis has been applied in three general areas: texture classification, texture recognition, and texture segmentation. Texture recognition/classification entails associating a texture with a particular whole image, so that it can be compared with the texture of other images. In this application, the spatial distribution of texture within a given image is not significant. Texture segmentation requires the partitioning of an image into spatial regions, each of which is associated with a particular texture. The texture segmentation problem is the more difficult problem because of the inverse relationship between the ability to characterize texture and the spatial resolution required for optimal segmentation. That is, as the number of pixels is reduced, it is harder to classify a particular texture. A comprehensive survey of texture analysis methods can be found in [45], [46] and [47]. More recent reviews on texture analysis methods can be found in [48] and [49].

Conceptually, methods used in analyzing textures can be categorized roughly into three basic types, the structural methods, the statistical methods, and the spatial/spatial frequency methods. The structural model considers texture to be a result of taking a particular well-defined texture element (*texel*), and repeating or tessellating the texel in an ordered way in accordance with some rules. The texel is defined as a pixel pattern comprising the smallest identifiable building blocks for creating a particular texture. This method of generating texture could be described by a deterministic grammar or placement rules [50]. The texel together with the placement rules can then be used to discriminate among different textures. The scheme can be summarized in the spatial frequency domain as follows:

Given a texture primitive (texel) $p(x, y)$ and placement rules $r(x, y)$, the texture $t(x, y)$ can be defined as:

$$t(x,y) = p(x,y) * r(x,y), \qquad (2.2.1)$$

where

$$r(x,y) = \sum \delta(x - x_m, y - y_n), \qquad (2.2.2)$$

and x_m and y_n are the coordinates of the centers where the texture primitive is located. In the spatial-frequency domain, we have:

$$T(u,v) = P(u,v) \cdot R(u,v), \tag{2.2.3}$$

which gives us,

$$R(u,v) = T(u,v) \cdot P(u,v)^{-1} \tag{2.2.4}$$

Eq. (2.2.4) states that given a description of the texel $p(x, y)$, we can derive the $P(u,v)^{-1}$, and create a convolution filter in the spatial domain. If we convolute this filter with the original image, we should obtain the placement rule, which is characterized by an array of impulses indicating the positions of the centers where texels should be placed.

This kind of analysis model has its limitations. Firstly, it is highly dependent on the number of pixels needed to describe the size and shape of the texel and is highly dependent on the image resolution used. In many instances, it is virtually impossible to identify a texel. In other instances, there could exist ambiguity in choosing texels as it might be possible to describe a texture by more than one choice of texels and accompanying placement rules. In addition, few textures are strictly deterministic and realistic textures tend to exhibit some statistical variations that are hard to model with placement rules. Due to these limitations, structural models are of limited utility and have found few applications.

Attempts to utilize statistical approaches to model texture have received considerably more attention. Statistical models treat texture as a random arrangement of pixel intensities having some statistical distribution. The simple first-order gray-level statistic gives the mean, variance, and all the associated moments for the gray level histogram distribution [51]. This is in contrast to describing the joint statistics of pixel pairs, triples, and groups of *n* pixels. All conceivable first-order statistical measures of an image are determined by the image's gray-level histogram. The fundamental limitation of first-order measures is their insensitivity to pixel permutations and their inability to localize textures for segmentation purposes. Second-order statistics are more advantageous and are more widely used. One of the commonly used methods is based on creating a sequence of gray level co-occurrence matrices [45, 52, 53]. For each matrix, a direction θ and distance d in pixels are established. Then, the element (i, j) of the matrix represents the number of coincidences of the gray levels, i and j, that occur as the image is traversed in the direction and the distance as specified. This number is then normalized with respect to the total number of pixel pairs. The procedure can be described analytically as follows:

Given an image $f(x, y)$ with a set of N_g discrete gray levels, define the co-occurrence matrix $P(i, j, d, \theta)$ such that the (i, j)th entry is the number of times that

$$f(x_1, y_1) = i \tag{2.2.5}$$

and

$$f(x_2, y_2) = j, \tag{2.2.6}$$

where (x_1, y_1) and (x_2, y_2) are pixel pairs related by a Euclidean distance, d, and angle, θ, as follows:

$$(x_2, y_2) = (x_1, y_1) + (d\cos\theta, d\sin\theta). \tag{2.2.7}$$

Since i and j will enumerate all the N_g gray levels, we will have a matrix of the dimension (N_g, N_g), for each distance and orientation pair (d, θ). If we denote $R(d, \theta)$ as the total number of the neighboring pixel pairs that meet the (d, θ) constraint, we can define a number of features that characterize the texture. Two of them are listed here:

entropy,

$$H(d,\theta) = -\sum_{i=1}^{N_g}\sum_{j=1}^{N_g}\frac{P(i,j,d,\theta)}{R(d,\theta)}\log\frac{P(i,j,d,\theta)}{R(d,\theta)} \tag{2.2.8}$$

and *energy,*

$$E(d,\theta) = \sum_{i=1}^{N_g}\sum_{j=1}^{N_g}\left(\frac{P(i,j,d,\theta)}{R(d,\theta)}\right)^2 \tag{2.2.9}$$

It should be noted that these texture features do not localize common texture regions in the image space, but rather give global texture information. This methodology has been adapted for local texture classification by defining the same features for a localized moving window centered on a pixel of interest. This approach raises a problem in choosing the window size, resulting in a trade-off of texture classification performance and determining texture boundary accuracy.

An alternate second-order statistical method, which has been utilized in texture classification, is the gray-level auto-correlation function method. Gray-level auto-correlation coefficient as a function of pixel distance is closely related to the texture coarseness. For fine texture, the auto-correlation will drop off faster than coarse texture does as the distance increases. For regular texture, it will change in a periodic fashion. For this method to be applicable, the original image is assumed to have additive Gaussian white noise, so that the noise will not play a role in the power spectrum. This methodology is equivalent to spectral analysis, i.e., the Fourier power spectrum. In fact, they are Fourier transforms of each other. The limitations of these methods are inherent in the assumptions made about the noise. In addition, these methods of texture discrimination lack the ability to spatially localize texture elements.

Based on the research on texture pairs having identical second-order statistics, it was found that the human pre-attentive texture discrimination system cannot globally process third- and higher-order statistics [54]. Nevertheless, texture analysis methods based on Higher Order Statistics (HOS) have been proposed [55, 56]. It has been found that cumulants, which are higher order statistics, are immune to non-Gaussian or colored noises. They are, therefore, particularly powerful in analyzing texture when the power spectrum is flat or near flat. However, this technique is computationally intensive and both translationally and rotationally invariant. More importantly, the lack of localization ability for segmenting specific elements makes this approach inapplicable for segmenting structures considered in this thesis.

There has also been considerable research activity exploring image texture using spectral analysis. It is well known that the Fourier transform provides the global magnitude and phase information in the spatial frequency domain. The power spectrum can capture the image's directionality as well. Lendaris and Stanley [57] employed methods which divide the Fourier domain into independent sets of angular and radial bins as shown in Fig. 2.4.

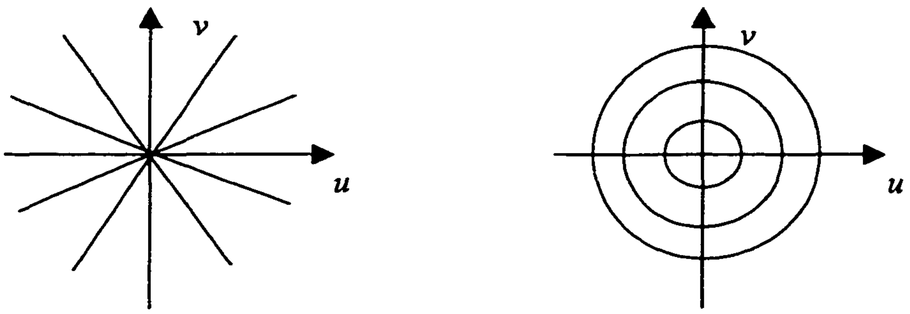

Angular Bins

Radial Bins

Fig. 2.4 The divided Fourier domain for angular and radial discrimination.

The high frequencies in the textured image will manifest themselves in the outer radial bins, while the low frequencies will stay in the inner radial bins. The angular bins provide the discrimination of the directionality. Thus, the image texture can be classified by identifying those bins where most of the signal power of the image texture is concentrated. This method is applicable for texture classification, where the texture of the whole image is under question. Fourier power spectrum generally lacks the localization properties that are needed if the texture analysis is meant to do segmentation. It is the main reason that statistical methods, which can be adapted to have local discriminating power, were traditionally considered superior to frequency domain techniques [45]. We now review algorithms that have been developed based on texture properties to solve the segmentation problem.

2.3 Segmentation of Textured Images

Generally, image segmentation is the process that subdivides an image into its constituent parts or objects. It is one of the most important elements in automatic image analysis because it is at this step that objects or other entities of interest are extracted from an image for subsequent processing. The implementation of image segmentation is the division of the image into regions, or segments, each of which is homogeneous. That is, pixels in one region are more similar to each other than pixels in other regions. This similarity can be described by various image attributes, which include gray-level, color, or texture measures. There are three principal approaches to segmentation in general: 1) region-based schemes, where adjacent regions of images are merged on one of the homogeneous property; 2) edge-based methods, where local discontinuities are detected and connected to form boundaries; and 3) clustering, where characteristic features extracted from local areas on the image and a clustering methods is used to group the feature space into clusters [58].

Algorithms for texture segmentation essentially fall into two categories: supervised and unsupervised approaches. Supervised approaches utilize *a priori* knowledge of the textures and the number of texture classes for segmentation. In the case of supervised segmentation, either the segmentation is guided by an expert knowledgeable in the classification of domain-specific texture classes, or the classes have been obtained through a training set. Unsupervised segmentation assumes no such information available whatsoever and is usually very computationally costly. Most algorithms for image segmentation are not totally unsupervised, but they may have varying degrees of supervision in terms of heuristics that are applied.

Gray-level based segmentation algorithms generally are unsupervised and depend on either the region-based (similarity) or the edge-based (discontinuity) method. The discontinuity-based approach refers to partitioning an image based on abrupt changes in gray level, and the principal areas of interest are detection of isolated points, detection of lines and edges. The similarity-based approach deals with thresholding, region growing, and region splitting and merging, with some degree of supervision.

For a textured image, the homogeneity of a particular region in the image is characterized by the texture property and there has been considerable work specifically focused on segmentation of textured images (See [59], [60] and [61] for reviews). While many of these segmentation methods are primarily based on methods which use region growing, split-and-merge, there has been a proliferation of segmentation techniques based on Bayesian classification, relaxation, clustering, and neural networks.

In the following, we will review some of the texture analysis methods suited for segmentation. One of the better statistical methods is the application of gray-level co-occurrence matrix (GLCM) [53]. Based on the success of GLCM, there have been many similar approaches proposed. Different methods strive to explore various texture primitive descriptions. Patel *et al* used a *Texture Co-occurrence Spectrum* for each texture sample by extracting information from all directions around a pixel with four 4-

tuple masks [58]. They are H(horizontal), V(vertical), DL(diagonal left), and DR(diagonal right). The pixel values under the mask are ordered and coded as a rank. Finally, the statistics of the ranks are used instead of the pixel pairs to form the texture feature. Reasonable segmentation results were reported when the method was applied to natural texture composites.

He and Wang [62] proposed another texture spectrum definition. The texture primitive is defined as texture unit, which is extracted from the 3×3 neighborhood and represents the smallest complete texture information. The eight pixels surrounding the central pixel are compared with the center in terms of gray-levels. Each of the eight pixels can be assigned the value 0, 1, or 2 as the result of the relationship of smaller than, equal, or greater than the center. The texture unit at a pixel can thus be defined as a permutation of the eight possible values of (0, 1, or 2). The statistics of the occurrence frequency of the texture units over a larger region of an image can then be derived to capture the texture information. Like all co-occurrence based texture analysis methods, there is always the difficult problem of choosing the window size of the minimum texture region.

Other efforts to classify texture included the auto-regressive moving average (ARMA) model [63], where the model parameters were estimated as the texture feature. This method exploits the linear dependence of one pixel on other pixels in its neighborhood. It was originally proposed for synthesizing texture and later extended to texture segmentation based on two-dimensional estimation. It was shown to perform well on streaky textures. Manjunath *et al* [64] used Markov random field for unsupervised texture segmentation. The estimated parameters of the assumed Gaussian Markov random field (GMRF) are used as the texture feature. Segmentation was obtained by clustering based on a normalized Euclidean distance. Then the parameters of the model estimated from the clusters were further utilized to approximate a maximum *a posteriori* estimate of the cluster labels and to minimize the misclassification error. The method is computationally expensive, and while it could model some fairly random texture patterns, the model parameters do not give immediate information about the orientation aspect of the texture pattern.

Pentland [65] proposed using the fractal dimension (*FD*) as a feature for texture segmentation, based on the finding that there exists a high correlation between fractal dimension and human estimates of roughness. The fractal dimension D of a bounded set A in $I\!R^n$ is a real number used to characterize the geometrical complexity of A. It is estimated based on the concept of self-similarity, that is: a bounded set A in Euclidean n-space is self-similar if A is the union of N_r distinct (non-overlapping) copies of itself scaled up or down by a ratio r. Then the fractal dimension D of A is given by:

$$D = \frac{\log(N_r)}{\log(1/r)} \qquad (2.3.1)$$

High fractal dimension implies a high level of roughness or coarseness of texture. Algorithms based on *FD* as an estimate of texture are generally computationally expensive or cover only a small dynamic range, and sometimes are inaccurate [66].

Moreover, different textures may have the same *FD* because of dependence not only on coarseness but on directionality as well. Thus, even though Chaudhuri and Sarkar's work [66] has obtained good results on Brodatz' texture samples, textures in general are not fractals or can only be considered so over a limited range of scales [59]. More importantly in our case, its inability to distinguish orientational information greatly reduced its usefulness to be applied in situations where the directionality of the texture is critical for characterization of image segments.

Laws [67] first proposed an operator-based feature, where four 5×5 center-weighted filter masks were convolved with the image to be segmented. From the filtered image, texture energy measures were formulated by computing variances within a 15×15 window for each pixel, and used as the texture feature. The method was claimed to generally outperform statistical methods. Unser [68] introduced a similar method and generalized these filter operators as local linear transforms. He used simpler 2×2 Hadamard masks to measure the local average and the local derivatives in horizontal, vertical and diagonal directions, and used the local statistics as the texture feature. Hsiao and Sawchuk's work [69] extended Laws' work by introducing EPNSQ (edge preserving noise smoothing quadrant) to do feature smoothing so that the boundary between texture regions is maintained.

Recently, a number of studies have focused on utilizing the joint spatial/spatial frequency (*s/sf*) approach in solving the texture representation problem. The assumption was that texture could be characterized by localized frequency contents in the spatial domain. Most of these methods were able to achieve high resolution in both the spatial and spatial-frequency domains and were consistent with the recent theories on human visual system. Among others, proposed methods include: spectrogram [70], Wigner distribution [71], Gabor filters [20, 22], Gabor wavelets [24] and general wavelet transforms [21, 23] etc. The latter approaches, which essentially utilized a localized spectral analysis, appeared particularly well suited for solving problems where local texture and orientation is of prime importance. The localization property leads to easier segmentation. In addition, multi-resolution analysis methods such as wavelet analysis provided rich choices in creating and selecting powerful texture discriminative features. The energy pattern distributed in resolution space, for example, could provide unique information, and support a representation for classifications. Therefore, we can create a feature vector consisting of a set of energy values as a discriminating signature, then use such a feature in classification and segmentation.

One of the most popular s/sf approaches was derived from using Gabor filters (Gabor wavelets are equivalent to an appropriately formulated Gabor filter set). The primary benefit of using the Gabor filters is that a wide range of pre-attentively discriminable textured regions can be distinguished by the first-order differences in the values measured by the filters [19]. This performance can be attributed to the similarity of the receptive fields of cortical neurons to the Gabor filters [72], which are related to the Gaussian filters [73]. Bovik *et al* [20] pioneered the work of applying Gabor filters to texture segmentation. They chose Gabor filters because of their useful properties of tunable orientation and radial frequency bandwidths, tunable center frequencies, and optimal resolution in both space and spatial frequency (See Chapter 3). They used a peak finding scheme applied to the global power spectrum in order to select the relevant filters. Feature selection was based on taking the maximum filter response at any position in the image. Instead of using complex-valued Gabor filters, Jain and Farrokhnia [22] used even-symmetric Gabor filters (the real part) only, and computed the local energy from the filter output as the texture feature. Filter selection is based on ranking the integrated power in the frequency bands, and taking the filter subset for which the summed power is a given fraction of the total power (95%). Starting with an initial set of 20 filters, 11 to 13 filters were required to segment simple Brodatz textures.

Methods using Gabor filters, as proposed above, all involved the proper choices of Gabor filter parameters. The bigger the filter set, the more accurate the feature. When a feature vector exceeds 20 feature elements, the computational load incurred will become rapidly unmanageable. An optimal Gabor filter design has been proposed in [74], which found one filter that was optimal in the sense of a pre-defined filter quality measure. One limitation of this approach is that this filter quality measure is derived based on the prerequisite that the textures to be segmented must be known *a priori* and is therefore a completely supervised segmentation approach. This limitation precludes the use of the method exploring unknown texture regions, as is studied in this dissertation.

Teuner *et al* [75] proposed a method for unsupervised texture segmentation using tuned and matched Gabor filters. The approach estimated the dominant spectral contrasts, which were computed from the magnitudes of the Gabor coefficients as obtained through Gabor expansion. It started from the low resolution and calculated a *spectral feature contrast matrix*, which was defined to detect those coefficients that differ significantly from the mean of all other coefficients with the same spectral indices. The *feature contrast matrix* was then computed iteratively and the maximum matrix element between levels was compared. The algorithm stopped when no larger contrast value existed in smaller elementary cells than those that have occurred at the preceding iteration step. That is, the algorithm would terminate when no novel features in smaller image regions had been identified. The center frequencies and the orientations of the tuned Gabor filters were determined by sorting the feature contrast value of the matrix of the last level, and thresholding them to pick the most salient ones. This method essentially found a ranking of Gabor filters at the highest resolution where there was meaningful contrast for texture determination. This method did not utilize the multiresolution or wavelet properties inherent in the Gabor filters at each level. Therefore, it is not clear that this expansion most efficiently utilized the texture information.

Recently, a number of algorithms based on pure discrete wavelet transform have been proposed for texture segmentation methods. One method [76] used a tree-structured wavelet transform on textured image segmentation. Firstly, the image to be segmented was decomposed with 2-D two-scale wavelet transform into four subimages as parent and children nodes in a tree. Then, energies of each decomposed image at the children node were calculated, and used as the texture feature. The decomposition continued in each subimage until the energy of this subimage was significantly smaller than others. The clustering-based segmentation started from the lowest resolution (leaves in the tree) and went from bottom-up. Other wavelet-based texture analysis methods can be found in [21, 23, 77] and [78], though all were applied to texture classifications only. Unser [79] tried wavelet frames both in texture classification and segmentation applications, and reported better performance than the standard wavelet transform feature extraction, when used in classifying 12 Brodatz textures. Most recently, M-band wavelet decomposition has been proposed in discrimination of natural textures [80]. Compared with the traditional 2-scale wavelet decomposition, it provided enhanced frequency resolution, which is more suited to natural textures.

Gabor filters are sometimes termed as *crude* wavelets, as they do not have the appealing properties like orthogonality, compact support etc., which are crucial in discrete wavelet transform implementation. Their performance, however, in multiresolution approaches to texture discrimination has been fairly good. It has been reported that the Gabor filter based texture feature performed better in image retrieval applications than other wavelet or multiresolution based approaches [24]. These other methods included: multi-resolution simultaneous auto-regressive model features, orthogonal wavelet transform features, bi-orthogonal wavelet transform features, tree-structured decomposition using orthogonal filter bank, and tree-structured decomposition using bi-orthogonal filter bank. In addition, a comparative study has been made [81] to evaluate the capabilities of different spatial/spatial-frequency methods including Gabor filters, wavelets, and wavelet packets for the purpose of both texture segmentation and classification. When Gabor filters using half-octave frequency progression were used, the performance was better than either wavelets or wavelet packets.

It is not easy to measure the performance of texture segmentation methods, considering the diversity of the texture contents. The subjects range from textured images from the classic Brodatz's texture album [82], to synthesized images, to real images such as satellite images. The majority of the texture analysis techniques, therefore, have been applied to texture images that are almost perfectly arranged to provide the most homogeneous appearance. Real world texture images are more likely to be obscured by noise, poor lighting etc. In this instance, the performance is more realistically evaluated on subjective basis. Du Buf *et al* [83] described a comparative study of texture features with particular emphasis on the applicability to unsupervised image segmentation. He focused on the performance of various texture feature extraction schemes by fixing the segmentation method to an approach based on quad-tree decomposition. The test images were bipartite and contained synthesized textures created stochastically from four groups, the Gaussian lowpass and bandpass filters, FIN (Filtered impulse noise) and Fractal. It was shown that Haralick's [53] co-occurrence matrix based feature, Unser's [68] and Laws' texture energy feature [67] performed the best. The author attributed the better performance of Laws' feature to its similarity to Gabor function. He didn't cover the Gabor-based methods directly though.

Despite the variety of methods proposed, automated segmentation of complex medical images remains at the stage of laboratory research [8]. One reason for this is the difficulty in developing simple, universally applicable methods to deal with real world problems without domain knowledge. So image segmentation is more or less a case specific approach. Brain section microscopic images fall into this category, because they are characterized by irregularly shaped nuclear groups, with constituent neurons of varied sizes and shapes, forming a unique textured pattern. Bone pictures share the same attributes where orientation of bone struts is of particular interest. In this thesis, we will develop a multi-resolution texture-based algorithm using Gabor wavelets and show that it is a potentially powerful informatics tool in analyzing and segmenting textures where orientation, shape and architecture are fundamental components.

CHAPTER 3. TEXTURE SEGMENTATION BASED ON GABOR WAVELETS

3.1 Wavelet Transform

The wavelet transform could be viewed as an extension of the Fourier transform. The Fourier models represent functions as weighted sums of sinusoids, which form an orthogonal basis for the function space [84]. The basis functions for the Fourier transform can be represented by exponential functions with imaginary arguments. By Euler's theorem, these exponential functions represent sinusoids at different frequencies. The weight associated with each function at each frequency is the Fourier coefficient. For image analysis, the Fourier transform can be extended to two dimensions, representing weighted combinations of functions at different frequencies and along different directions in the plane. Wavelet models analogously represent functions as a weighted sum of functions that are scaled and translated versions of a "mother" wavelet. In short, the wavelet transform replaces the complex exponential function with a wavelet function and scaling and translation of the mother wavelet function replaces frequency multiplication.

A representation of a function by a wavelet expansion is called the forward procedure. Wavelet reconstruction involves putting the wavelet pieces back together to retrieve the original function, and is called the inverse wavelet transform. Wavelet theory consists of the study of these pieces (wavelets), their properties and interrelationships, and how to put them back together. The primary and most advantageous application areas of wavelet theory are those that generate or process wideband signals, which simultaneously have both short-term characteristics and trends with relatively long-term characteristics. In addition, the duration of the interesting portion of the wideband signal is not known *a priori.*

The class of functions that the wavelet transform in two dimensions represents is similar to the function class represented by the Fourier transform. That is, the member functions should be square integrable on the real plane [2]. The definition of a wavelet can then be given as follows [85]:

Definition:

If $g(x)$ is a real-valued function whose Fourier spectrum, $G(\omega)$, satisfies the admissibility criterion:

$$C_g = \int_{-\infty}^{\infty} \frac{|G(\omega)|^2}{|\omega|} d\omega < \infty \qquad (3.1.1)$$

then $g(x)$ is called a basic wavelet.

Because there is an ω in the denominator, it is necessary that the basic wavelet have no DC component and be oscillatory. In addition, to keep the integral bounded as $\omega \to \infty$, the Fourier transform of the wavelet must go to zero. That means the basic wavelet must decay toward zero to make $G(\infty) = 0$. These requirements extend to two dimensions.

The 1-D continuous wavelet transform of a function, *f*, with respect to a given admissible mother wavelet, *g*, is defined as:

$$W_g f(a,b) = |a|^{-\frac{1}{2}} \int f(x) g^*\left(\frac{x-b}{a}\right) dx \qquad (3.1.2)$$

Where superscript "*" denotes complex conjugate and the $|a|^{-1/2}$ term is for normalization that keeps the energy of the scaled mother wavelet equal to the energy of the original mother wavelet.

The wavelet transform defined above is an analysis filter. It breaks a signal down into component pieces so that these pieces are examined or operated on instead of the original function. That is because in most cases significant insights can be obtained through analyzing the pieces rather than the original function. The inverse wavelet transform or reconstruction filter is a synthesis filter, which puts the original signal back together. As a special case when $g(x) = e^{jx}$, $a = 1/\omega$, and $b = 0$, the wavelet transform becomes Fourier transform.

The choice of a specific mother wavelet has been an important topic of wavelet theory [86, 87]. The important properties of a wavelet under consideration include:

1) Whether or not there exists discrete decomposition using FWT: Fast Wavelet Transform;
2) Whether or not it is an orthogonal base, which determines if a non-redundant perfect reconstruction is possible;
3) Whether or not there exists an explicit expression for the wavelet function, etc. [88].

In practice, choosing a wavelet is highly dependent on the application field. Image compression and texture analysis would require different wavelet to be used. For example, in image compression applications, it is necessary to have a nice reconstruction property requiring non-redundancy. However, for texture analysis applications, it might be preferable to have redundant information for easier discrimination. The 2-D Gabor wavelet has been suggested as an important basis for studying texture and has been utilized in many applications [19, 20, 22, 24, 75]. In this thesis, we develop its texture-discriminating features and apply it to cellular structure and orienting architectures.

The Gabor function was originally proposed by the Hungarian-born physicist Dennis Gabor in time-frequency analysis [89], where the transmission and compression of sound waves were studied. This study was a fundamental "inquiry into the essence of the "information" conveyed by channels of communication, and the application of the result of this inquiry to the practical problem of optimum utilization of frequency bands." The major finding was that with the use of Gaussian windowing functions to represent time functions in the frequency domain, resulted in obtaining the lower bound in the uncertainty relationship between frequency and time. This windowing function became known as the Gabor function. The 2-D Gabor function $f(x,y)$, is a two-dimensional Gaussian function which is multiplied by a complex exponential function [90]. Gabor wavelets have the important property that the spatial and spatial-frequency resolutions are simultaneously optimized so that they give a joint optimal base. That is, the uncertainty parameter for localization in both the space and spatial-frequency domains is the smallest [90]. This is easily seen by using the *Heisenberg Uncertainty Principle* which gives a firm lower limit on the resolution as [89]:

$$\Delta_x \Delta_u \geq \frac{1}{4\pi} \tag{3.1.3}$$

where Δ_x and Δ_u are the effective durations in the spatial and spatial frequency domains. They are defined respectively as:

$$\Delta_x = \sqrt{\frac{\int_{-\infty}^{\infty}\int_{-\infty}^{\infty}(x-x_0)^2 \,|f(x,y)|^2\, dxdy}{\int_{-\infty}^{\infty}\int_{-\infty}^{\infty}|f(x,y)|^2 dxdy}} \tag{3.1.4}$$

and

$$\Delta_u = \sqrt{\frac{\int_{-\infty}^{\infty}\int_{-\infty}^{\infty}(u-u_0)^2 \,|F(u,v)|^2\, dudv}{\int_{-\infty}^{\infty}\int_{-\infty}^{\infty}|F(u,v)|^2 dudv}} \tag{3.1.5}$$

where x_0 and u_0 are the mean values of the respective variables. Similar uncertainty equations can be obtained for relations between Δ_y and Δ_v as :

$$\Delta_y \Delta_v \geq \frac{1}{4\pi} \tag{3.1.6}$$

Thus, the lower limit for any two-dimensional filter with joint resolution is constrained by the uncertainty:

$$\Delta_x \Delta_u \Delta_y \Delta_v \geq \frac{1}{16\pi^2} \tag{3.1.7}$$

If *f(x,y)* is the Gabor function, then the lower limit given by *Heisenberg*'s principle is achieved. This resolution property is particularly important in texture segmentation because the texture segmentation requires simultaneous measurements in both the spatial and spatial-frequency domains. Filters with smaller bandwidth in the spatial-frequency domain are capable of making finer distinctions among different possible textures. On the other hand, accurate localization of texture boundaries requires filters that are localized in the spatial domain. It is interesting that psychophysical research has shown that the 2-D Gabor function (Gaussian windowed sinusoidal plane wave) coincides with the receptive field profiles of simple cells in the visual cortex of some mammals [72]. In addition, the Gabor function has distinct orientation properties [20]. It is these properties that make the two-dimensional Gabor function an appropriate candidate wavelet for the analysis and segmentation of a wide range of stained tissue from brain and bone. In this research, we develop the Gabor wavelet texture segmentation scheme based on a Gabor filtering method suggested by Jain and Farrokhnia [22]. Its limitation in this particular application will be discussed, and the necessary improvement will be developed.

3.1.1 Gabor Wavelet Transform

A general bandpass filter in one dimension can be expressed in the frequency domain as the transfer function:

$$H(f) = G(f) * [\delta(f - f_0) + \delta(f + f_0)] \tag{3.1.8}$$

where f_0 is the center frequency of the passed band and * is the convolution operator. In the ideal case, $G(f)$ should be a rectangular pulse [91]. A more realistic implementation would be a nonnegative unimodal function such as a Gaussian. The transfer function, $G(f)$ is then given by:

$$G(f) = e^{-\frac{f^2}{2\alpha^2}} \tag{3.1.9}$$

The filter's impulse response in the time domain takes the form as:

$$h(t) = 2g(t)\cos(2\pi f_0 t) = \frac{2}{\sqrt{2\pi}\sigma} e^{-\frac{t^2}{2\sigma^2}} \cos(2\pi f_0 t) \tag{3.1.10}$$

where $\sigma = 1/(2\pi\alpha)$. This impulse response, which is comprised of a cosine function modulated by a Gaussian, is exactly the even-symmetric version of a one-dimensional Gabor filter. This example shows that filters based on Gabor functions are essentially bandpass filters. This idea can be extended to two dimensions where the complex 2-D Gabor filter has the impulse response given by:

$$h(x,y)=\frac{1}{2\pi\sigma_x\sigma_y}\exp\{-\frac{1}{2}[\frac{x^2}{\sigma_x^2}+\frac{y^2}{\sigma_y^2}]\}\cdot[\cos(2\pi u_0 x)+j\sin(2\pi u_0 x)]. \quad (3.1.11)$$

with the Fourier transform $H(u, v)$ as:

$$H(u,v)=\exp\left\{-\frac{1}{2}\left[\frac{(u-u_0)^2}{\sigma_u^2}+\frac{v^2}{\sigma_v^2}\right]\right\} \quad (3.1.12)$$

where $\sigma_u=1/2\pi\sigma_x$, $\sigma_v=1/2\pi\sigma_y$.

The impulse response of this filter is a complex function of the spatial coordinates. If σ_x and σ_y are different, its amplitude decay depends on directions. Both the real and complex responses oscillate along the x axis. Although the complex-valued Gabor filter is mathematically convenient, it has found no biological justification. To obtain a physically meaningful function, one generally works with the real part or the summation of the function in Eq. (3.1.11) with the complex conjugate function. The choice of using a real-valued, even-symmetric Gabor filter instead was justified in [92]. The limitation of a real-valued Gabor filter is that it will not distinguish texture patterns that are the same but with a 180° phase flip.

The impulse response of an even-symmetric Gabor filter (mother wavelet) is given by:

$$h(x,y)=\frac{1}{2\pi\sigma_x\sigma_y}\exp\{-\frac{1}{2}[\frac{x^2}{\sigma_x^2}+\frac{y^2}{\sigma_y^2}]\}\cos(2\pi u_0 x) \qquad (3.1.13)$$

where u_0 is the frequency of a sinusoidal plane wave along the x-axis, and σ_x and σ_y are the space constants of the Gaussian envelope along the x and y axes, respectively. The spatial frequency, u_0, takes on dyadic values, which are multiples of 2 of some primary value. Both σ_x and σ_y take on values related to the center radial frequency u_0. Filters with arbitrary orientations (θ) can be obtained via a rigid rotation of the x-y coordinate system by ($-\theta$):

$$\begin{aligned} x^{\cdot} &= x\cos\theta - y\sin\theta \\ y^{\cdot} &= x\sin\theta + y\cos\theta \end{aligned} \qquad (3.1.14)$$

In this fashion, a set of Gabor wavelets or filters can be generated which cover the two-dimensional image plane. The Fourier transform representation of each Gabor filter can be given by:

$$H(u,v)=\exp\left\{-\frac{1}{2}\left[\frac{(u-u_0)^2}{\sigma_u^2}+\frac{v^2}{\sigma_v^2}\right]\right\}+\exp\left\{-\frac{1}{2}\left[\frac{(u+u_0)^2}{\sigma_u^2}+\frac{v^2}{\sigma_v^2}\right]\right\} (3.1.15)$$

where

$$\sigma_u = \frac{1}{2\pi\sigma_x} \qquad \sigma_v = \frac{1}{2\pi\sigma_y} \tag{3.1.16}$$

Fig. 3.1 shows both $h(x, y)$ and $H(u, v)$ in a 2-D plot.

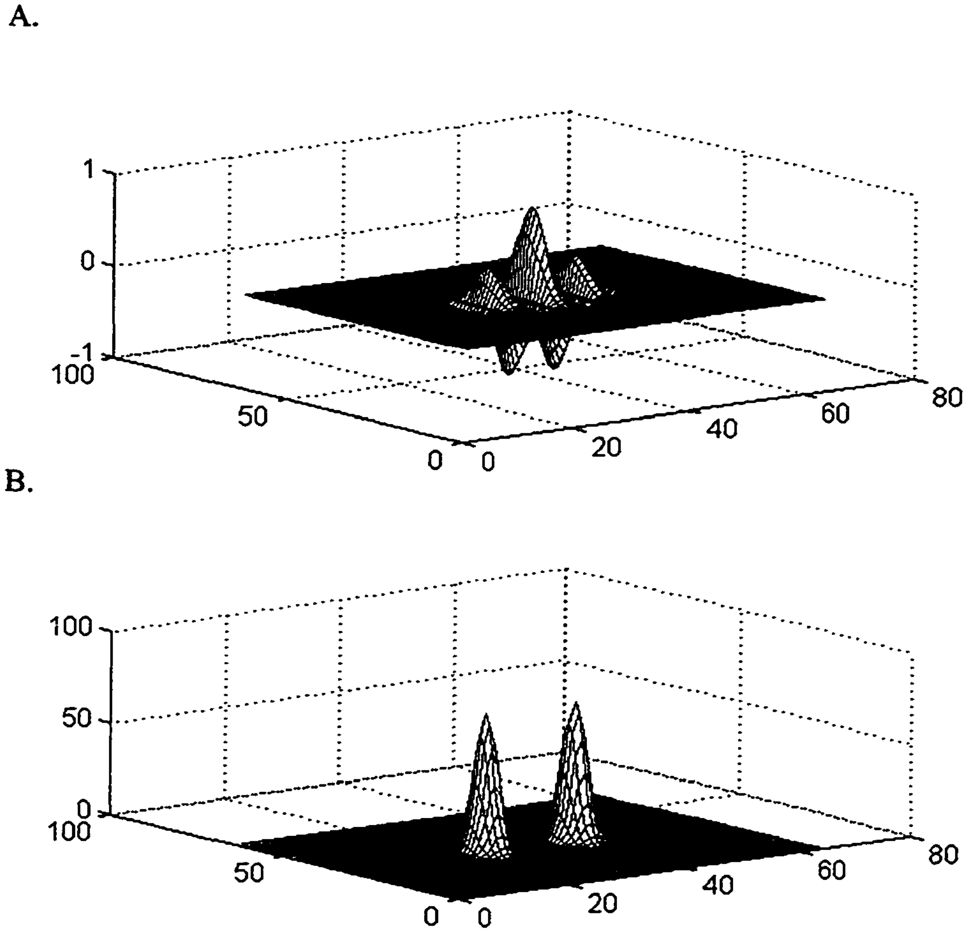

Fig. 3.1 Illustration of a Gabor filter. (A) The impulse response of an even-symmetric Gabor filter with orientation at zero degree and spatial frequency at 8 *cycles/64 pixels*. The Gaussian envelope has the parameters as σ_x=6 and σ_y=4. (B) The correspondent Fourier transform of (A).

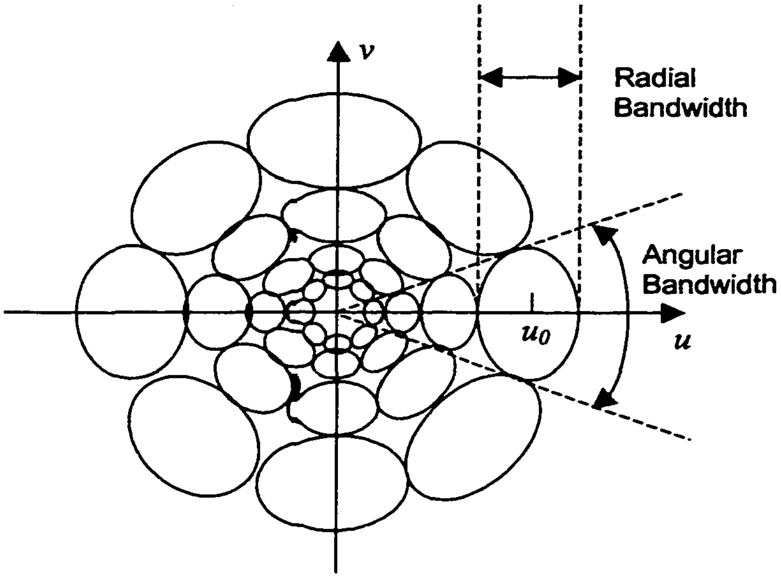

Fig. 3.2 The Gabor filter set with half-peak support in the frequency domain. For each spatial frequency band, there are four orientations. Only 4×4=16 filters are shown.

The design of Gabor filter entails determining the filter parameter, σ_u and σ_v. This is equivalent to specifying the radial and angular bandwidth supports for both the spatial frequency and the orientation of each filter. Once σ_u and σ_v are determined, σ_x and σ_y can be derived accordingly, using Eq. (3.1.16). Fig. 3.2 shows the filter set in the Fourier domain, with the contours indicating the half-peak magnitude of the filter responses.

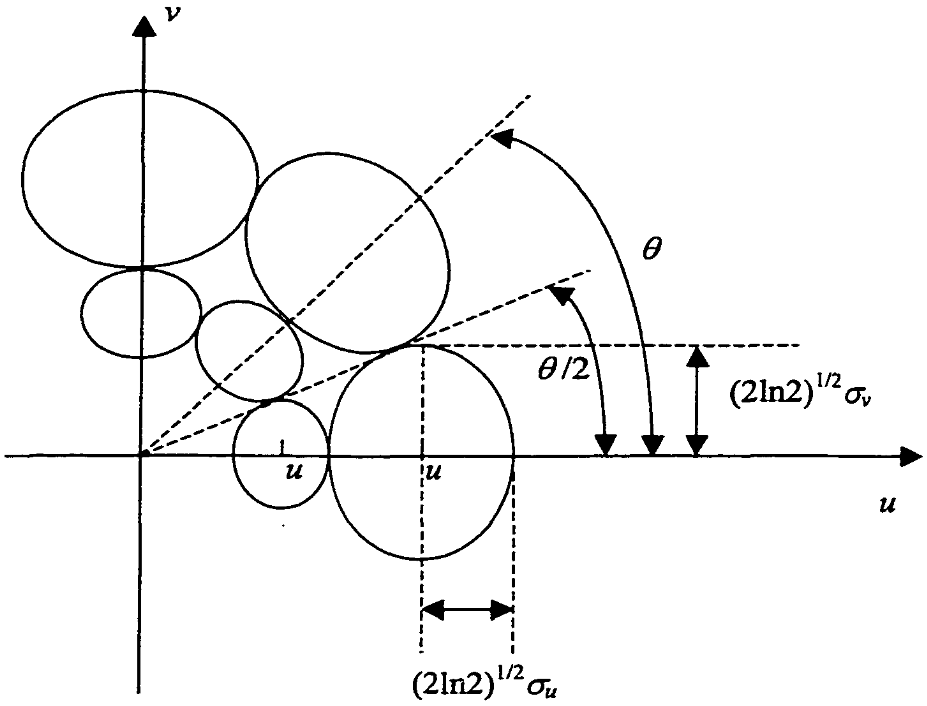

Fig. 3.3 A diagram illustrating the determination of σ_u and σ_v. Given the center frequency u_0, rate of frequency progression and the orientation resolution θ, σ_u and σ_v are determined by making the half-peak contours of filter sets tangent to each other, and deriving the lengths of the constrained semimajor and semiminor axes of the ellipse-shaped filter support.

Gabor filters are not compactly supported because the Gaussian function extends to infinity. Therefore, it is common to design the filter set so that the half-peak magnitude support of the filter responses in the frequency spectrum touch each other as shown in Fig. 3.2. This constraint on the support insures that the resulting bandwidth support will have small overlap and cover the whole spectrum almost uniformly. Although various approximations have been given to characterize the σ_u and σ_v of these filters [22, 90], we derive an accurate formula for both σ_u and σ_v based on geometric arguments, which are shown below and illustrated in Fig. 3.3:

For any Gaussian distribution $g(t) = Ae^{-\frac{t^2}{2\sigma^2}}$, the half-peak magnitude offset can be calculated as:

$$t_{half-peak} = \sqrt{2\ln 2}\sigma \tag{3.1.17}$$

We will denote the frequency progression rate as

$$\frac{u_0}{u_1} = 2^r \tag{3.1.18}$$

where r is in octaves.

Combining equations (3.1.17) with (3.1.18) gives

$$\frac{u_0 + \sqrt{2\ln 2}\sigma_u}{u_0 - \sqrt{2\ln 2}\sigma_u} = 2^r \tag{3.1.19}$$

which can then be solved for σ_u as follows:

$$\sigma_u = \frac{(2^r - 1)u_0}{(2^r + 1)\sqrt{2\ln 2}}. \tag{3.1.20}$$

If we denote the orientation resolution as θ, then, as shown in Fig. 3.3, the line defined by

$$v = \tan(\frac{\theta}{2})u \tag{3.1.21}$$

should be tangent to the contours of both the filter at *0°* and the filter at *θ*. The contour of the *0°* filter can be defined as:

$$\frac{(u - u_0)^2}{a^2} + \frac{v^2}{b^2} = 1 \tag{3.1.22}$$

where

$$a = \sqrt{2\ln 2}\sigma_u \tag{3.1.23}$$

and

$$b = \sqrt{2\ln 2}\sigma_v \tag{3.1.24}$$

Replacing the variable v in the equation for the ellipse (3.1.22) with the equation for a straight line (3.1.21), we obtain a quadratic equation:

$$\left[b^2 + a^2 \tan^2(\frac{\theta}{2})\right]u^2 - 2u_0 b^2 u + (u_0^2 - a^2)b^2 = 0 \qquad (3.1.25)$$

The tangent condition of (3.1.21) and (3.1.22) impose a uniqueness constraint on u that demands that the discriminant of the quadratic be equal to zero. This implies:

$$(-2u_0 b^2)^2 = 4\left[b^2 + a^2 \tan^2(\frac{\theta}{2})\right]\cdot\left[(u_0^2 - a^2)b^2\right] \qquad (3.1.26)$$

Solving Eq. (3.1.26) for b, we obtain:

$$b^2 = (u_0^2 - a^2)\tan^2(\frac{\theta}{2}) \qquad (3.1.27)$$

Using Eqs. (3.1.23) and (3.1.24) for a and b, we obtain:

$$\sigma_v = \tan(\frac{\theta}{2})\sqrt{\frac{u_0^2}{2\ln 2} - \sigma_u^2} \qquad (3.1.28)$$

Finally, σ_x and σ_y can be determined from Eq. (3.1.16) as:

$$\begin{aligned}\sigma_x &= \frac{1}{2\pi\sigma_u}\\ \sigma_y &= \frac{1}{2\pi\sigma_v}\end{aligned} \qquad (3.1.29)$$

These results compare favorably with those given by others [22] in that they improve for finer angular bandwidths.

It should be noted that r is given in octaves. If we choose full-octave frequency progression, the r will be 1. If we choose half-octave frequency progression, the r will be ½ instead. The angular resolution, θ, depends on the total number of orientations desired. In our research r is set at 1 and θ is chosen to be $\pi/4$ (45°).

3.2 Multi-Resolution Texture Feature Selection

Choosing the best representative feature that describes the texture property is perhaps the most important issue. Insight regarding this issue has come from analogy with the type of texture processing done by the human visual system [52, 54]. Psychophysical experiments support the hypothesis that the analysis of a stimulus by the visual system involves a set of quasi-independent mechanisms, called channels, which could be conveniently modeled as filters [93]. Each channel responds to gray-level changes over regions of different size or at different orientations. The Gabor filtering scheme is very similar to that mechanism. Gray levels in each filtered image can be interpreted as representing the limited spectral information arising from small areas in the original image [22]. In other words, the Gabor filter set output carries the information needed to represent channels. Each filter is spatial-frequency and orientation selective, so the convolution of this band-pass filter and the input image captures the texture information of specific frequencies and orientation with spatially localized information retained. The different frequencies are conceptually related to the resolution representing an image. Low frequency components represent the coarse resolution, while higher frequency components represent the finer resolution. The Gabor filter set consists of multiple frequency components and is therefore naturally an implementation of multi-resolution analysis.

3.2.1 Filter Selection

In section (3.1), we derived the method of choosing the Gaussian parameters of the Gabor function. They are all based on the value of the center frequency, u_0. The choice of u_0*'s* should be made so that the frequency bands associated with them best represent the actual frequency contents of a particular texture. Therefore, they should be image-content dependent. A number of previous works have used various methods for determining u_0*'s* with varied complexities and success [53]. We will develop a simple and heuristic scheme which can be described as follows:

First, we need to determine what should be the maximum value of the center frequency u_0, which is denoted as u_{0max} Let N_w denotes the image width in pixels. The highest possible spatial frequency is then $N_w/2$ ($cycles/N_w$), and the lowest spatial frequency is 0 representing the DC component. Since a Gabor filter covers a span of frequencies centered at u_0, choosing the u_{0max} as the highest frequency possible, $N_w/2$, will waste half of the bandwidth. Choosing the u_{0max}, so that $u_{0max} + \Delta u$ is less than the highest frequency possible, will ensure better coverage in the high frequency band. Using the half-peak span of the Gaussian given by Eq. (3.1.17), we choose Δu as:

$$\Delta u = \sqrt{2\ln 2}\sigma_u \tag{3.2.1}$$

and let (u_{0max} + Δu) be the highest possible frequency, i.e.:

$$u_{0\max} + \Delta u = \frac{N_w}{2}(cycles / N_w) = \frac{1}{2}(cycles / pixel) \tag{3.2.2}$$

Since σ_u can be obtained by solving Eq (3.1.19), with r chosen as 1, we have:

$$\sigma_u = \frac{u_{0\max}}{3\sqrt{2\ln 2}} \tag{3.2.3}$$

Combining Eqs (3.2.1), (3.2.2), and (3.2.3), and solving for u_{0max}, we obtain:

$$u_{0\max} = \frac{3N_w}{8}(cycles / N_w) \tag{3.2.4}$$

Choosing u_{0max} as the candidate for the highest center frequency will allow good coverage of the high frequency content of the image signal. The successive lower frequency bands are determined by setting them one octave apart. Therefore, the sequence of center frequencies u_0's, from highest to lowest frequency, assuming N_w is the power of 2, can be given as:

$$\frac{3N_w}{8}, \frac{3N_w}{16}, \cdots, \frac{3}{1}, \frac{3}{2} (\text{cycles} / N_w) \qquad (3.2.5)$$

There are, thus, $\log_2(N_w/2)$ candidate frequency bands that can be utilized in covering the whole bandwidth. In reality, however, the low radial frequencies are not useful in texture analysis because they capture spatial variations that span the whole image instead of capturing local textural variations. Practically only a few higher frequency bands are important. The question is how to select them in an effective way for good results. Because conditions for optimality, which could be applied to general images, are not well defined, we derived a heuristic approach for choosing them.

In our implementation, we chose 3~4 levels of adjacent frequency bands, in decreasing order $u_{01} > u_{02} > u_{03} > u_{04}$. The choice of the u_{01} (the highest frequency bands to be used) was based on analysis of the global Fourier power spectrum. The Fourier spectrum was represented in polar form and the averaged power spectrum profile, as a function of $\sqrt{u^2 + v^2}$, is determined. For highly regular textures, especially simulated textures, the Fourier profile shows sharp transitions. The u_{01} could then be chosen at the point where the Fourier spectrum slope starts to increase when going from high to low frequencies and where the frequency band centered at u_{01} covers a significant part of the spectral power. For natural and irregular textured images that we encountered in analyzing anatomical substrates, the profile of the Fourier power spectrum had a smooth transition from low magnitude in high frequency bands to high magnitude in low frequency bands. We found choosing the u_{0l} as one octave down from the u_{0max} as defined by Eq. (3.2.4) gives the better result. A further elaboration and examples of the methodology for choosing the bands is given in Section (5.1.3).

Another degree of freedom in filter selection, though not as critical, is the choice of the number of orientations, θ. In this study, we used four orientations (0°, 45°, 90°, and 135°). Finer quantization of orientation might improve the texture directionality discrimination but generally will be less computationally efficient. Although a multi-resolution approach was implemented so that a greater number of orientations can be computationally feasible, for general texture discrimination, our results indicated that the effects of applying more than four orientations are not sufficiently justified, as shown in Section (5.1.4).

3.2.2 Features Using Texture Energy

While the Gabor wavelet outputs give the breakdown in local orientation and spatial frequency, the individual values of the output vary dramatically. Consequently, the Gabor filtered outputs do not provide coherent data set needed for texture features for robust local segmentation. One way to improve texture feature extraction is to process the Gabor filtered output through a transformation, which can improve the cohesiveness of the filter outputs. An appropriate function to accomplish this is a hyperbolic tangent function, which is given by:

$$y = \psi(x) = \tanh(\alpha x) = \frac{e^{2\alpha x} - 1}{e^{2\alpha x} + 1} \qquad (3.2.6)$$

where α is a constant. This bounded nonlinear function transforms the sinusoidal modulations in the filtered images to approximately square modulations, as demonstrated in Fig. 3.4. It has the property to maintain the input value x when x is small, but will saturate the output to 1 when x increases greatly. The value of α, determines the slope of $tanh(\alpha x)$ when it passes the origin, and the rate it saturates the output. The larger the value of α, the faster the saturation. This kind of nonlinearity has been utilized in neural net implementation and relaxation methodologies [71, 94], and has been applied in texture segmentation to help create more robust feature values [22]. It is also applicable to our work, particularly in the case when the given image has a high contrast and produces a wide range response from the Gabor filters. In our study, the typical output of Gabor filters is in the range around (-10, 10), therefore, we determine α empirically to be in the range of 0.1~0.4. A value of 0.1 shows relatively small amount of saturation, while a value of 0.4 has a strong saturation effect.

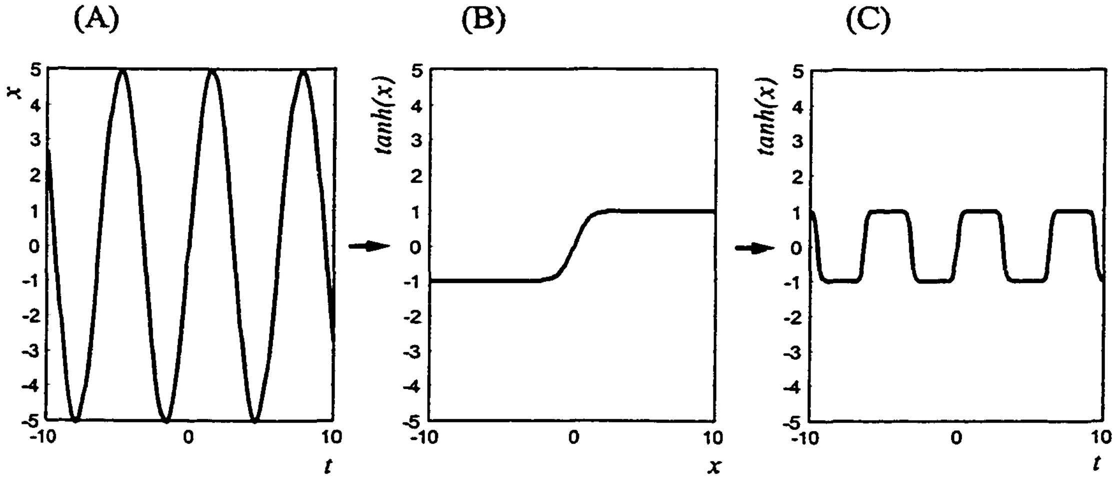

Fig. 3.4 The effects of *tanh*(*x*). (A): original *x*=*sin*(*t*) wave, (B): profile of *tanh*(*x*), (C): output of (A) transformed by (B), *tanh*[*sin*(*t*)].

As described above, the Gabor filter set is composed of filters with center frequencies, u_{0m} and orientations θ_n, where m ranges over the sequence of filter center frequencies (1~M) and n ranges over the number of orientations (1~N). Thus, there are $M \times N$ features in total. At each coordinate (x, y), the Gabor coefficients (filter output) can be given by $g_{mn}(x, y)$, where (m, n) represents one particular frequency and orientation combination. The nonlinear transformation transforms this image as $\psi[g_{mn}(x, y)]$. Features at each pixel (x, y) can then be defined in terms of $\psi[g_{mn}(x, y)]$ by computing a measure of "texture energy," the absolute value $|\psi[g_{mn}(x, y)]|$ [22, 67].

Feature smoothing is usually a necessity for robust segmentation. Jain and Farrokhinia [22] suggested that a Gaussian averaging of a region surrounding (x, y) would be a better descriptor of the texture energy for feature definition and we have implemented this window function. Thus, the texture features utilized in this thesis are given as follows:

$$e_{mn}(x, y) = \frac{1}{W^2} \sum_{(x_1, y_1) \in W_{xy}} G(x, y, \sigma_x, \sigma_y) |\psi[g_{mn}(x_1, y_1)]| \qquad (3.2.7)$$

where W_{xy} is an $W \times W$ window centered at the pixels with coordinates (x, y) and $G(x, y, \sigma_x, \sigma_y)$ is a Gaussian window centered at (x, y) with standard deviations σ_x and σ_y. Therefore, if we choose M total frequency bands and N total orientations, the $M \times N$ features associated with each pixel will be as follows.

$$[\, e_{11}\ e_{12}\ \dots\ e_{1N},\quad e_{21}\ e_{22}\ \dots\ e_{2N},\ \dots\dots,\ e_{M1}\ e_{M2}\ \dots\ e_{MN}\,] \qquad (3.2.8)$$

3.2.3 Features Exploring Cell Distribution Patterns

While these texture features were utilized in performing the first level of segmentation where nuclear structures in neuro-anatomical slides were found, we were also interested in determining whether each segment would have additional texture variation. The most important criteria for discriminating different nucleus structures include (Dr. Jean Buettner, Personal communication):

1) The density of the cell spacing, which is dependent on whether cells are closely arranged or sparsely populated.
2) The regularity of the cell spacing, which is dependent on whether cells distribution is isotropic or has a directional bias.
3) The size and the shape of the cells. Some cells may take round, or oval shapes, while others may be polygonal.
4) The location of cells. Even for the same cell patterns, when they are distributed in different locations, they could be considered as different structures.

While the last property is trivially represented in the wavelet feature vector because the wavelet filter is intrinsically local, the first three properties should also be represented in the Gabor-based texture feature. For example, the density of the cell spacing could be reflected by the overall magnitude of the texture energy of all frequency and directional components. The regularity should be represented by large components in some particular directions. A more randomly distributed cell pattern is likely to have similar energies along all orientations. Compared with smaller cells, bigger cells with larger spacing could be considered as a blow-up of smaller cells with smaller spacing, which will be reflected by the matching texture feature with a resolution shift. Because the Gabor texture energy features are inherently multi-resolutional, the pattern change in resolution can be easily represented.

To characterize some of the cellular properties, we derived an additional set of features based on the original texture energy features given in Eq. (3.2.8). These feature were utilized for the second level segmentation where sub-regions within a nucleus will be segmented. For a given frequency band m, the average energy among all orientations (μ_m) and its standard deviation (σ_m) were computed as follows:

$$\mu_m = \frac{\sum_{n=1}^{N} e_{mn}}{N} \tag{3.2.9}$$

and

$$\sigma_m = \sqrt{\frac{\sum_{n=1}^{N} (e_{mn} - \mu_m)^2}{N}} \tag{3.2.10}$$

Thus, for a total of M frequency bands, 2×M features were utilized to implement the second level segmentation. The arrangement of the feature vector associated with each pixel will be as follows.

$$[\, \mu_1 \;\; \sigma_1 \;\; \mu_2 \;\; \sigma_2 \;\; \dots \;\; \mu_M \;\; \sigma_M \,] \tag{3.2.11}$$

3.3 Segmentation Based on Partitional Clustering

A schematic of the texture segmentation algorithm is shown in Fig. 3.5. The original image is first preprocessed to identify pixels belonging to non-textured regions, which are essentially regions containing uniform gray levels. This is accomplished by examining the variance over a moving window and labeling the center pixel as belonging to uniform gray level regions if the variance is below a threshold. Another process collects large regions of connected pixels that are non-textured and discards smaller ones. The purpose of these steps is to locate those pixels along the border between the texture and non-textured regions, so that a heuristically based texture-energy adjustment method could then be implemented at a later stage to offset the false high texture energy along the border (the detail will be explained in section 4.3). Following this preprocessing, the aforementioned frequency and orientation tuned Gabor filters are convoluted with the original image, producing a series of output images. The output images are then processed by the nonlinear square modulator (Eq. 3.2.6) to cut off excessive filter output values. This is followed by an absolute value filter, which determines the pixel-level texture energy features. The texture energy features along the borders of adjacent textured and non-textured regions are then adjusted using information that has been determined in the preprocessing stage. Finally, Gaussian-smoothing generates the local texture energy features, $e_{mn}(x, y)$, for the image. These texture energy features are augmented with additional features, that include the multiresolutional Gaussian averaged value of the original image and the (x, y) pixels coordinates, which are normalized to have the same standard deviation as the energy features. This augmented feature vector is used as the basis for segmenting the image by a data clustering algorithm. A probabilistic relaxation algorithm has been implemented, which improves upon the segmentation, resulting in greater coherence of common textures.

It should be noted that the spatial-frequency filtering transforms the texture segmentation problem into a decision problem in the feature space. That is, corresponding to each pixel there is a feature vector in which the feature components representing the channels of the human perception of textures. Based on these feature vectors, the segmentation can be implemented as a *K*-mean partitional clustering procedure [95]. The flowchart for the *K*-mean clustering is shown in Fig. 3.6. The number of distinct textures, *K*, is heuristically chosen based on the expected classes into which the image will be segmented, which in turn depends on the image content. The initial *K* cluster centers have been chosen randomly. For each pattern associated with a pixel, we have computed its Euclidean distance to each cluster center, and labeled it as the same cluster with the shortest distance. After each pixel is labeled, we re-compute the cluster centers using their mean feature values. The iteration continues until the update of the cluster seeds reaches the minimum. This is characterized by comparing the averaged distances of correspondent cluster seeds between iterations. When the difference is smaller than 5%, the iteration stops. One of the examples is illustrated in Fig. 3.7, where after around 10 iterations, the difference stabilizes close to a minimal value. The final cluster centers can be viewed as the characteristic feature for the textured region it represents. Each pixel can then be classified based on the cluster to which it belongs. For an $n \times n$ sized image, with d features characterizing each pixel, the *K*-mean clustering algorithm would require $n \times n$ comparisons of d-dimensional vectors for each cluster center. To reduce the computational requirements, we have allowed the ability to down-sample the image by a number dependent on the size of the image and the number of channels. Empirically, we have found that down sampling of 10% reduced the time of the algorithm by an order of magnitude without significantly impacting the accuracy. Once the clustering based on the reduced data set is finished, final clustering is done by assigning each pixel in the original image to the nearest cluster center.

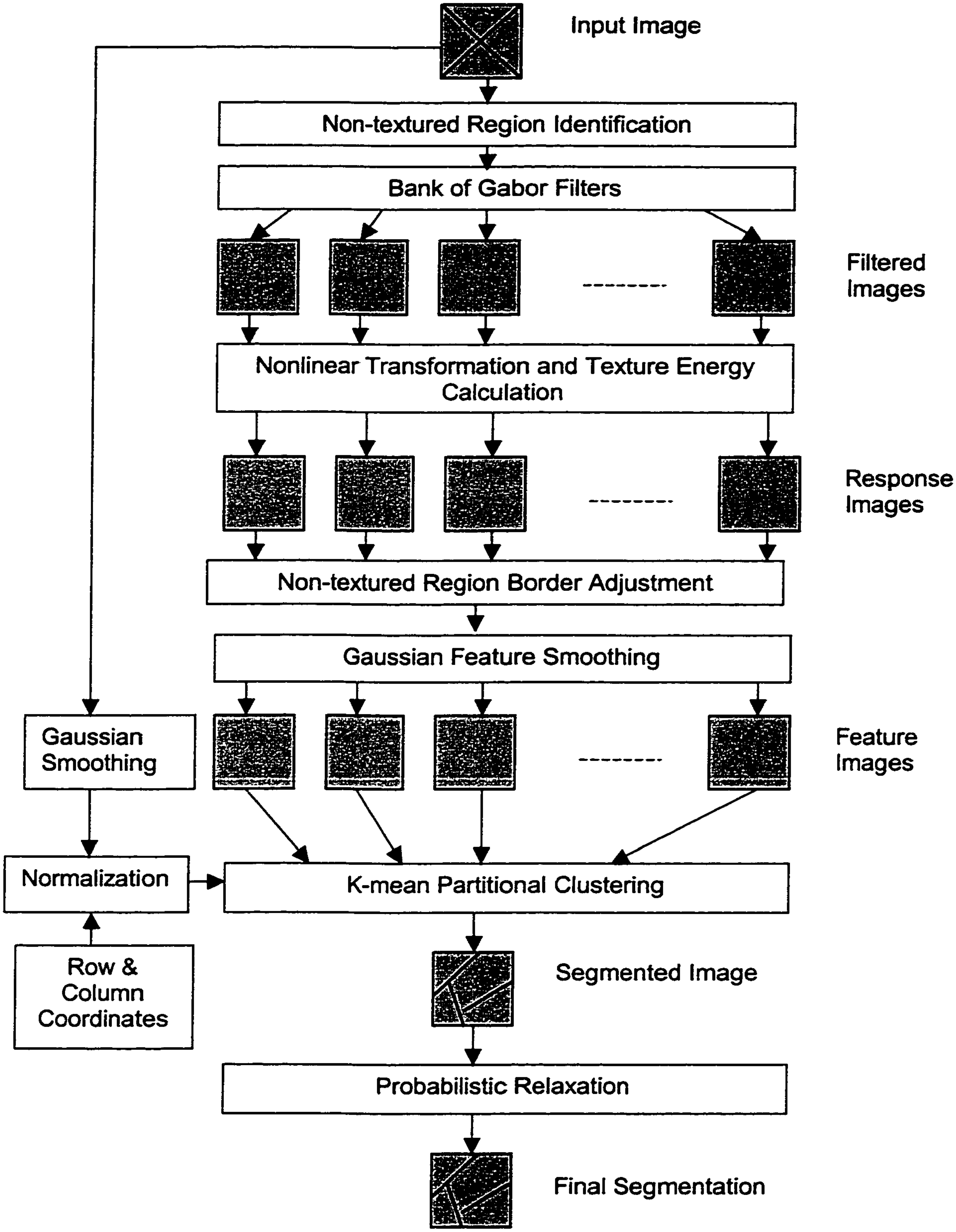

Fig. 3.5 An overview of the texture segmentation algorithm

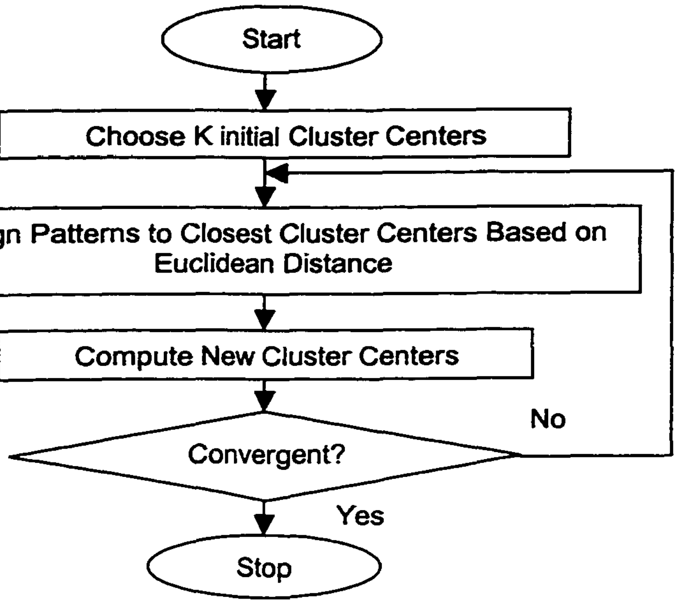

Fig. 3.6 Flowchart of the *K*-mean data clustering algorithm

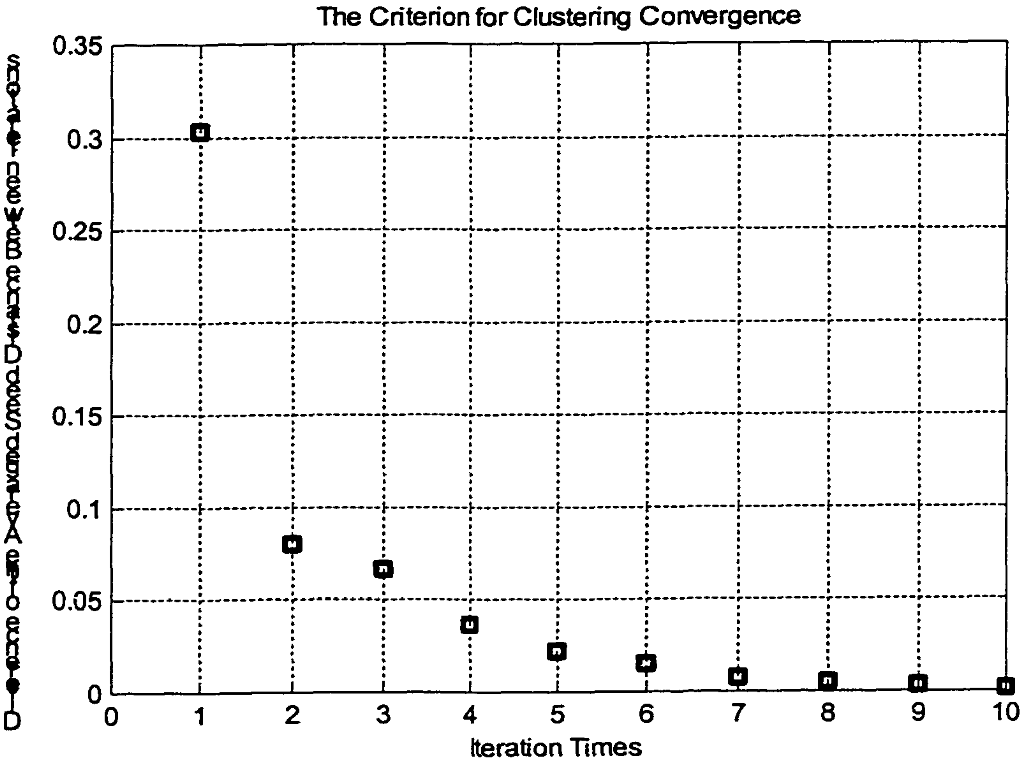

Fig. 3.7 The criterion for clustering convergence. Clustering stops when the difference of the averaged distance of cluster seeds between iterations reaches minimum (Difference between iterations < 5%)

CHAPTER 4. IMPLEMENTATION ISSUES AND PERFORMANCE ENHANCEMENT

4.1 Introduction

The implementation was initially developed under MathWorks Matlab environment. As the program grew in complexity, speed became a problem, because of the interpretive execution in the MATLAB environment. The implementation was later re-coded in C++ under the Microsoft Visual C++ Version 6.0 development environment. The program runs under Windows 9x/NT/2000 operating systems. It can be launched either as a full application with the graphical user interface, or simply as a command with a command line option for the need of batch processing. Three sets of images have been applied to the algorithm. They are, 1) simulated texture patterns, 2) real images of *Nissl* stained sections showing abducens nucleus which were provided by Dr. Buettner, and 3) real images of brainstem sections containing the abducens and vestibular nuclei, which were scanned in our own laboratory. The scanning was accomplished using a Nikon Eclipse E400 microscope with a Dage-MTI, Inc.'s NC-81LX 2000 lines video camera mounted on the top. The video signal from the camera was fed into a Matrox Meteor-II frame grabber board installed in a PCI slot inside the PC. The frame grabber can be coded to capture still images from the NTSC video signal generated by the camera at the resolution of 640×480, and save grayscale images in Windows BMP format. The video signal has also been passed to a high resolution (2000 lines) MTI HR-2000 monitor for more convenient visualization. The microscope and the camera are shown in Fig. 4.1

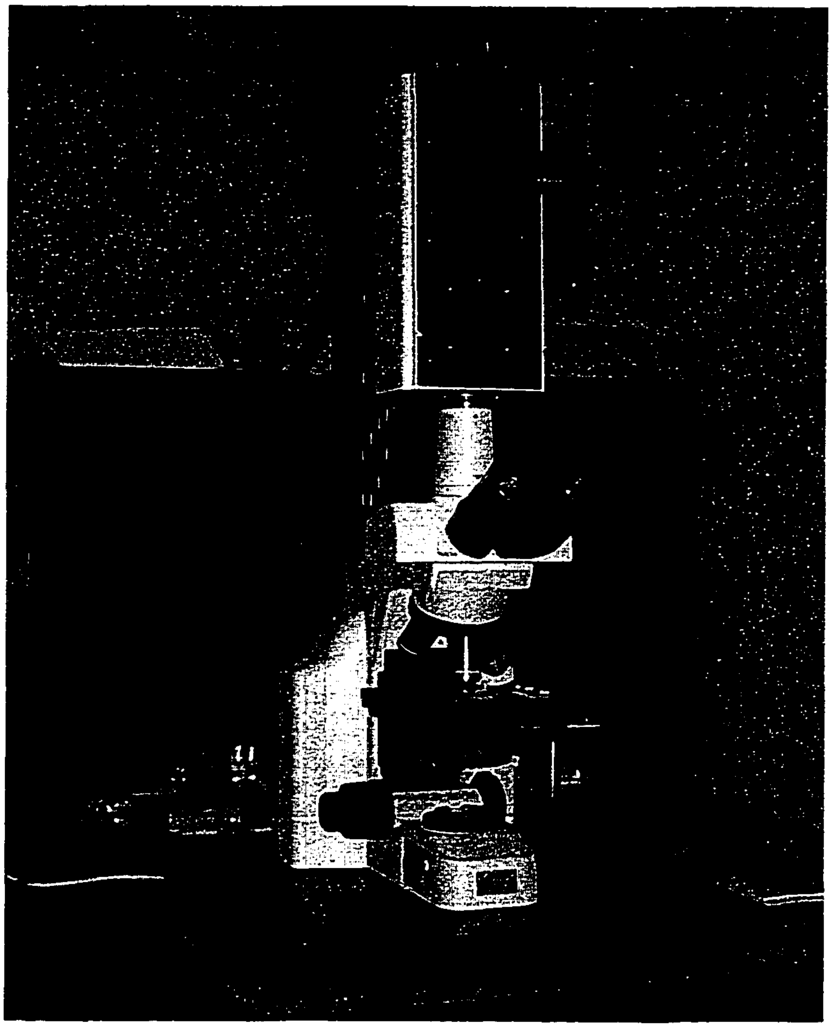

Fig. 4.1 The Nikon Eclipse E400 microscope with the MTI NC-81LX video camera mounted on the top.

4.2 Multi-resolution Implementation and Computational Efficiency

One particularly important implementation issue was the computational performance. While the above-described method is conceptually multi-resolution, the direct implementation does not take the advantage of the computational efficiency usually obtained with multi-resolution techniques as used in pyramidal schemes [96]. The reason for the diminished computational efficiency is that the original image is always used as the signal for convolution with the various filters. Thus, the computation load is high for the lower frequency bands, where the Gabor filters have increasingly wider effective support or size, covering a greater part of the image and processing more points (Fig. 4.2). Table 4.1 illustrates the time spent in producing a segmented image, i.e. Gabor wavelet transform (filtering), feature generation and normalization, and feature clustering.

The first two stages – Gabor filtering and feature generation take most of the time because they involve convolution of the original image with various-sized Gabor filters or the smoothing Gaussian windows. The computation time grows approximately exponentially with filter size. To deal with this problem, we reduced the size of the original image by the scale in accordance with the level (scale = 2^{level}). This allowed us to use the small Gabor filter originally used at the high-resolution level across all levels instead (Fig. 4.3). The size of the Gabor filter support was chosen as a multiple of the standard deviation of the Gaussian envelope. The actual computation time data when multi-resolution implementation was utilized are shown in Table 4.2. The filter size before and after the multi-resolution implementation is shown in Table 4.3.

The reduction in computation time is attributed to the fact that for the lower levels, not only do we avoid the larger size of the low frequency filters, but we also have a smaller image to work with. This reduces the computation time at the lower level by a factor of 16. There was a loss of detailed image information using this multi-resolution approach after down-sampling the original image. The main loss of information was in the sharpness of the boundaries for the segments with varying low frequency contents. Since these contents are intrinsically low resolution spatially in order to capture texture variations of more global significance, this implementation to increase computational efficiency did not significantly affect our segmentation results. Further simulations indicated that using 3~4 levels and 4 orientations was appropriate for obtaining good results. Using more levels improved the over-segmentation problem, but sometimes reduced the number of independent clusters and blurred the boundaries between them. This suggested that for texture analysis, which is a combination of global and local properties dependent on image content, there is a range of resolution levels, which optimize segmentation performance. Our heuristic approach for determining the highest frequency band (See Section 3.2.1) and a specification of the number of levels and orientations appeared to give a good compromise for obtaining speed and segmentation accuracy. Further research is necessary to find analytical relationships between these parameters for a particular image content.

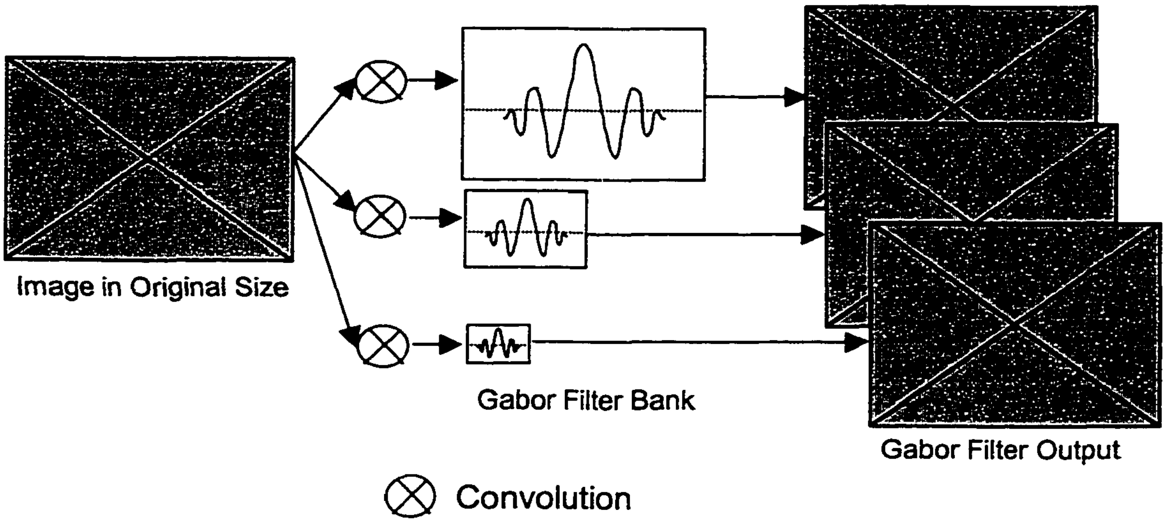

Fig. 4.2 The Gabor filtering scheme without considering computational efficiency. The Gabor filters shown are 1-D simulations.

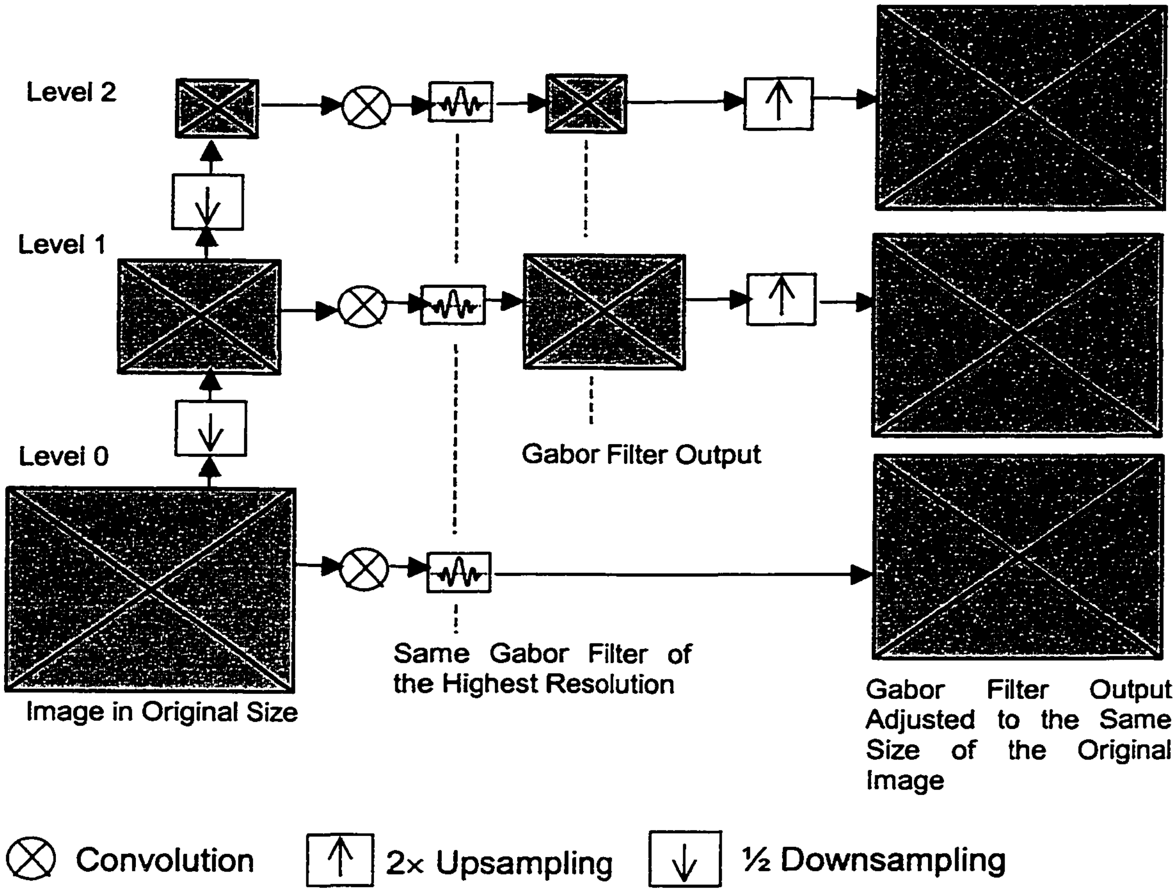

Fig. 4.3 The modified scheme exploring the multi-resolution nature of the Gabor filters. For all levels, we use the same Gabor filter as used in the highest resolution. But for lower resolution levels, we apply Gabor filters to down-sampled images, resulting in an exponentially reduced computation load.

Total Levels Employed	Computation Time Spent (seconds)			
	Gabor Filtering	Feature Generation	Feature Clustering	Total in sec(min)
3	231	195	58	484(8.07)
4	912	738	74	1724(28.73)
5	4283	3011	92	7386(123.10)

Table 4.1 Computation time when no multi-resolution implementation was used. Time was measured on a 200Mhz Pentium Pro PC. Number of Levels Employed corresponds to the number of used frequency bands in analyzing the image, counting from the highest band. In this simulation, four orientations were employed.

Total Levels Used	Computation Time Spent (seconds)			
	Gabor Filtering	Feature Generation	Feature Clustering	Total sec(min)
3	12	20	59	91(1.52)
4	18	20	75	113(1.88)
5	21	21	79	121(2.02)

Table 4.2 Computation time when multi-resolution implementation was used. Time was measured on the same 200Mhz Pentium Pro PC.

Level	Without Multi-resolution		With Multi-resolution	
	Filter Size	Image Size	Filter Size	Image Sizes
0^{th}	17 × 13	496 × 338	17 × 13	496 × 338
1^{st}	31 × 25	496 × 338	17 × 13	248 × 169
2^{nd}	63 × 51	496 × 338	17 × 13	124 × 84
3^{rd}	125 × 101	496 × 338	17 × 13	62 × 42
4^{th}	247 × 199	496 × 338	17 × 13	31 × 21

Table 4.3 Filter size and image size comparisons between implementations with and without multi-resolution.

4.3 Texture Energy Adjustment for Non-Textured Region Border

The Gabor filter based texture features identify textured regions well. There was a problem, however, when textured regions were juxtaposed with regions having almost uniform gray levels or non-textured regions. Although the texture feature does identify the area where there is no change in gray level, the border between the textured region and the non-textured region tends to be falsely identified as a region of strong texture. This phenomenon can be shown in Fig. 4.6(A~B), where the blood vessel, which is a solid gray level region, was not detected. Instead, the area along the border was blurred into a mistakenly classified nucleus region. The reason is that the cross section of the blood vessel has a circular form, and along the boundary, the sharp change of gray level responds to Gabor filter of any orientation. As a result, this small region as a whole will be considered as an area of strong texture energies along all orientations, very similar to the randomly distributed cell groups, resulting in misclassification.

Our approach to dealing with this problem was to first specify those solid-gray-level regions before the Gabor filters were applied. By doing so, we would be able to mitigate the strong energy effect along the region border later. To single out those solid regions, we examined the gray level standard deviation within a small neighborhood. If a 7 × 7 small neighborhood has a gray level standard deviation below a given threshold (for example, 5), this pixel is classified as belonging to a solid or non-textured region.

The first scan produces a binary image with all the candidate solid-region pixels recognized. There was no clear line between real solid regions and small solid areas inside a textured region. A simple approach was to dismiss the entire region if the area (pixel count) is below a threshold value. The threshold was empirically set by the user depending on the image content. The solid regions were identified using a blob-coloring algorithm to label all stand-alone regions with a sequential number (color). Let x_c denote the image value of the current pixel, and x_u and x_l denote the values of the immediate upper and left pixels, respectively. And let the color of a particular pixel x be denoted as $C(x)$. This algorithm is illustrated in Fig. 4.4.

With this blob-coloring algorithm, we obtained all the individually colored and separated regions. We then traverse these regions and eliminate the ones with area smaller than the threshold. The remaining regions were the solid gray-scale regions we were attempting to identify. With these regions marked, we developed a scheme to reduce the high texture energy along the their borders as follows.

Since we use a Gabor filter bank with multiple orientations, it is natural to infer that among all orientations there likely will be one orientation, along which the texture energy is affected the least. For example, suppose we have two regions bordering each other horizontally as in Fig. 4.5 (dotted rectangular area). The filtering result shows that the texture energy will be the highest for the Gabor filter with the 0° orientation, and smaller with the 45° and 135° orientations. The texture energy reaches the minimum value from filter with the 90° orientation.

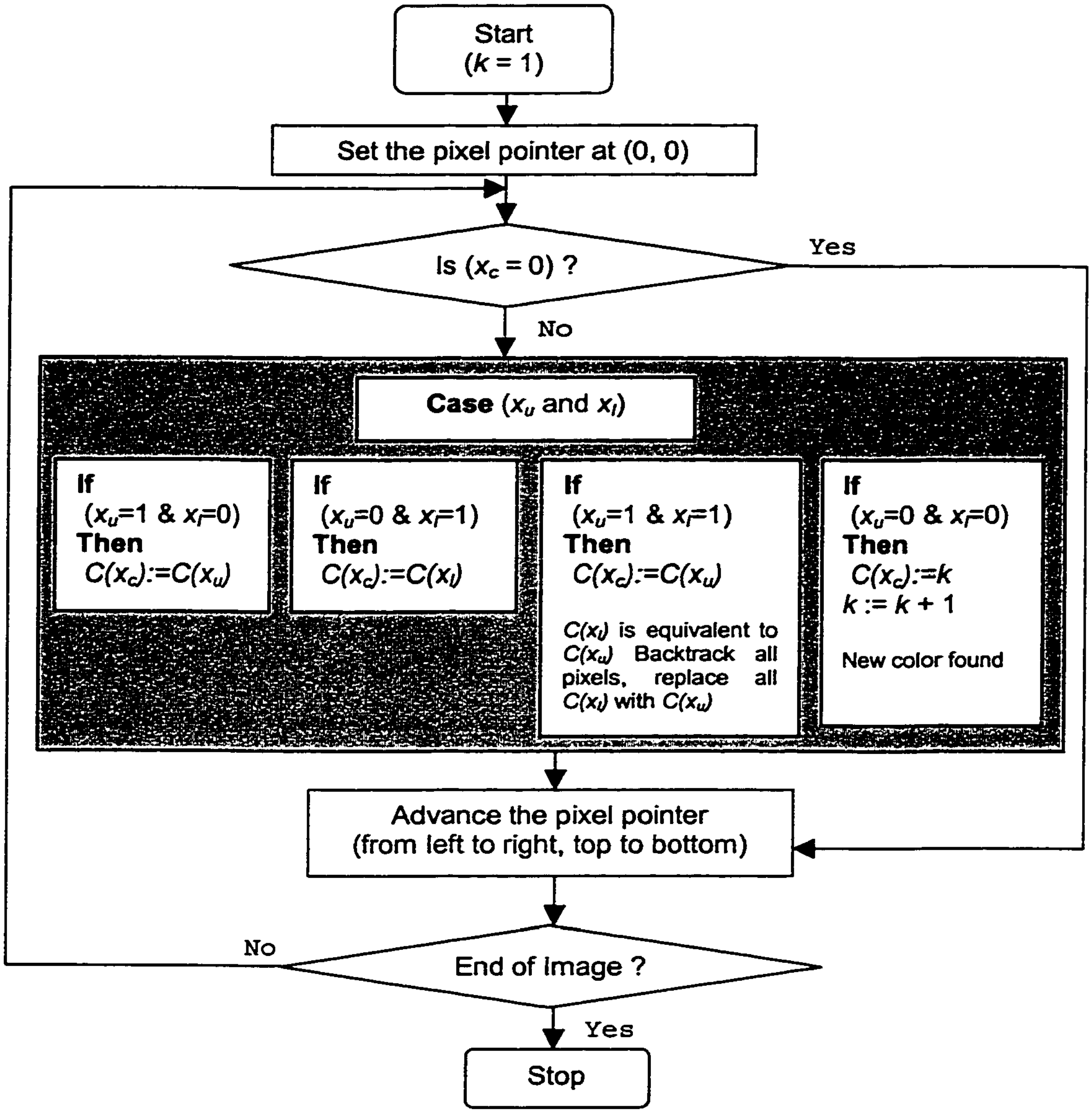

Fig. 4.4 Flow-chart of the blob-coloring algorithm.

Averaged texture energies along different orientations (of the dotted area to the left)			
0°	45°	90°	135°
0.569	0.448	0.278	0.429

Fig. 4.5 Illustration of the orientational difference of texture energy along the border of textured and non-textured regions. For the dotted area, the lowest energy is shown to be along the 90 degree, as the texture contrast is the least along this direction.

To minimize the effect of the border among textured and non-textured region, we will adjust the texture energies at a pixel located near the border area with new values. For each frequency band and orientation, the new value is determined to be closer to the smallest value among all orientations in the same band. We developed the following method to derive this new value:

First, we scan each pixel of the feature image (before the stage of feature smoothing) of each resolution level, with a neighborhood window centered on the pixel in question. The size of the windows is determined as the same size as the smallest filter kernel size, which was used in feature generation (The size was the multiples of the standard deviation of the Gabor filter in our implementation). For each center pixel, we count the number of pixels inside that neighborhood window that belong to a non-textured region, together with the total area of the neighborhood window, and calculate the area ratio:

$$R = \frac{\text{pixel count of non-textured area}}{\text{pixel count of total area}} \qquad (4.3.1)$$

When the ratio *R*, is 1 or 0, then the pixel in question is not near the border and the pixel's texture energies are not altered. If *R* is 0.5, then the texture energy in each frequency band and orientation is replaced by the minimum value in the same frequency band. At the lower resolutions, the false texture energy at the boundary is distributed over a wider spatial extent. Thus, we would like to move *R* toward 0.5 even more when the resolution is lower. We will, therefore, use an $R_{adj}(l)$ as an adjusted ratio to offset the influence of different resolutions as a function of the current level l (the level 0 denotes the highest resolution level). If L denotes the total number of levels used, then $R(l)$ is defined as *R*, the ratio calculated normally as Eq. (4.3.1), plus an adjustment part, R_{adj}, which is meant to put it closer to 0.5 when the resolution is lower. This is given by:

$$\begin{aligned} R(l) &= R + R_{adj}(l) \\ R_{adj}(l) &= (0.5 - R)\cdot\frac{2^l - 1}{2^l} \end{aligned} \qquad (4.3.2)$$

The adjustment part, R_{adj}, exerts the minimum influence when the resolution is the highest, i.e. $l = 0$. When the resolution is the lowest, $l = L\text{-}1$, then:

$$R(L-1) = R + (0.5 - R)\cdot\frac{2^{L-1} - 1}{2^{L-1}} \qquad (4.3.3)$$

Comparing Eqs (4.3.2) and (4.3.3) shows that as we go to lower resolutions, the ratio $R(l)$ is closer to 0.5.

Texture energy will be affected the most when the ratio is near 0.5, and will be affected the least when it is near 0 or 1. We define an effect index, $E(l)$, as:

$$E(l) = 2 \cdot |R(l) - 0.5| \tag{4.3.4}$$

$E(l)$ will have the value 0.0 when it has the most effect, and have the value of 1.0 when it has the least effect. Based on the index E, for each band of the texture-energy feature image, we find the lowest energy among all orientations, denoted as $e_{min}(x, y)$. Whenever the pixel centered in the pre-defined neighborhood window is classified as near the border with an R not equal to 1 or 0, then, for each band and orientation combination, we will have the adjusted texture energy defined as:

$$e(x, y) = e_{\min}(x, y) + [e(x, y) - e_{\min}(x, y)] \cdot E(l) \tag{4.3.5}$$

Using this method, an improved segmentation result can be obtained, which is shown in Fig. 4.6(C).

Based on our uniform region preclusion algorithm, a combined textured and non-textured region segmentation is possible. Not only are textured regions identified, but also non-textured regions can be further discriminated based on their gray level differences. That is, we can combine the texture property and the gray-level property to develop a universal segmentation system.

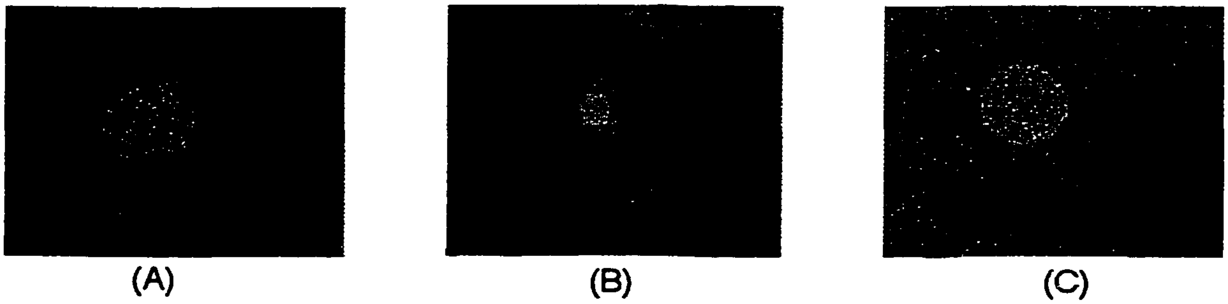

Fig. 4.6 Result of the texture energy adjustment along the border region. (A): A portion of the original abducens image with the cross-section of the blood vessel, which is a non-textured region (B):The segmentation without the consideration of energy adjustment, the area along the perimeter of the blood vessel was mistakenly classified as high energy textured region, (C): The improved segmentation with the border region texture energy adjustment.

4.4 Relaxation

Brute-force segmentation usually gives rise to the problem of over-segmentation, which is characterized by scattered holes in a presumably solid region. It makes sense to take measures to minimize this effect. Relaxation is a necessary step to produce a more coherent segmentation result.

4.4.1 Additional Features for Relaxation

From the texture energy obtained from the Gabor wavelet transform, we construct the dominant aspects of the feature vector. During the course of this research, we experimented with a few methods to incorporate some spatial constraint, in order to improve the relaxation and blob characterization [69]. As an initial attempt, we utilized the pixel coordinates (x, y) as two additional features [22]. The idea is that two spatially proximate pixels are more likely to be grouped into the same region than two pixels far apart spatially. Using pixel coordinates proved to be beneficial in producing more solid regions, though it was necessary to normalize these features.

In addition to the pixel coordinate features, we included in the feature vector the Gaussian smoothed image gray level intensity at that pixel coordinate. This added feature was computed separately at each scale. This feature is a measure of the steady state DC component of the texture, which is filtered out by the Gabor wavelets. This idea has been experimented with before. Unser [68] used four 2×2 Hadamard masks, along with three directional derivative masks, which also include a DC mask to measure the DC component of the texture element. We incorporated this looking-from-a-distance texture information in our texture feature vector. In order to achieve a normalization of texture features, this Gaussian smoothing used the same standard deviation as the Gaussian used for smoothing the texture energy features (Eq. 3.2.7). In addition, the output of the smoothed intensity feature was also normalized.

4.4.2 Probabilistic Relaxation Labeling

Even though we obtained better result with the additional features described above, over-segmentation still occurred at times as there were unwanted holes in the nuclear group and some isolated cell groups of very small area, requiring more robust relaxation schemes. Formally, relaxation is a process which explores the local relationship of image parts and establishes an adjustment procedure in order to achieve a globally more consistent interpretation of a picture [97]. There are two kinds of relaxation processes. One is discrete relaxation labeling when the set of labels are definitively associated with picture parts; the other is continuous or probabilistic relaxation labeling when the labels are associated with picture parts with a likelihood.

Generally, a probabilistic relaxation process is organized as follows [97]:

1) A list of possible labels is independently selected for each pixel, based on its intrinsic characteristics. A measure of confidence can also be associated with each possible label.
2) The possibilities (and confidences) for each pixel are compared with those for related (neighbored) pixels, based on a model of the relationships between the possible labels of pixels. Labels are deleted or confidences are adjusted to reduce inconsistencies.
3) Step (2) can be iterated until some criteria are achieved or a pre-specified maximum number is reached.

Specifically, Let $\{A_1, \ldots, A_N\}$ be the set of objects and let $\{L_1, \ldots, L_K\}$ be the set of possible labels of classes. With each object A_i, there is an associated estimate of the probability distribution of A_i having label L_j, $j = 1, \ldots K$, $(P_i(L_1), \ldots, P_i(L_K))$. These estimates form a probability vector. It is assumed that:

$$0 \le P_i(L) \le 1, \qquad \sum_{j=1}^{K} P_i(L_j) = 1 \tag{4.4.1}$$

For each pair of neighboring objects A_i and A_j and each pair of labels L_h and L_k, there is a compatibility measure $r_{ij}(L_h, L_k)$, e.g., in the range [0, 1]. These coefficients indicate the degree to which classifying A_i into class L_h is compatible with classifying A_j into class L_k. Usually the value 0 indicates complete incompatibility and 1 means total compatibility. There are varieties of choices for the compatibility measures, and there are as well several iterative updating rules that adjust the probabilities of how each point is influenced by neighboring points. Two most important methods are described as follows.

The Rosenfeld-Hummel-Zucker (*R-H-Z*) algorithm [98]:

$$P_i^{(m+1)}(L) = \frac{P_i^{(m)}(L)(1+q_i^{(m)}(L))}{\sum_{l=1}^{k} P_i^{(m)}(L_l)(1+q_i^{(m)}(L_l))} \tag{4.4.2}$$

where

$$q_i^{(m)}(L) = \frac{1}{J}\sum_{j=1}^{J}\sum_{l=1}^{K} r_{ij}(L,L_l)P_j^{(m)}(L_l). \tag{4.4.3}$$

Here J is the set of all neighbors of element A_i. The function $r_{ij}(L, L_l)$ in the R-H-Z rule is empirically determined. Previous work by Hsiao [99] has shown that another algorithm originally proposed by Peleg [100] converges much faster than the *R-H-Z* algorithm. The Peleg's scheme is described as:

The Peleg's algorithm [100]:

$$r_{ij}(L_h, L_k) = \frac{P(A_i \in L_h, A_j \in L_k)}{P(A_i \in L_h)P(A_j \in L_k)} \tag{4.4.4}$$

and

$$P_i^{(m+1)}(L) = \frac{1}{J}\sum_{j=1}^{J}\frac{\sum_{l=1}^{K} r_{ij}(L,L_l)P_i^{(m)}(L)P_j^{(m)}(L_l)}{\sum_{h=1}^{K}\sum_{l=1}^{K} r_{ij}(L_h,L_k)P_i^{(m)}(L_h)P_j^{(m)}(L)} \tag{4.4.5}$$

In our research, we have used Peleg's algorithm, and the result has been shown in Fig. 4.7(A~B).

(A)

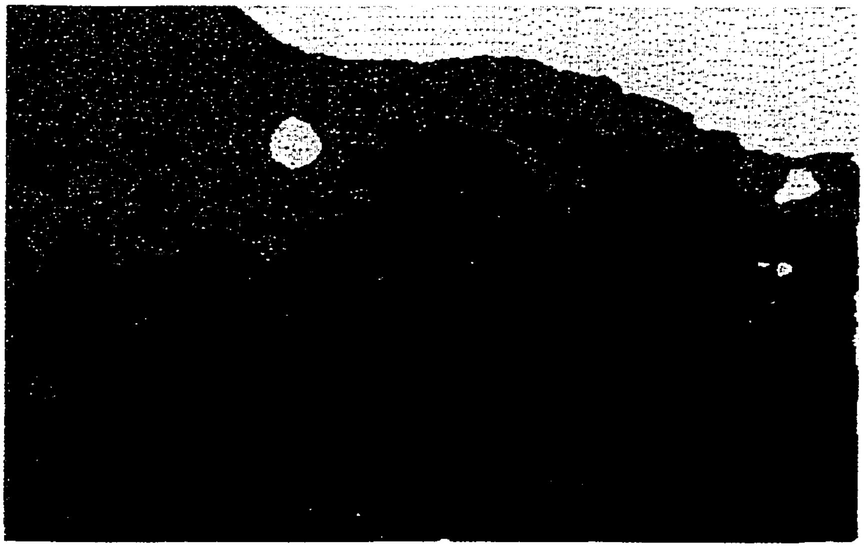

(B)

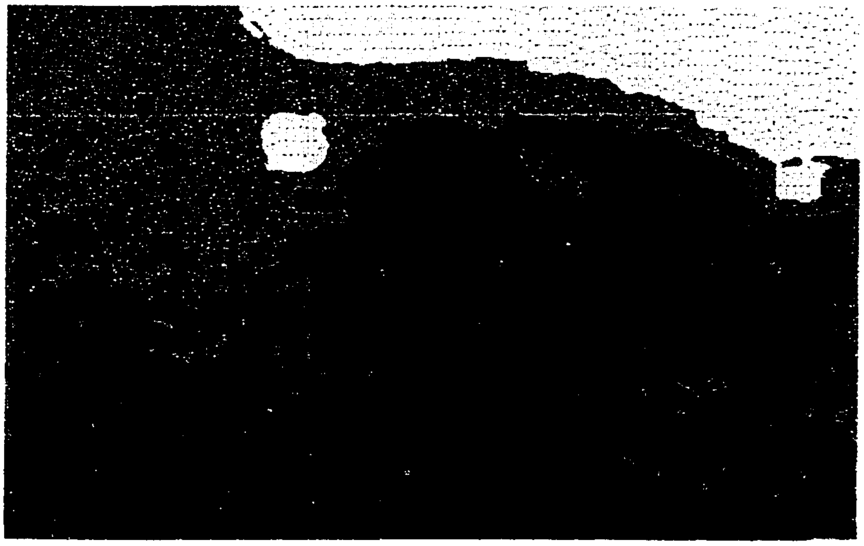

Fig. 4.7 Effects of the probabilistic relaxation. (A) The segmentation results before relaxation. It showed some holes in a supposedly homogeneous textured region (B): The segmentation results after Peleg's relaxation (4 iterations). Textured region appeared to be more solid and cohesive.

CHAPTER 5. RESULTS

In this section, we first show the application of the texture based segmentation algorithm to identifying simulated images. We study the dependence of texture structure, such as cellular density, size of cells, orientation and regularity of cell distribution on the discriminating power of the Gabor wavelet filters. This demonstrates how size, shape and orientation affect the texture-based discrimination algorithm. We then show the application of the method to neuro-anatomical images, which contain abducens and vestibular nuclei.

5.1 Results Applied to Simulated Texture Patterns

5.1.1 Discriminating Properties of the Gabor Texture Feature

Four panels of simulated pictures were constructed, which consist of black circles on uniform white background (Fig. 5.1). They simulate small cells randomly distributed (Fig. 5.1(A)), small cells uniformly distributed (Fig. 5.1(B)), small cells randomly but sparsely distributed (Fig. 5.1(C)), and big cells randomly distributed (Fig. 5.1(D)). The plots of the averaged texture energy for the first panel against each one of the remaining simulated images are shown in Fig 5.2A, Fig 5.2B, and Fig 5.2C, respectively. For each of the images, we used Gabor filters of four frequency bands with the highest frequency band having a center frequency u_{0max} as defined in Eq. (3.2.4). Four orientations are used, which are 0°, 45°, 90° and 135°, so that a total of 16 features were employed.

Fig. 5.2A shows that, compared with the normal cell distribution as Panel A, the more regularly distributed texture image (Panel B) has a strong oscillation in one of the frequency band (feature #5~#8). In addition, the texture energy of Panel B drops off quickly at the lowest frequency band (feature #1~#4). This is because the regularly arranged cell pattern has uneven cell density distributions along different orientations, and will have sawtooth form in some band. Instead, the random distribution has no preferred directionality, and consequently will be relatively flat across all frequency bands. Thus, the variation of the texture energy within a frequency band could be an strong indication of the regularity of the cell distribution. Additionally, the regularly distributed cells will more likely merge into a solid region when resolution drops to a certain level, which is shown in the sharp drop of the texture energy of Panel B at the lowest resolution. The pattern at the highest resolution (feature #13~#16) for the two panels, however, remains almost identical. This is because at the finer resolution the overall texture energy is dominated by the local attributes, i.e., the shape and the size of the cells, instead of the regularity of the cell distribution (See Section 5.1.3 for a more detailed study of effects of shape). Since Panel A and B have the same cell size and shape with the same density, they produce very similar texture energy at the high-resolution level.

Fig. 5.2B shows the effect of cell density on the texture feature. Panel C has a very sparse cell distribution (almost a half of the density of Panel A), which is represented by the significant energy drops in the two higher resolution levels.

Fig. 5.2C shows the effect of cell size on the texture feature. Firstly, a larger cell distribution with the same intracellular spacing, in shifted-down resolution, is equivalent to a distribution having a smaller cell size and denser distribution. In our case, Panel D has cells with almost double the size of the cells in Panel A, but also has double the intracellular spacing. That means Panel D is approximately the 2× blow-up of Panel A. If we shift the texture pattern of Panel D by one frequency band to the right, the middle three bands will almost match that of Panel A. Secondly, bigger cells with large spacing tends to maintain the high energy in lower resolution levels. This is because when the resolution lowers, small cells tend to disappear and merge into the background faster than big cells with large spacing. Consequently, the texture energy for small cells will be more likely to decrease rapidly than bigger cells towards the low frequency bands.

Though simplified, the simulated results shown above, suggest that the Gabor-based texture energy feature could be used to distinguish among different subdivisions of the nucleus, as well as to discriminate nucleus from surrounding tissues.

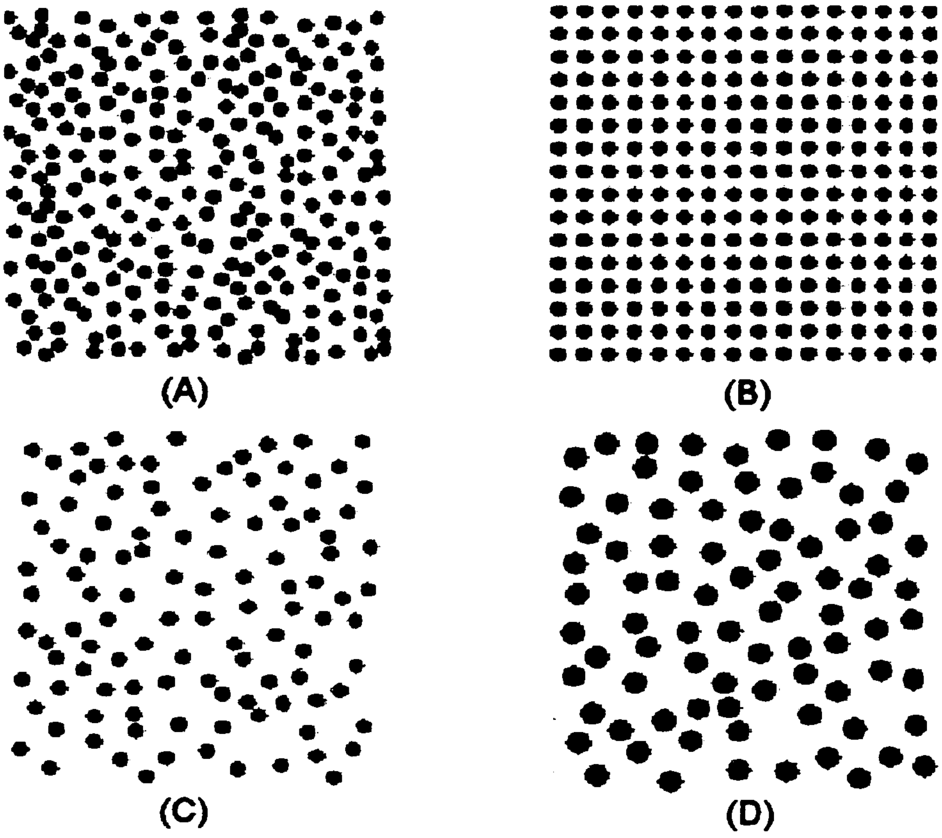

Fig. 5.1 Four panels of simulated images of different cell distributions (A): normal size, random distribution, (B): normal size, regular distribution, (C) normal size, sparse distribution, and (D) bigger size, random distribution.

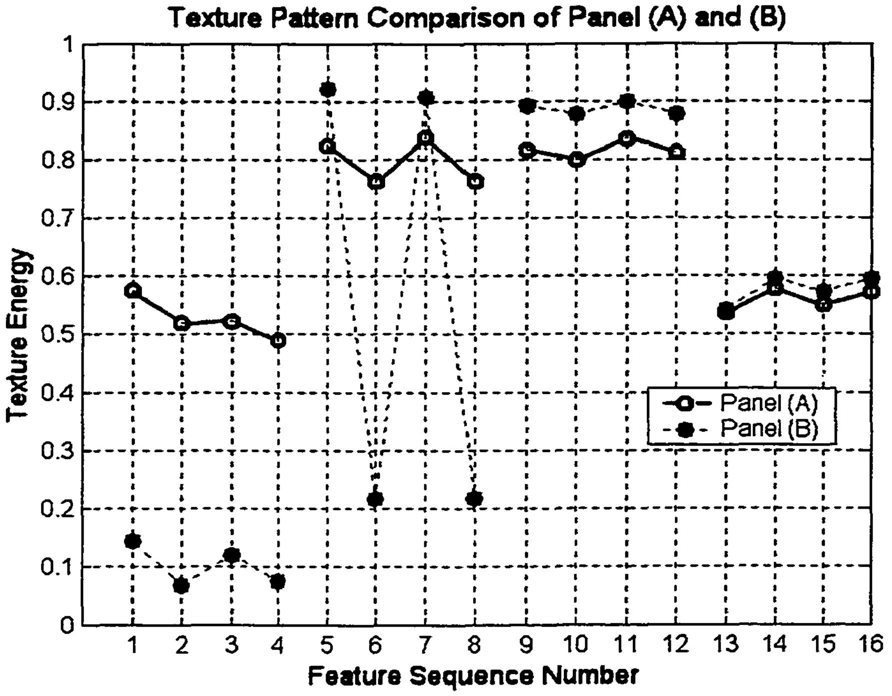

Fig. 5.2A A plot of the texture energy comparison between Panel (A) and (B).

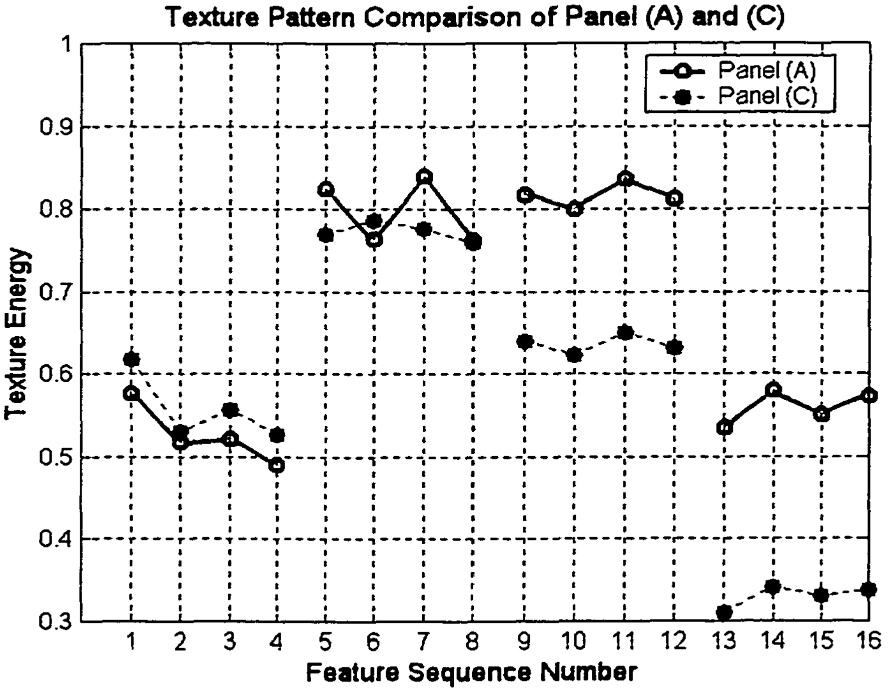

Fig. 5.2B A plot of the texture energy comparison between Panel (A) and (C).

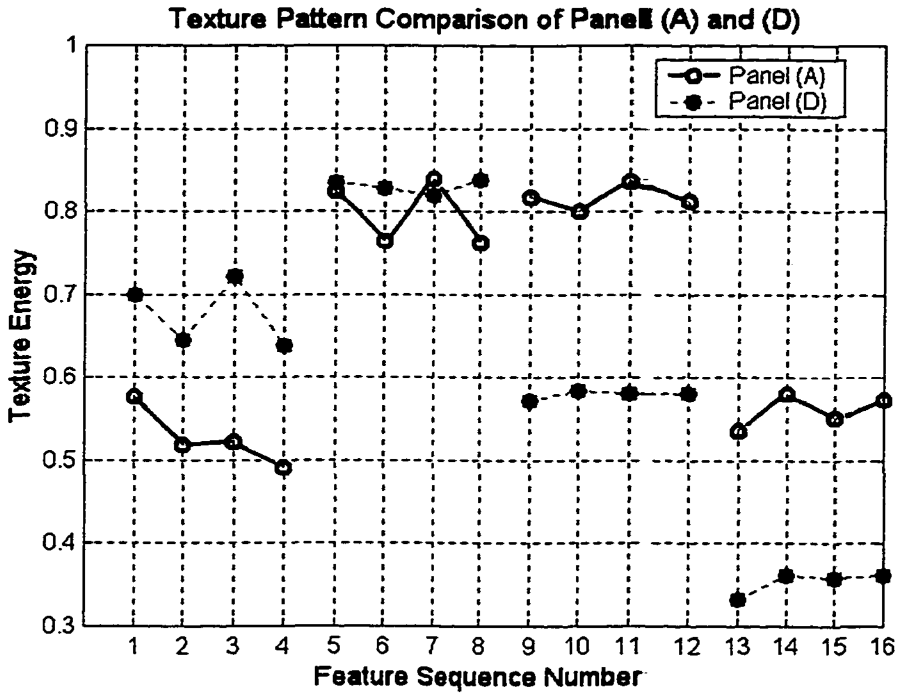

Fig. 5.2C A plot of the texture energy comparison between Panel (A) and (D).

5.1.2 Selecting the Highest Center Frequency

In Section (3.2.1), we noted that choosing the center frequencies for Gabor filters based on image-content is an important consideration. The image-content aspect is highly related to the distribution density of texture elements. In the case of neural tissues, the texture elements are cells that are the constituents of the nucleus. When the cell distribution is too sparse, the texture analysis will not be able to capture localized texture information. Because texture is based both on global and local properties, a sparsely distributed cell group tends to lose local quality as a form of texture. An example demonstrating this is shown in Fig. 5.3. Four panels of synthesized cell patterns with varying spatial distribution are shown in Fig. 5.3(A) (test image adapted from [98]). All of the four cell distributions are fairly sparse. If we take three frequency bands to form the texture feature, the predominant texture energy lies along the cell boundaries, and the insufficient population of cells makes it impossible to form homogeneous texture regions (Fig. 5.3(B)). Increasing the total levels to four has not helped to improve the segmentation result. However, if the simulated texture panel was downscaled by a factor of four (Fig. 5.3(C)), then using exactly the same parameters in our algorithm, all four panels now have formed solid regions (Fig. 5.3(D)). This phenomenon is due to the sparsely arranged distribution of texture elements. The local characteristics related to the minute shape information of the texture elements take on the predominant role in affecting the texture discrimination. This effect could outweigh the influence of the intrinsic global texture properties, encompassed by the spatial distribution of cells. Downscaling created denser texture regions, and accentuated the spatial frequencies that better represent the texture characteristics.

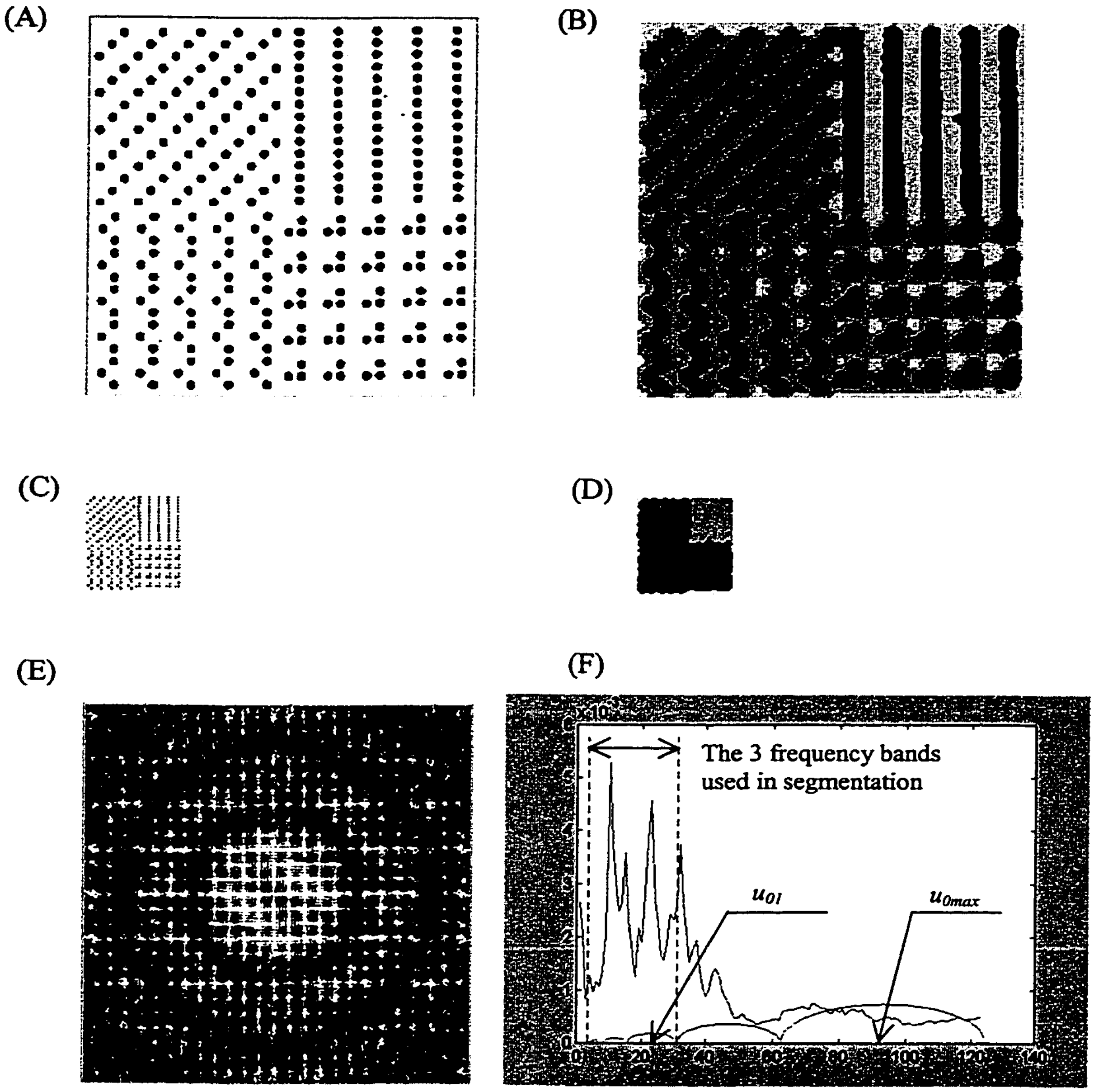

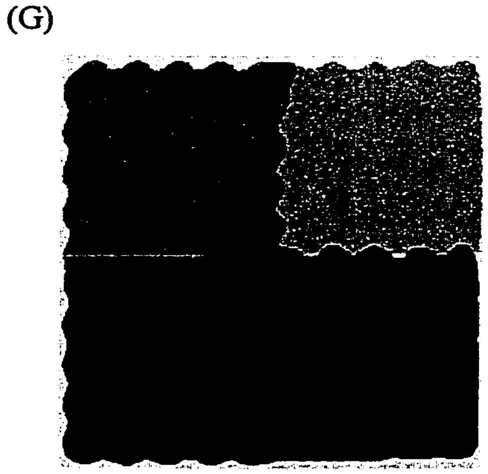

Fig. 5.3 Choosing the appropriate starting high frequency band. (A): original simulated image, (B): unsuccessful segmentation result of (A), (C): downscaled image of (A), (D): segmentation result of (C), (E): Fourier power spectrum of (A), (F): polar plot of (E), (G): successful segmentation of (A)

The multi-resolution nature of the Gabor wavelet transform has the property that downscaling the original image is equivalent to sliding the frequency bands to lower resolutions. This property helps to formulate the problem of choosing the appropriate highest frequency band, i.e. the center frequency u_{0l} (See Section 3.2.1), for characterizing the texture. The goal is to determine u_{0l} so that the following 3~4 bands used in constructing the texture feature vector cover the most significant part of the Fourier power spectrum of the original image. Fig. 5.3(E) shows the Fourier power spectrum of Fig. 5.3(A), and Fig. 5.3(F) shows the polar plot of the Fourier power spectrum of Fig. 5.3(E) superimposed on the support of the frequency bands of the Gabor filters. The default highest frequency band (centered on u_{0max}) covers a relatively small part of the Fourier power spectrum. When we chose u_{0l} to be u_{0max}, the segmentation could not form cohesive regions as shown in Fig. 5.3(B). However, if we slide the u_{0l} down by two octaves, better coverage of the peaks of the Fourier power spectrum is obtained. This produced a very coherent segmentation result (Fig. 5.3(G)). This compared favorably with our personal perception of the texture panels in Fig. 5.3(A).

5.1.3 Effects of Cell Shape on Texture Discrimination

Cell shape also contributes to determining the textural characteristics of the cell groups. In the texture feature vector we used, the elements affected most by the shape of the cell should be the output of the Gabor filter with the highest spatial frequency. This is because the high spatial frequency filter with narrower effective support can capture very localized difference of individual cells. Fig. 5.4 showed four simulated panels of texture region with varied hand-drawn cell shapes. Since the size of the cells is comparable, the texture patterns as reflected by the feature vectors are very similar in the lowest frequency band for the marked two rectangular regions (enclosed by dotted and solid lines). There were, however, distinct differences at a particular orientation, since the dotted-line region had a strong 0° orientation. Differences, however, were more evident in higher frequency bands at all orientations, as the shapes of the cells start to exert their effects at the higher resolutions. In particular, the solid-line region has a relative flat profile for the medium and high frequency bands, while the dotted-line region is marked by the dominant (horizontal) texture energy and an evident dip in energy along the 90° (vertical) orientation.

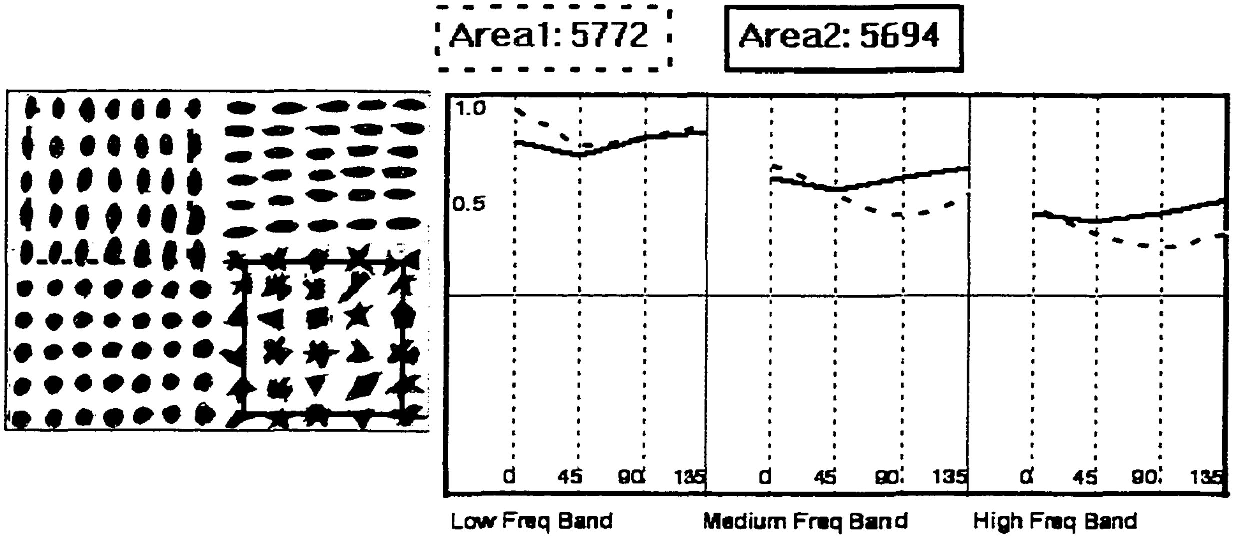

Fig. 5.4 Effects of the cell shapes on texture feature.

5.2 Texture Discrimination of the Abducens Nucleus

5.2.1 Identification of the Abducens Nucleus

The multiresolution texture analysis approach was used to analyze a number of images containing abducens nucleus. One of them ("TAZ1437L") is shown in Fig. 5.5(A) (images are provided by Dr. Jean Buettner, Munich, Germany), which shows the presence of abducens nucleus along with varying surrounding tissue, blood vessel, and the empty space of the fourth ventricle.

This image was segmented into four regions based on their texture differences. The number of regions is heuristically determined based on user assessment and specified *a priori*. Our initial choice of four regions was based on our desire to distinguish regions of empty spaces (including the fourth ventricle and the blood vessel), the area where the cell groups reside, and the brain tissues with dark and light substrates which did not have an obvious cell presence. The texture attributes were characterized by a 17-element feature vector (See Table 5.1). The first 12 of the elements of the feature were constructed using the localized spectral information as the result of Gabor wavelet transform, which were the texture energies at three frequency bandwidths and four orientations. As described above (Sec. 5.1.2), the highest center frequency u_{0l} was determined by examining the Fourier power spectrum (Fig. 5.5(B)). Fig. 5.6(A) shows the polar plot of the averaged Fourier power spectrum as the function of radius superimposed on the support of the frequency bands for the Gabor filters. The first possible high frequency band covers a small region of the power spectrum (Fig. 5.6(A)).

Therefore, we slide down one level (one octave) to pick our first center frequency so that the significant portion of the spectrum is covered (Fig. 5.6(A), the span between two vertical lines).

The next two components of the feature vector were the coordinates of the pixels. The last three elements were the Gaussian smoothed pixel intensities at three resolution levels. Based on these features, we used the partitional clustering algorithm mentioned earlier for the segmentation. The nuclear groups were identified and delineated in a semi-automated way. We specified four texture classes and the resulting segmented image is shown in Fig. 5.6(B), with different regions of interest assigned with different gray levels. Darker regions indicate higher texture energy. The segmented image shows that the abducens nucleus (region #4) is well identified.

The four cluster centers for "TAZ1437L" are shown as Table 5.1, and the first 12 features associated with Gabor wavelets are illustrated in Fig. 5.7. The data shown in the table demonstrate that the mean feature for each cluster distinctively represents its texture attribute. The neural substrates (Fig. 5.7, regions #2, #3, #4) in general have higher texture energy than the ventricle (Fig. 5.7, region #1). The trend is that the energy associated with the neural substrates rise approximately in a monotonic fashion as frequency increased. Among the neural substrates, the abducens nucleus (region #4) has the highest energy at all frequency bands and all orientations.

To demonstrate the effects of the added features of Gaussian smoothed pixel intensities at three resolution levels, we also show the segmentation result without the added features in Fig. 5.8. The added features produced regions that are more coherent and that are similar to the way in which a human would identify them.

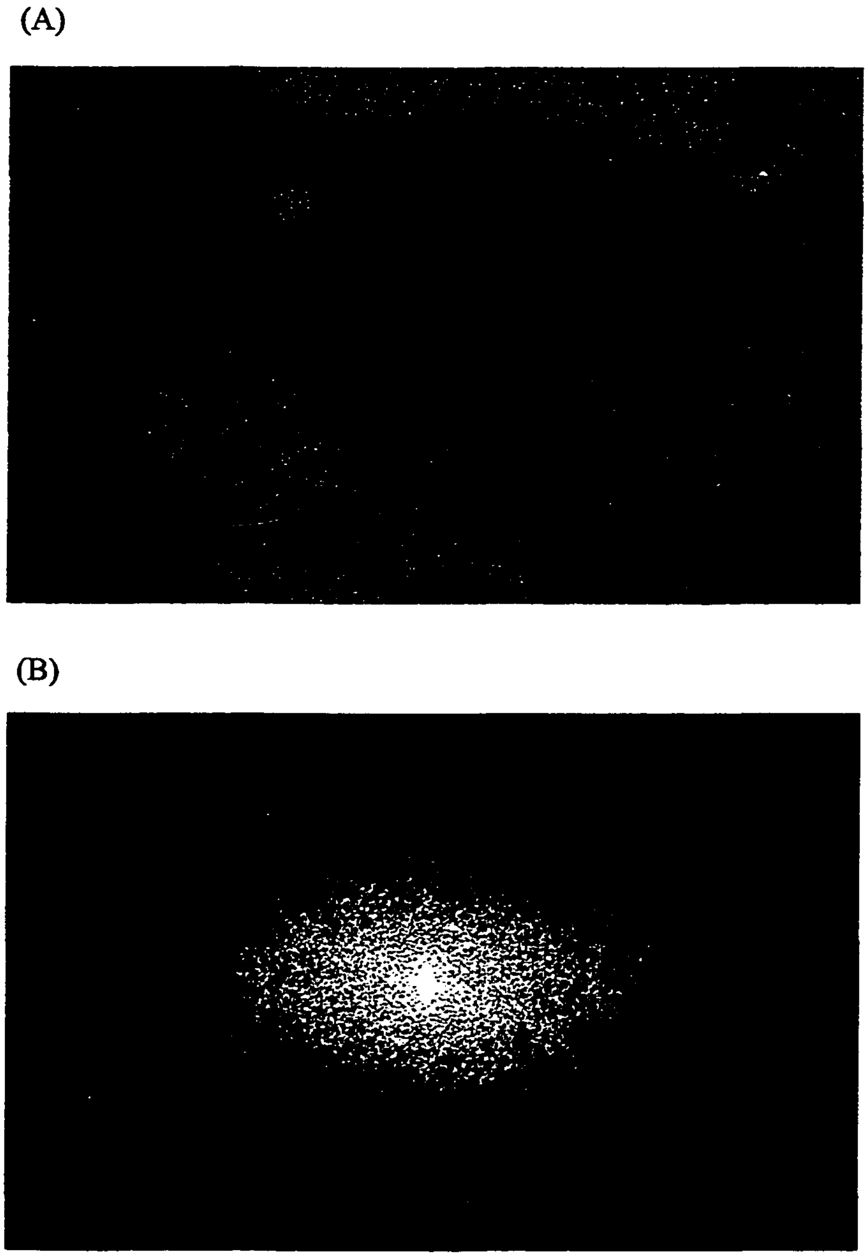

Fig. 5.5 Sample image "TAZ1427L" showing abducens nucleus and surrounding neural tissues. (A): the original image, (B) the Fourier power spectrum.

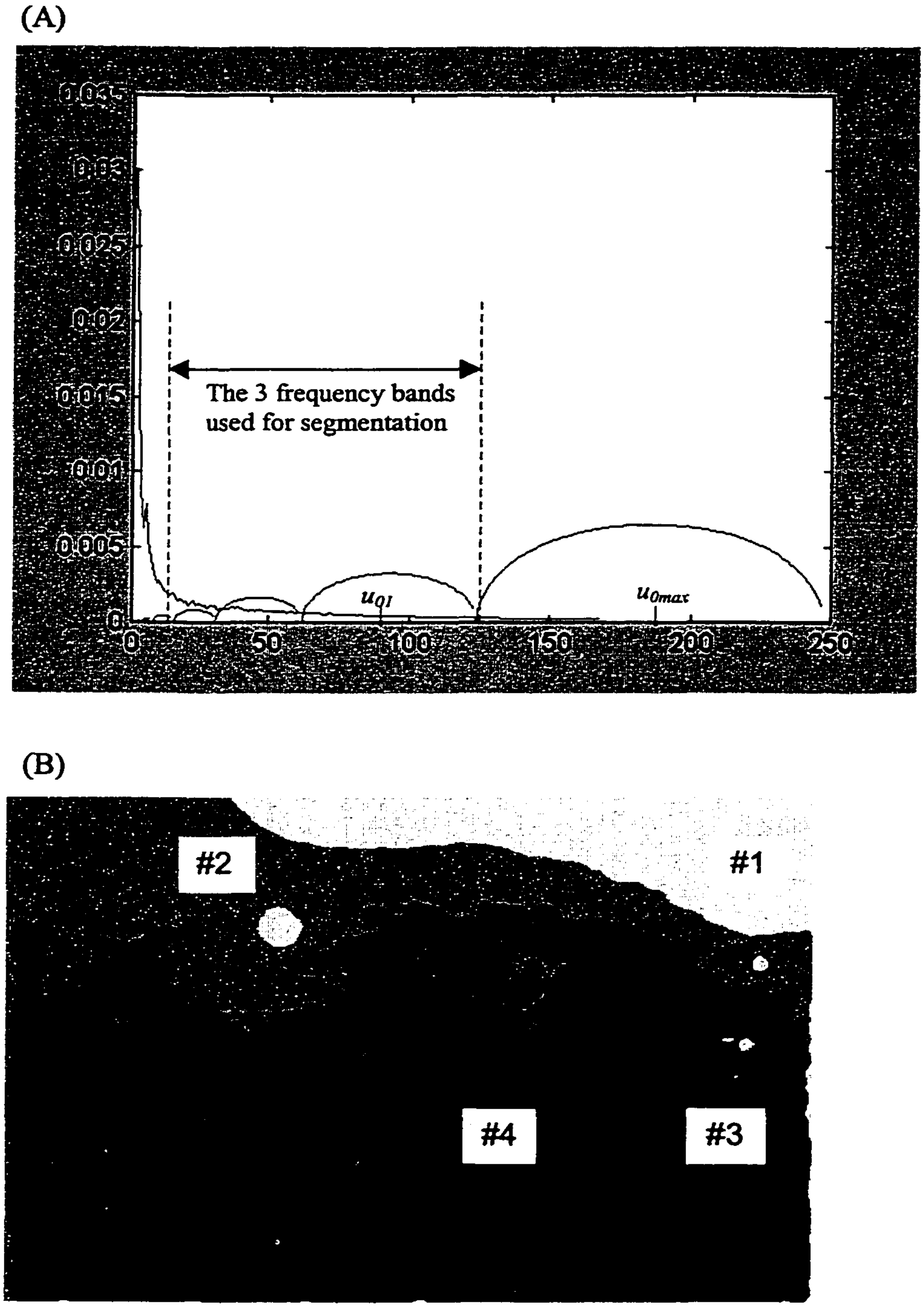

Fig. 5.6 Analysis and segmentation result of the sample image "TAZ1437L". (A): the analysis of polar Fourier power spectrum in determining the frequency bands, (B): the segmentation result when four classes are specified.

No.	Description of the texture feature	Rgn #1	Rgn #2	Rgn #3	Rgn #4
1	Freq. $3\times N_w/64$ (cycles/N_w) at 0°	0.050	0.168	0.252	0.304
2	-> same freq. at 45°	0.054	0.172	0.217	0.297
3	-> same freq. at 90°	0.066	0.194	0.223	0.328
4	-> same freq. at 135°	0.054	0.187	0.250	0.313
5	Freq. $3\times N_w/32$ (cycles/N_w) at 0°	0.051	0.287	0.334	0.448
6	-> same freq. at 45°	0.054	0.276	0.316	0.402
7	-> same freq. at 90°	0.065	0.270	0.319	0.414
8	-> same freq. at 135°	0.059	0.280	0.335	0.468
9	Freq. $3\times N_w/16$ (cycles/N_w) at 0°	0.075	0.431	0.399	0.531
10	-> same freq. at 45°	0.064	0.395	0.361	0.499
11	-> same freq. at 90°	0.076	0.346	0.380	0.483
12	-> same freq. at 135°	0.075	0.346	0.396	0.521
13	x-coordinates	0.364	0.184	0.244	0.262
14	y-coordinates	0.053	0.110	0.352	0.284
15	Pixel intensity at level 2	0.230	-0.127	0.071	-0.105
16	Pixel intensity at level 1	0.233	-0.129	0.075	-0.105
17	Pixel intensity at level 0	0.223	-0.122	0.075	-0.104

Table 5.1 Data set of the first segmentation of the sample image "TAZ1437L". Four regions were specified, with each column representing the mean feature vector of the corresponding region. For Gabor filter outputs, smaller values indicate less texture energy.

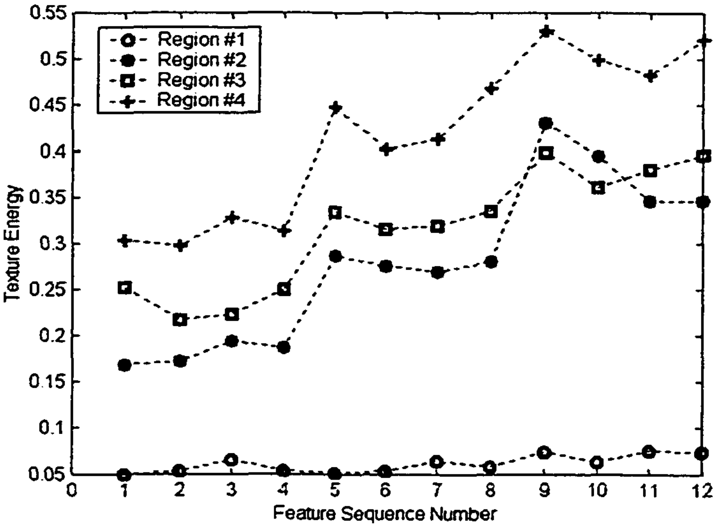

Fig. 5.7 Plot of the averaged texture feature of individual regions in Fig. 5.6(B), as the function of feature order.

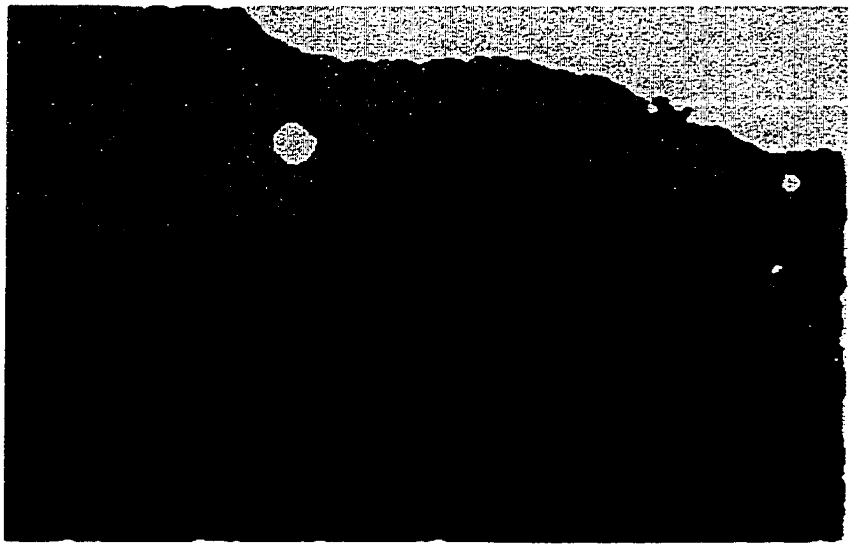

Fig. 5.8 Segmentation without the added features of the Gaussian smoothed pixel intensities. Compared to Fig. 5.6(B), it is less coherent, and the Genu of the VIIth (facial) nerve (GVII) is missing (See Fig. 5.11(A) for the labeling).

After obtaining the segmented image, we also tried to further segment the nucleus group into subdivisions with the same clustering algorithm and a different feature set as described in Section (3.2.3). One of the second-level segmentation results is shown in Fig. 5.9, where two subclasses were specified. The averaged texture feature vectors for the two regions inside the abducens nucleus for "TAZ1437L" are shown as Table 5.2, with the first 6 features associated with the Gabor wavelets illustrated in Fig. 5.10. The two sub-regions possess subtle different energy patterns, particularly in the standard deviation of energies among all orientations. This difference should characterize the variations in cell distributions within the nuclear group.

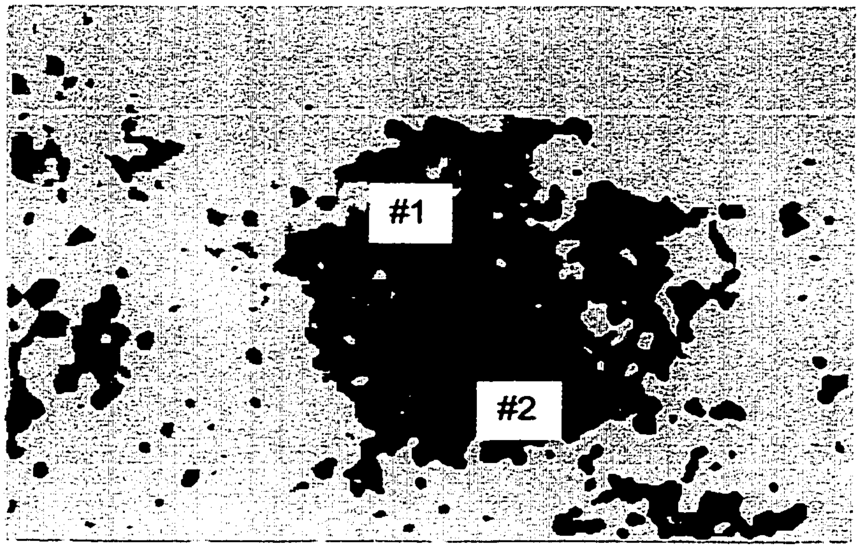

Fig. 5.9 Result of the second level segmentation of the sample image "TAZ1437L". The abducens nucleus was divided into two sub-regions.

No.	Description of Texture Feature	Sub-Rgn #1	Sub-Rgn #2
1	Mean value, Freq. 3×N_w/64 (cycles/N_w)	0.293	0.328
2	Standard deviation	0.204	0.285
3	Mean value, Freq. 3×N_w/32 (cycles/N_w)	0.428	0.439
4	Standard deviation	0.325	0.248
5	Mean value, Freq. 3×N_w/16 (cycles/N_w)	0.497	0.515
6	Standard deviation	0.291	0.262
7	x-coordinates	0.189	0.307
8	y-coordinates	0.222	0.319

Table 5.2 Data set of the second segmentation of the sample image "TAZ1437L". The last two columns are the averaged feature vectors of the corresponding subdivisions of the abducens nucleus.

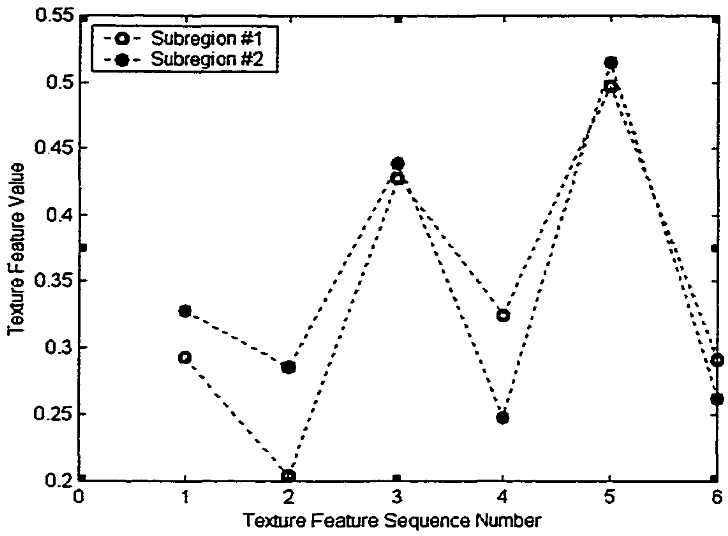

Fig. 5.10 Plot of the averaged texture features of the two sub-regions in Fig. 5.9.

The fact that the second segmentation found a separation between dorsal and ventral regions of abducens (Fig. 5.9) indicates that these regions are texturally different and might be functionally separable. These are being studied in detail by Dr. Jean Buettner. Dr. Buettner has found regions of the dorsal abducens which are anatomically and physiologically different from the more ventral portions (Fig. 5.11(A)) which is comparable to our second-level segmentation when seven subclasses were specified (Fig. 5.11(B)). The anatomical designation, however, is more limited and suggests that perhaps additional features, which have not been considered, might be necessary to effect a more subtle segmentation.

To demonstrate the consistency of the segmentation results, additional stained slices provided by Dr. Buettner were processed as shown in Fig 5.12~5.14. The achieved performances were quite similar and comparable. One important aspect of the texture-based algorithm, which is inherent in the feature vector, is that there are more features generated by the Gabor wavelets than other features such as position and Gaussian smoothed pixel intensities. This insures that the Gabor components of the texture feature are weighted more than the other features. Thus, the program by default analyzes cellular structures while the underlying shadings associated by other factors such as fibers, etc., are emphasized less, though viewing from a distance might suggest a different segmentation. An example of this phenomenon is shown in Fig 5.12. Here the shading associated with the genu of the VIIth nerve would suggest a separate segment to the human observer. The program, however, emphasizes the texture of the underlying cellular distribution and merges the regions into one. Similar results can be seen in the other images.

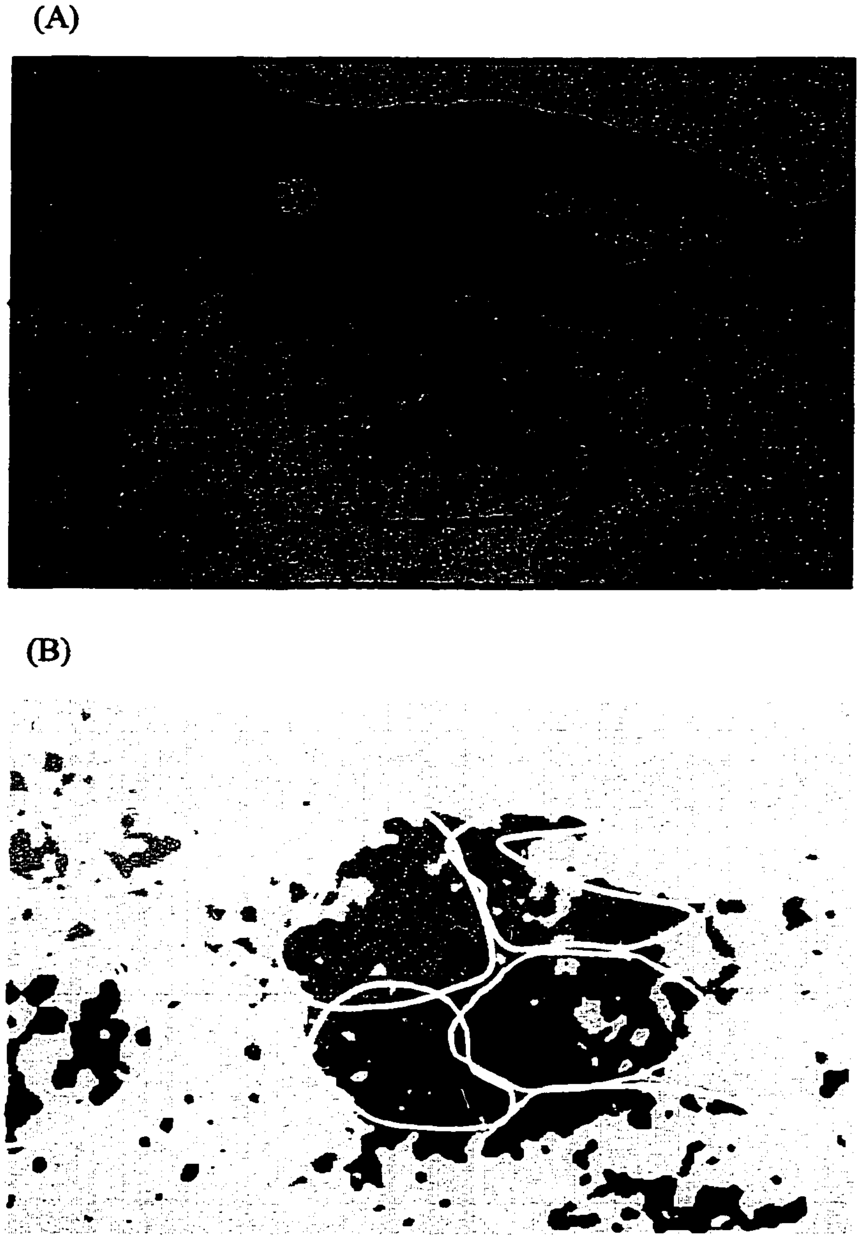

Fig. 5.11 Further subdivisions of the abducens nucleus. (A): Segmentation made by Dr. Jean Buettner in sub-dividing abducens nucleus with different functional regions. **Lv**: Lateral vestibular nucleus, **Sg**: Nucleus supragenualis, **MLF**: Medial longitudinal fasciculus, **GVII**: Genu of VII(facial) nerve, **pgd**: Paragigantocellularis dorsalis, **NVI**: Abducens nerve, **ms**: Superior portion of the medial abducens nucleus, **in**: Interior portion of the medial abducens nucleus, **ml**: Lateral portion of the medial abducens nucleus. (B): the second-level segmentation when the number of subclasses was specified as seven.

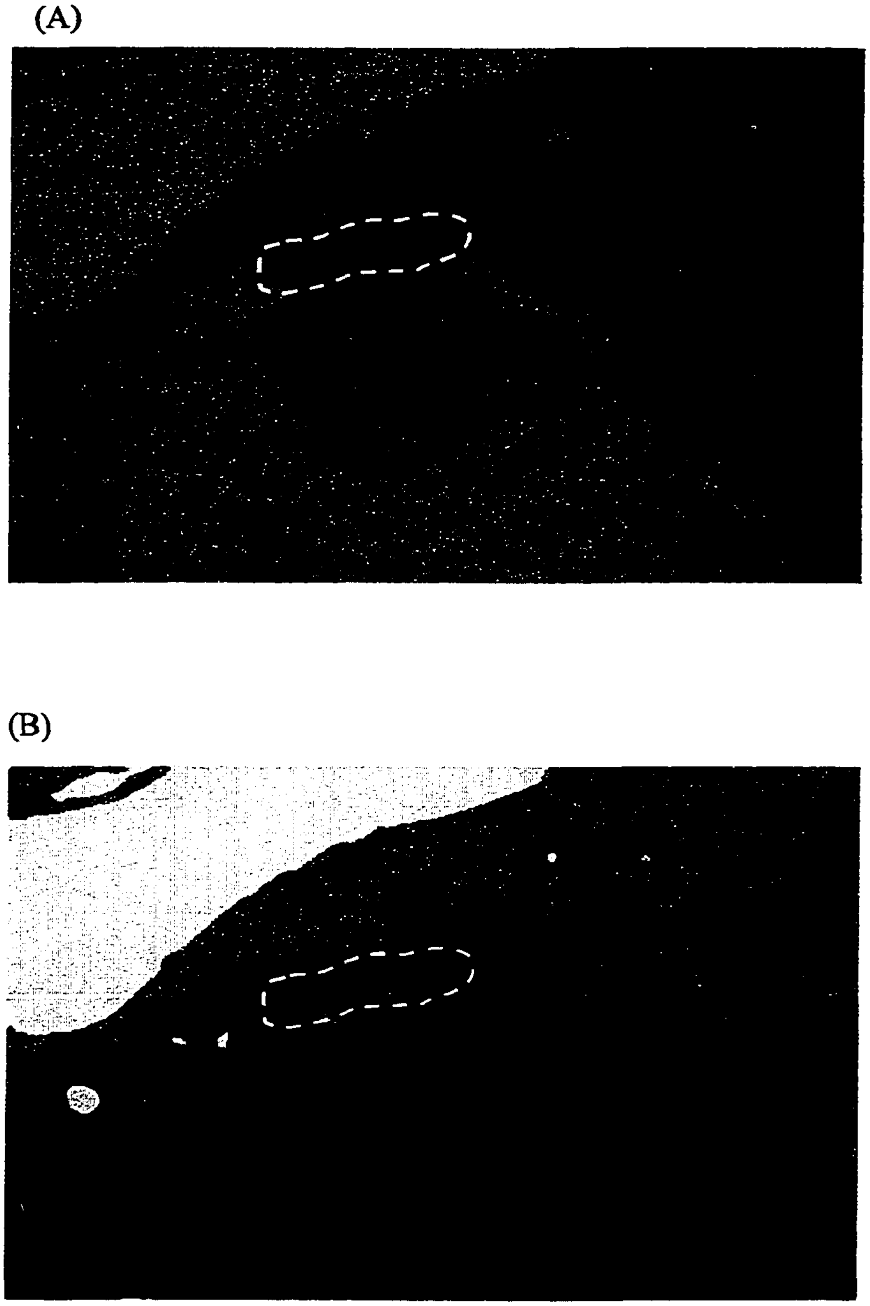

Fig. 5.12 Segmentation result of the sample image "TAZ1436R". The white dotted region is the genu of the VIIth nerve. (A) the original image, (B) result when segmented into 4 regions.

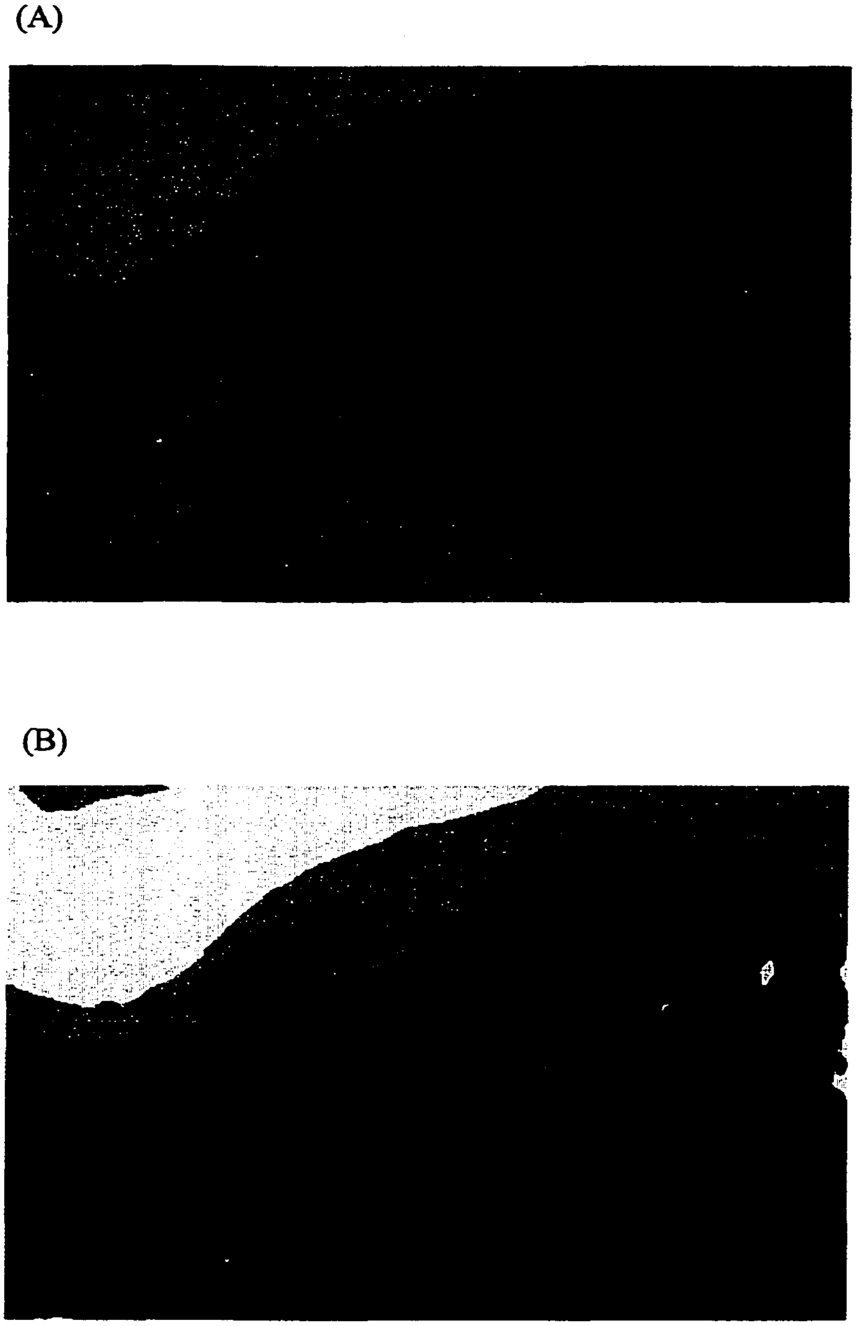

Fig. 5.13 Segmentation result of the sample image "TAZ1437X". (A): the original image, (B): result when segmented into 4 regions.

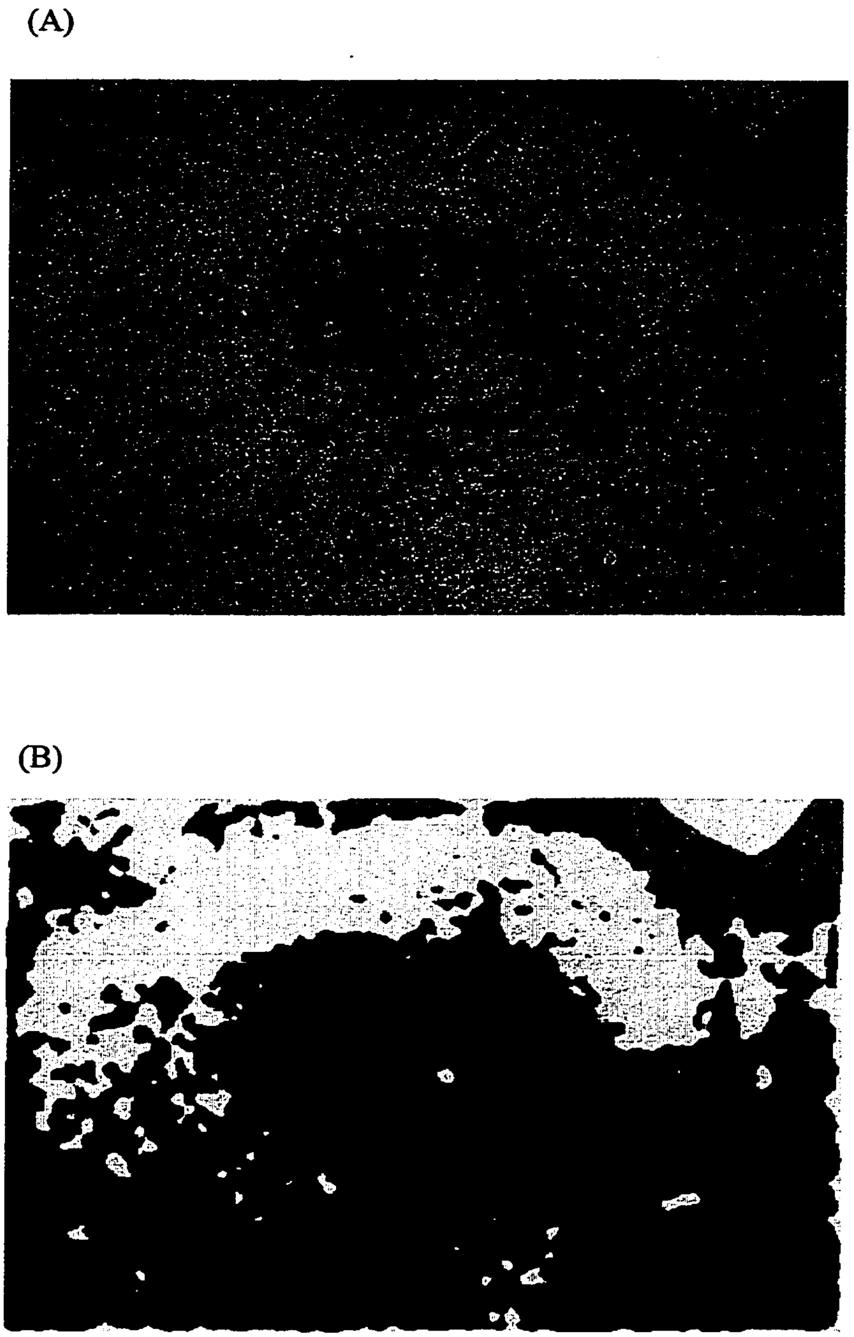

Fig. 5.14 Segmentation result of the sample image "TAZ1439L". (A): the original image, (B) result when segmented into 4 regions.

Finally, to better demonstrate the dominant cell groups, a small-blob-sifting algorithm has been employed, which works on the segmented image and sifts out all small regions and produces a cleaner-looking segmentation result. In particular, we firstly used an erode-and-dilate processing to break up weakly connected regions. Then we used the blob-coloring algorithm (see Section 4.3) to label all individual regions. Finally, we discarded all regions if the area (pixel count) is below a given threshold, and filled the discarded regions with the dominant surrounding regions. The result when applied to the segmentation of "TAZ1437L" is shown in Fig. 5.15 (pixel count threshold set at 300, compare with Fig 5.6(B)). Sometimes this kind of representation may be preferable to that produced by relaxation (See section 4.4 and Fig. 4.7).

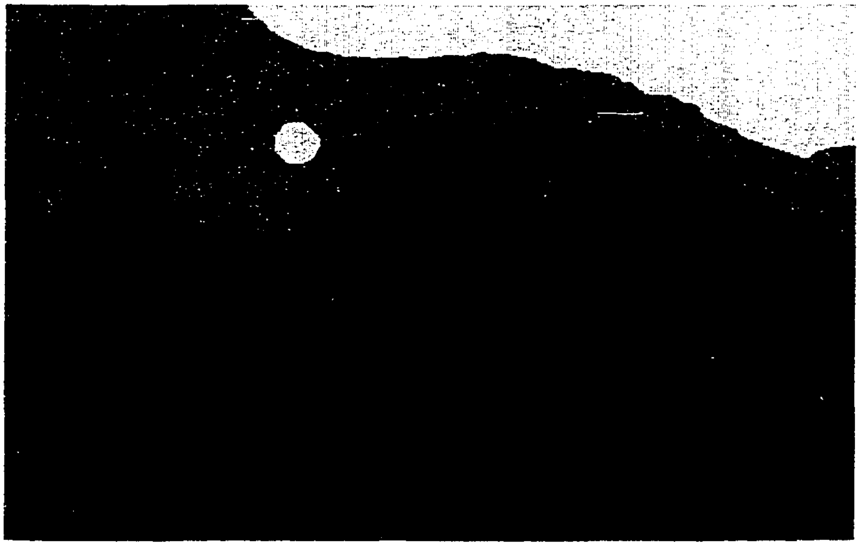

Fig. 5.15 Another view of the segmentation result of Fig 5.6, while tiny small regions (pixel count < 300) were sifted out.

5.2.2 Effects of Orientation Resolution on Texture Discrimination

We implemented the program so that the user is allowed to choose the orientation resolution arbitrarily. Experiments showed that orientation resolution higher than $\pi/4$ did not give results that were better or more consistent than human visual segmentation. Fig. 5.16 shows the comparison of the segmentation of the same input image (Fig.5.5(A)) using an orientation resolution of $\pi/6$ instead of $\pi/4$. The higher orientation resolution resulted in the inclusion of certain regions into the nucleus, which perhaps should not be included. Thus, the results suggest that optimal segmentation may be achieved by a compromise between the number of orientations and levels which are close to the values chosen heuristically in this study.

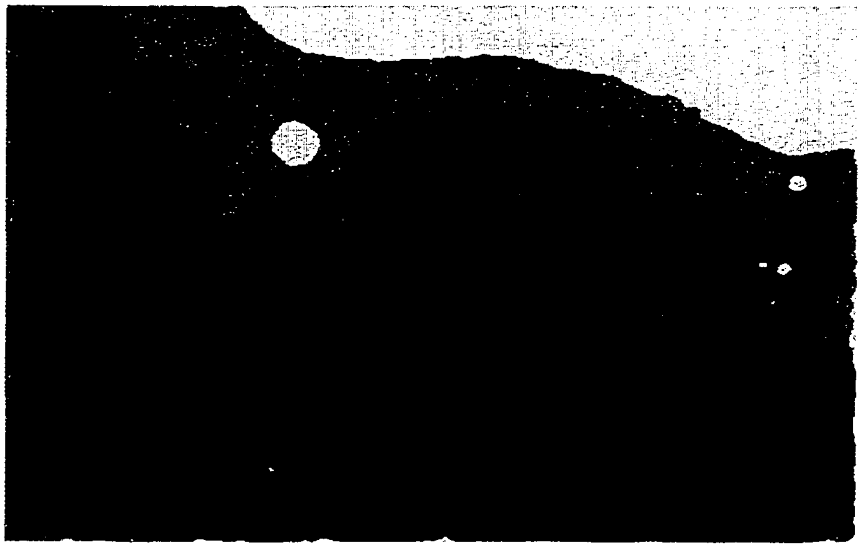

Fig. 5.16 Effects of higher orientation resolution on segmentation result

5.2.3 Reconstruction of the Original Texture with Texture Features

The design of the Gabor filters ensured that almost all of the frequency and orientation contents of the original image were covered in the frequency domain. However, there was considerable transformation of information in the determination of the feature vector. We therefore wished to determine, at each step of the feature determination how well the image could be reconstructed. We first summed the output of the entire dominant Gabor filter set we used to construct texture feature, which could be considered as an approximation of the inverse Gabor wavelet transform. The result, when properly scaled, should resemble the original textured image. One of the reconstruction examples using image "TAZ1437L" is shown in Fig. 5.17. Since we used four levels in the middle of the frequency band (sliding down by one octave), we notice insignificant losses both in minute details and in low frequency components including the DC component. Thus, a reconstructed image from the Gabor filtered coefficients, is still a good approximation of the original image (Compare Fig. 5.5(A) to Fig. 5.17). Since we used non-linear transform and absolute value of the Gabor filter output to produce texture feature, however, it affected the reconstruction process. Fig 5.18~5.20 show the progressive loss of detailed image information as it affects the image reconstruction. The image could be reasonably reconstructed by summing the nonlinear transform of Gabor filtered output, the second stage of processing (Fig. 5.18), but we see the effect of higher contrast. That is due to the reduced output range as the saturating result of the nonlinear transform (Eq. 3.2.6), which caused the contrast to be increased when the reconstructed image was scaled to fill the 256 grayscale levels. Fig. 5.19 is the reconstruction by summing the Gabor filtered output after both nonlinear transform and taking the absolute value. Fig. 5.20 shows the reconstruction by summing the actual texture energy feature as the result of Gaussian feature smoothing. The more modification we made to the raw data of the Gabor transform, the more detail we lost in the reconstructed image (Fig. 5.20). However, the resultant image still bears some similarity to the original image. It should be noted that the detail loss allowed for a better global texture characterization that makes the segmentation possible.

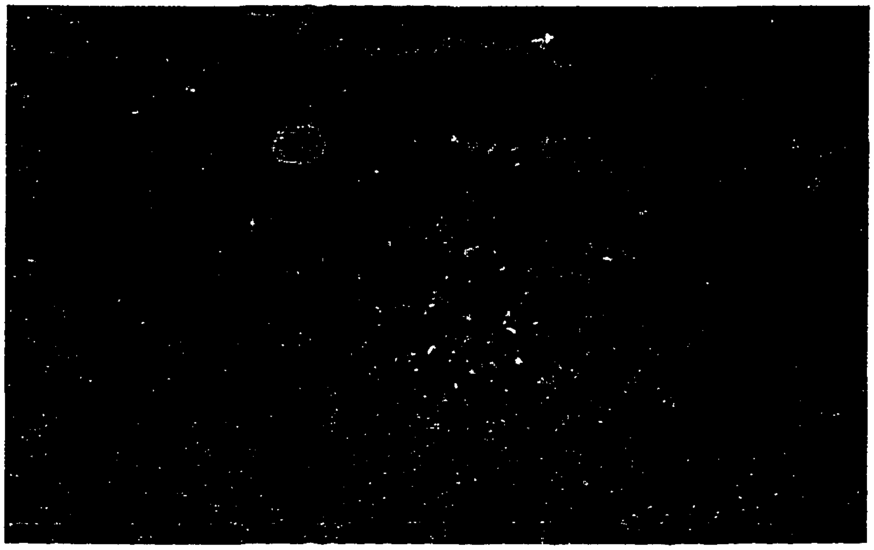

Fig. 5.17 Reconstruction of the original image from the output directly after Gabor wavelet transform.

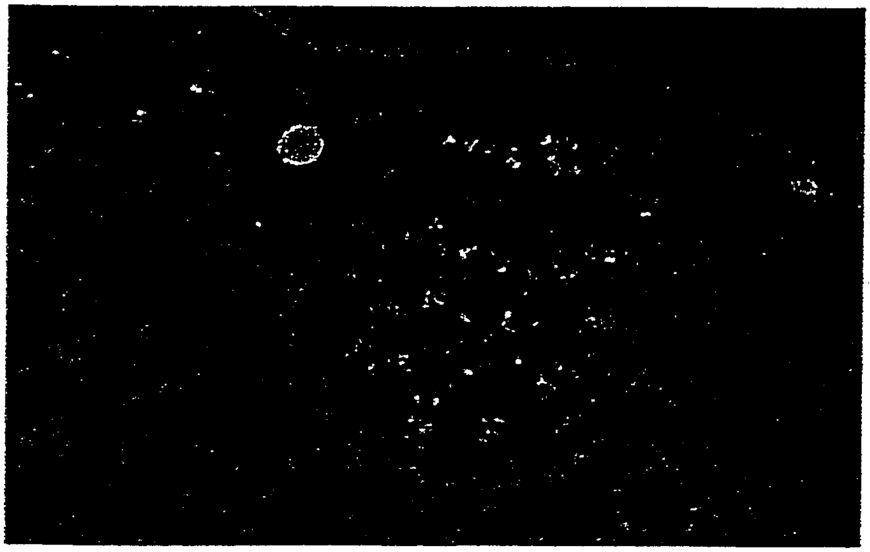

Fig. 5.18 Reconstruction of the original image from the data after the *tanh*() nonlinear transform.

Fig. 5.19 Reconstruction of the original image from the data after taking the absolute values.

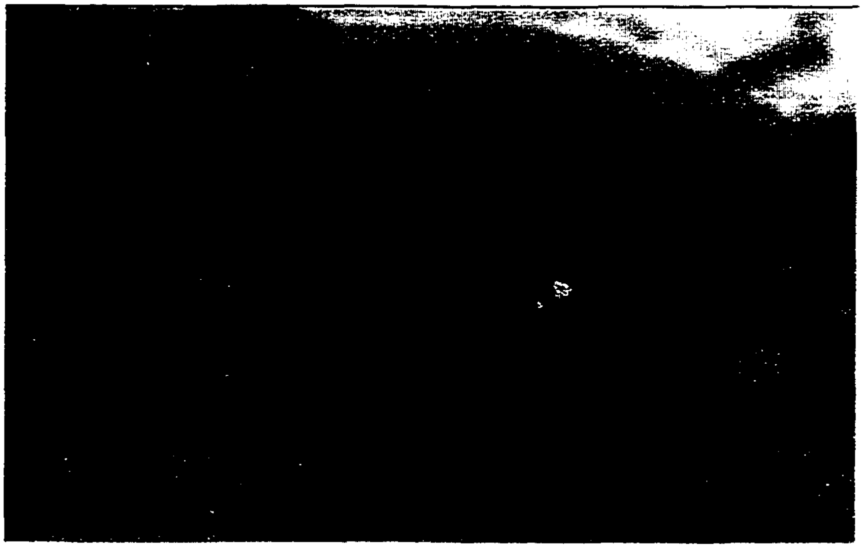

Fig. 5.20 Reconstruction of the original image from the texture feature after the Gaussian feature smoothing.

5.3 Application to Sequences of Brainstem Images

Results obtained in section 5.2 were based on well-studied sections by Dr. Jean Buettner from a rhesus monkey. In this section, we study the robustness of our methodology in analyzing a series of images of *Nissl* stained sections, which were scanned in our own laboratory using the Nikon Eclipse E400 microscope. We focus our efforts on identifying the abducens and the vestibular nuclei and compare the results with identified sections from an atlas of the rhesus monkey found at coordinates from P2.0 to P8.5 [28]. Abducens nucleus is located from P2.0 to 4.5 and the vestibular nuclei are located in more caudal sections from P5.5 to 8.5 (see Fig. 2.2A~B and Fig. 2.3A~B in chapter 2). While abducens nucleus is a singular and relatively more cohesive cell group, the vestibular nuclei consist of four distinctive parts, namely superior vestibular, lateral vestibular, medial vestibular and descending vestibular nuclei. The set of sample images we have analyzed were scanned from serial sections and were labeled as slide numbers from 180 to 245 in increments of 5 except the last one (Slides were identified and provided by Dr. Bernard Cohen). Two magnification levels were used in scanning the images. The 2× magnification level was used to capture a wide-angle view of the portion where abducens and vestibular nuclei were present, and the resultant image was used for segmentation purpose. The 10× magnification level was used to look into an individual cell group to illustrate the varying cell sizes and shapes. The abducens nucleus can be identified in slide numbers 180~215, and vestibular nuclei in slide numbers 205~245. In order to simplify the interpretation and comparison of the results, in all segmentation processing cases, we specified a fixed number of three clusters so that the cell groups, the fourth ventricle and neural tissues without cells were targeted for identification. For each slide in the sequence, we will show the original image, the segmentation result, a 10× magnification view of the interested cell group, and a plot of the averaged texture feature vectors of regions marked in the original and segmented images. Only the Gabor filter related features are shown in the plot, and we used a fixed number of Gabor filters of three frequency bands and four orientations. The order of the 12 features will be assigned as the three frequency bands with the center frequencies in the order of 3/64, 3/32 and 3/16 (cycles/pixel), while within each band there are four orientations at 0, 45, 90 and 135 degrees. In the following discussion about the plot, we will conveniently name the frequency bands as low, medium, and high frequency bands.

5.3.1 Identification of the Abducens Nucleus

Texture segmentation results on slides 180~215 are shown in figures 5.21~5.28. Slide 180 (Fig. 5.21) shows the first appearance of abducens nucleus (compare with Fig. 2.2A(A)). Instead of the usual circular cell aggregation, this formation is quite small (Fig. 5.21A and 5.21C, region #1) compared with other present nuclei such as the motor trigeminal nucleus (region #2) and the mesencephalic trigeminal nucleus (region #3). The 10× magnification level image (Fig. 5.21B) shows the presence of individual cells of the abducens nucleus. Fig. 5.21D shows the plot of the averaged texture feature vectors of the corresponding three marked regions. Region #1 has the least texture energy overall because it is the first appearance of the abducens nucleus so that the cell formation is small and sparse. Region #2 and #3 are close in terms of texture patterns. Compared with region #2, region #3 has a denser cell distribution, which is characterized by a higher energy in high frequency band and a lower energy at medium frequency band as the result of cells merging together in lower resolution.

Slide 185 (Fig. 5.22) shows that the abducens nucleus (region #1) starts to grow while the motor trigeminal nucleus (region #2) starts to shrink in size. The plot of the texture feature (Fig 5.22D) shows this trend as the pattern of region #1 and #2 move closer in pattern space, while region #3 remains relatively unchanged.

In slide 190 (Fig. 5.23), the abducens nucleus (region #1) almost grows to its full size. However, the cell density is still not comparable to that of the trigeminal nucleus (region #2), which is reflected in the overall texture energy.

Slide 195 (Fig. 5.24) shows the full-blown bilateral abducens nuclei (region #1 and #2) together with the less populated reticular parvocellular nucleus (region #3). The texture feature shows the close distance between the abducens nuclei on either side of the midline. The resemblance of the abducens nuclei on either side of the midline is also apparent in slide 200 (Fig. 5.25) as well.

The abducens nucleus starts to diminish gradually from slide 205 to slide 210 and almost disappears on slide 215, while the vestibular nuclei start to become apparent starting from slide 205. The 10× magnification image shows the decreasing population of the cell formation of the abducens nucleus (Fig. 5.26B, Fig. 5.27B and Fig. 5.28B), and the texture pattern clearly demonstrates this change. Fig. 5.26D shows that the abducens (region #1) in slide 205 has higher texture energy than the lateral vestibular nucleus (region #2). However, starting in slide 210, the lateral vestibular nucleus (region #2, Fig. 5.27D) shows higher texture energy than the abducens nucleus. The same is true in slide 215, as Fig. 5.28D shows that both the lateral (region #3) and the superior (region #4) vestibular nuclei have higher energy than the shrinking abducens nucleus.

5.3.2 Identification of the Vestibular Nuclei

Texture segmentation results on slides 205 to 245 are shown in figures 5.26~5.33. Compared to abducens nuclei, the vestibular nuclei are less clearly isolated (see the images from the brain atlas: Fig. 2.3A~B). Despite this, the texture-based algorithm has isolated some distinct cell groups. However, the actual labeling of these nuclei is tentative and strictly based on the texture properties. It will need further study and verification by anatomists using a wider range of anatomical techniques.

Slide 205 has the first showing of what are presumably the superior vestibular nucleus and the lateral vestibular nucleus (region #2 in Fig 5.26A), although texture energy showed in (region #2) is lower than that of the abducens nucleus. The lateral vestibular nucleus grows bigger in slide 210 together with the superior vestibular nucleus, and starts to have higher texture energy than the abducens nucleus (Fig 5.27). In slide 215, we begin to see medial vestibular nucleus (region #2, Fig 5.28A). Fig. 5.28D shows the differences of individual cell groups (region #1~#4 in the order of abducens, medial vestibular, lateral vestibular and superior vestibular nucleus). In particular, we can see that the superior and lateral vestibular nuclei (region #4 and #3) have a denser cell distribution than that of the medial vestibular nucleus (region #2). The same tendency can also be seen in slide 220 (Fig. 5.29), as the 10× image (Fig. 5.29B) shows some cell formation of medial vestibular nucleus. In slide 225, the medial vestibular nucleus grows significantly, but the averaged texture energy is still not as high as the superior and the lateral counterparts (Fig. 5.30D). Fig. 5.30B shows the 10× image of the lateral vestibular nucleus, which is manifested by its very big cell size and large spacing. As we discussed in section 5.1.1, bigger cells with large spacing tend to maintain high texture energy in lower resolutions. In Fig. 5.30D, the texture energy features of medial and superior vestibular nuclei (region #1 and #3) all have a large drop from the high frequency band to the medium frequency band. However, the lateral vestibular nucleus (region #2) maintains a similar energy level, and the energy drop from medium to low frequency band is smaller than the other two as well.

Descending vestibular nucleus shows up in Slide 230, with a texture energy pattern somewhat between that of the medial and lateral vestibular nuclei. The same cell size difference as described in Fig. 5.30D is also present in Fig. 5.31D.

The last two slides (slide 235 and 245) indicate some problems related to the inconsistency of the sample quality. Fig. 5.32 and 5.33 both show a practically non-existent medial vestibular nucleus (region #1), while in reality there should be the presence of the large cell group of medial vestibular nucleus. Under 10× magnification level, both Fig. 5.32B and Fig. 5.33B show cells in those regions, which are mostly grayed out. This may be related to the cut angle of the sample, which may defocus some parts of the slide relative to the other part. It may also be due to irregularities in the stain. Consequently, the low contrast of these cells contributed to the relatively poor segmentation result in these areas.

The Eclipse E400 microscope that we used in analyzing slides comes with the lenses for 1×, 2×, 10×, 20×, and 40× magnification levels. Although 10× and better magnification levels can provide more distinctive and detailed images, they can only capture a very small portion of a particular nucleus. Therefore, in all our results of analyzing the sequential slides of abducens and vestibular nuclei, we only used images taken with the 2× magnification level because they had the appropriate wide field of vision to capture nucleus in its entirety. However, there is an inherent loss of resolution when grabbing images into the computer. While the video camera has a horizontal resolution of 2000 lines, the maximum pixel resolution of the frame grabber is only 640×480. This kind of problems could be generally solved by using a higher resolution frame-grabber. We tried using an alternative approach. We took multiple 10× image portions and used image stitching to create a large image for processing. Fig. 5.34 is such an example taken from slide #195 capturing the left abducens nucleus. The image was created by stitching together 9 images (3×3 array) of 10× magnification, followed by picking up the region of interest by cropping. Since the cell spacing is relatively sparse at this resolution level, the image was then scaled down by 2 to make it essentially a 5× magnification image. Compared with the 2× magnification image shown in Fig. 5.24, this higher resolution image shows more details of the shape and formation of cells compared, which makes subdivision inside the abducens nucleus easier. The first segmentation and the second segmentation are shown in Fig. 5.35 and Fig. 5.36 respectively. The first segmentation recognized the abducens nucleus. It also distinguished among the two areas of the surrounding neural tissues which seemed to have distinct orientational difference. The second segmentation sub-divided the abducens nucleus into four sub-regions based on the texture difference. It appeared that there are difference between the dorsal portion and the ventral portion and differences inside the dorsal portion.

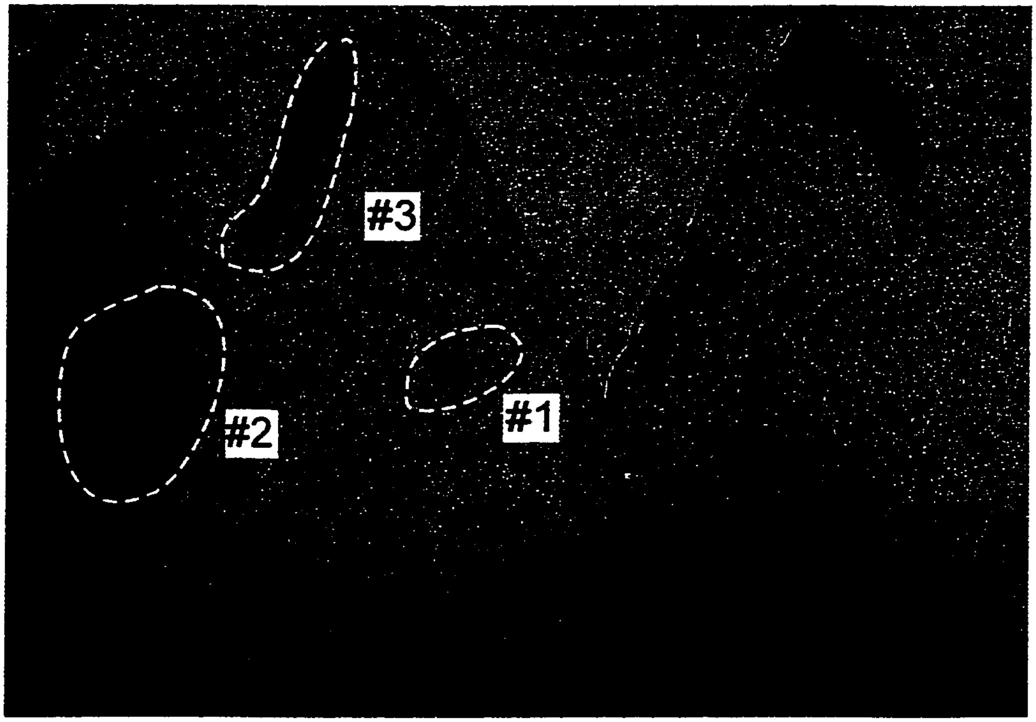

Fig. 5.21A The original image of slide #180

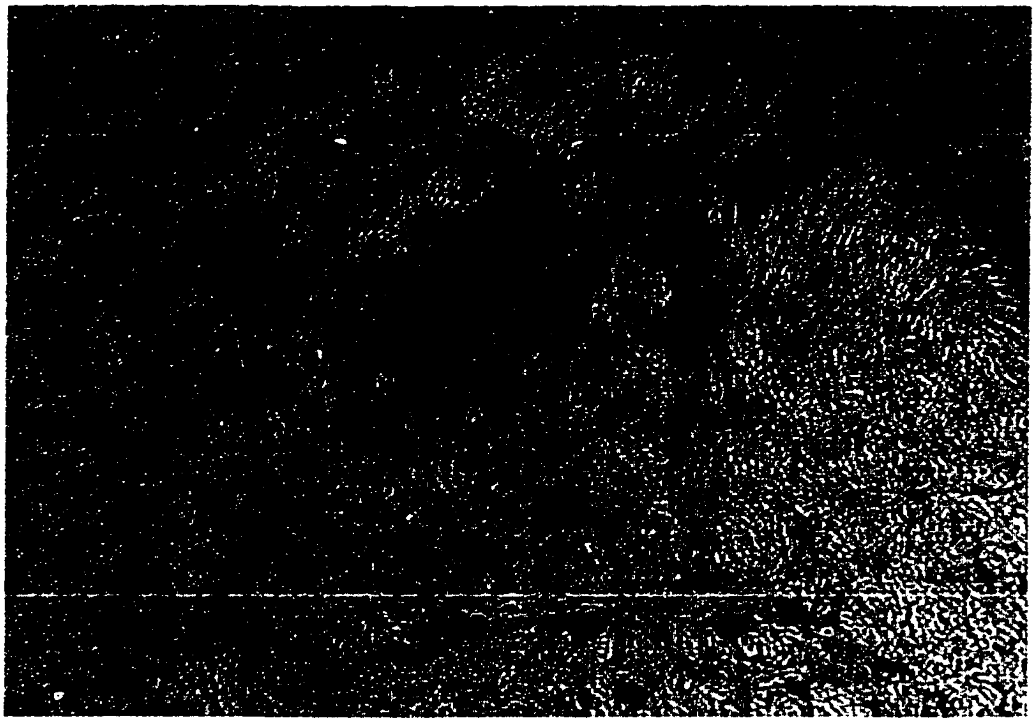

Fig. 5.21B The 10x magnification image of region #1 in slide #180

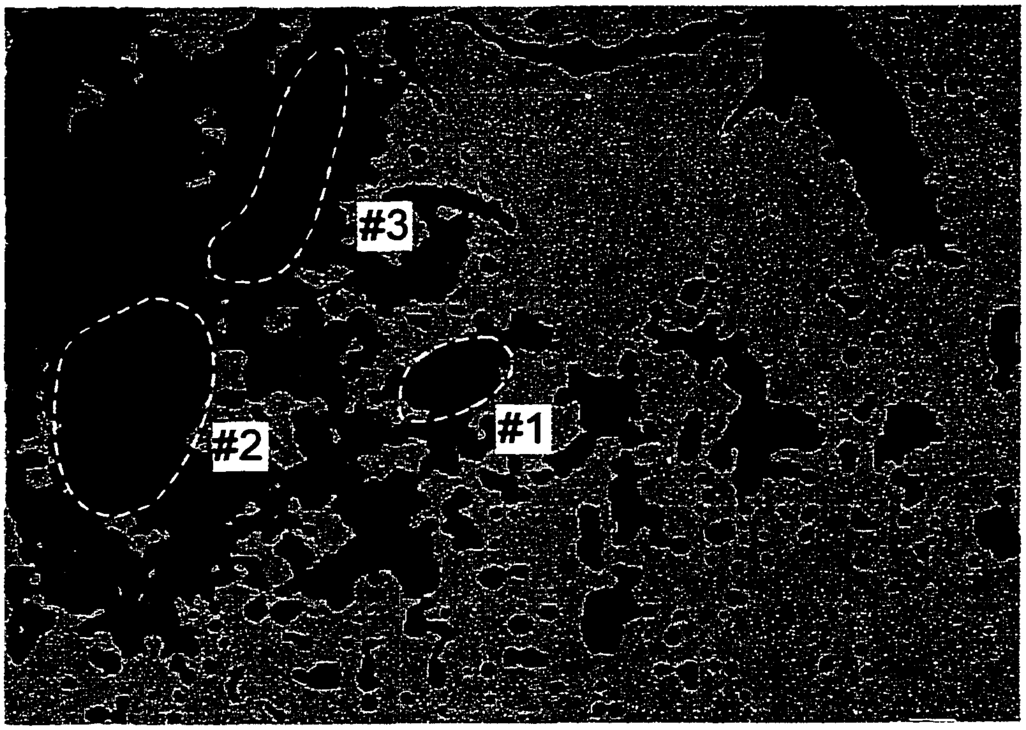

Fig. 5.21C The segmentation image of slide #180

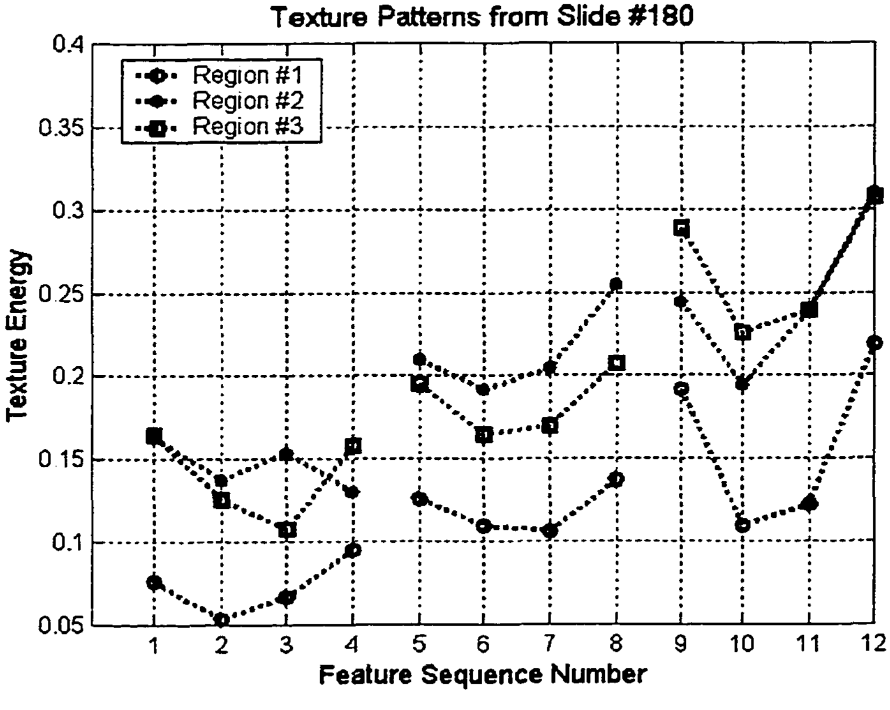

Fig. 5.21D The plot of the texture feature of region #1~3 in slide #180

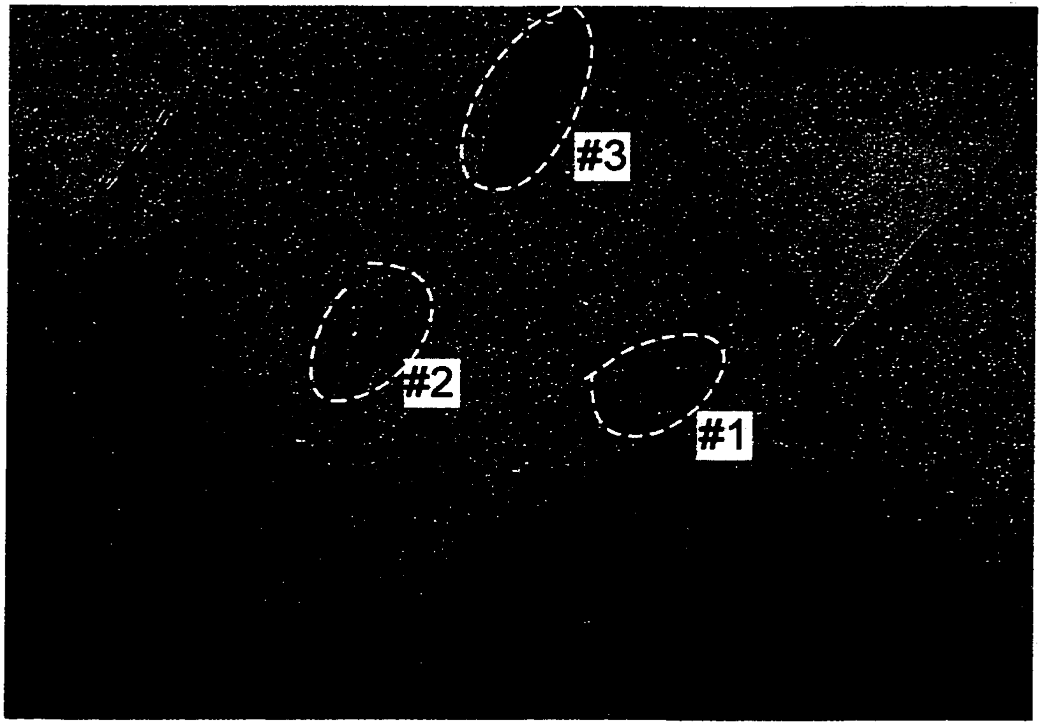

Fig. 5.22A The original image of slide #185

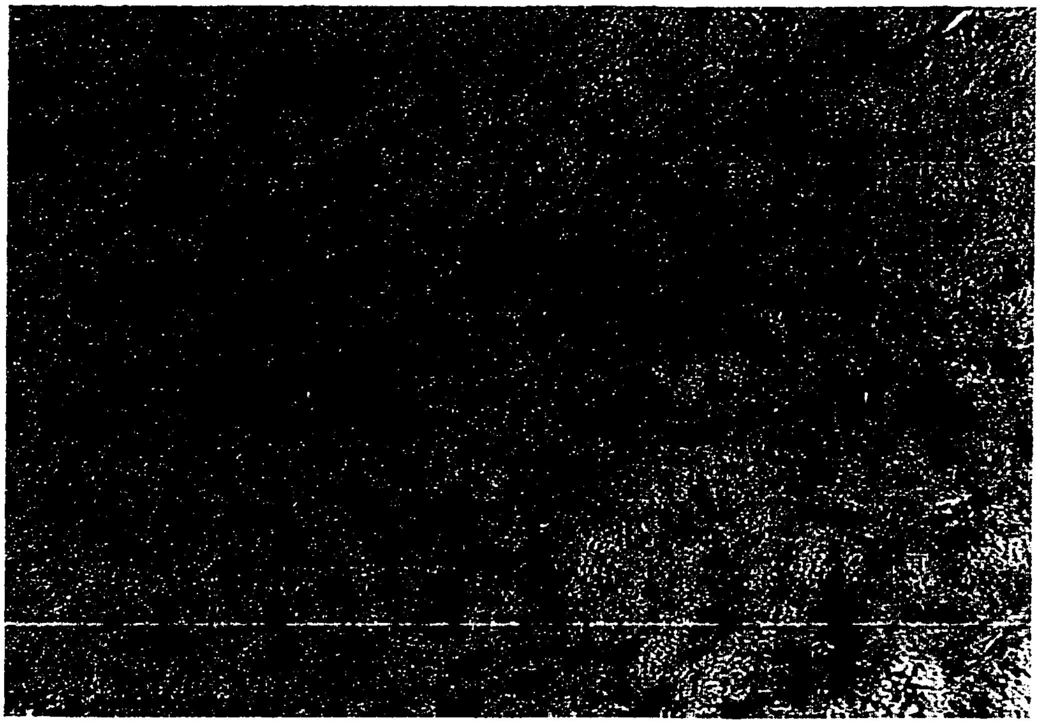

Fig. 5.22B The 10x magnification image of region #1 in slide #185

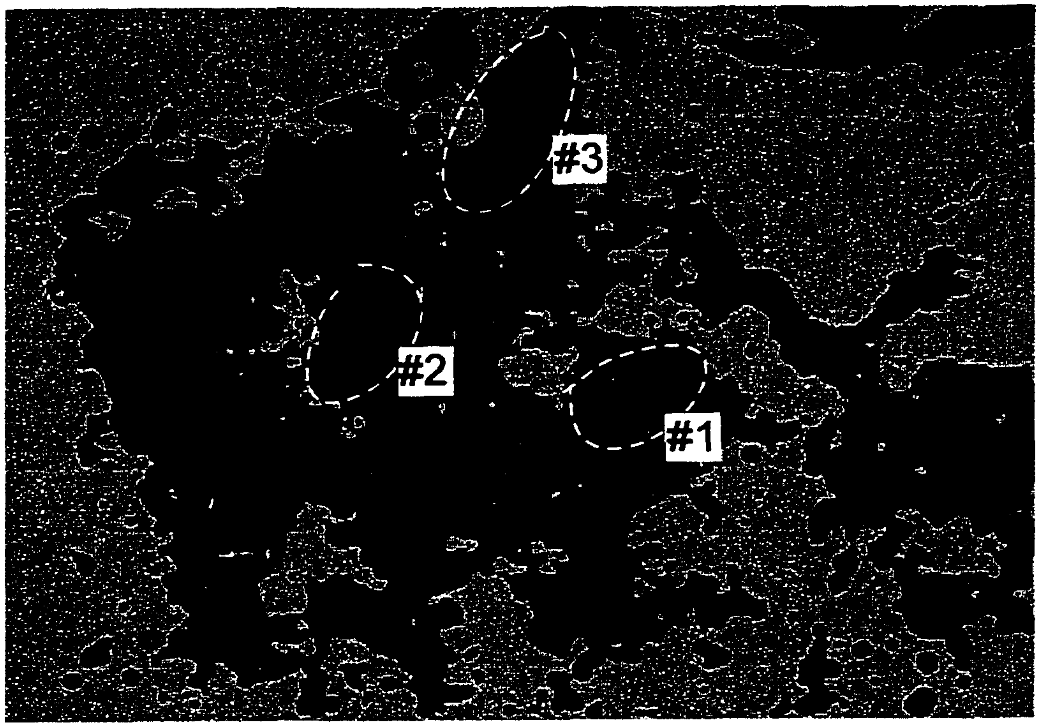

Fig. 5.22C The segmentation image of slide #185

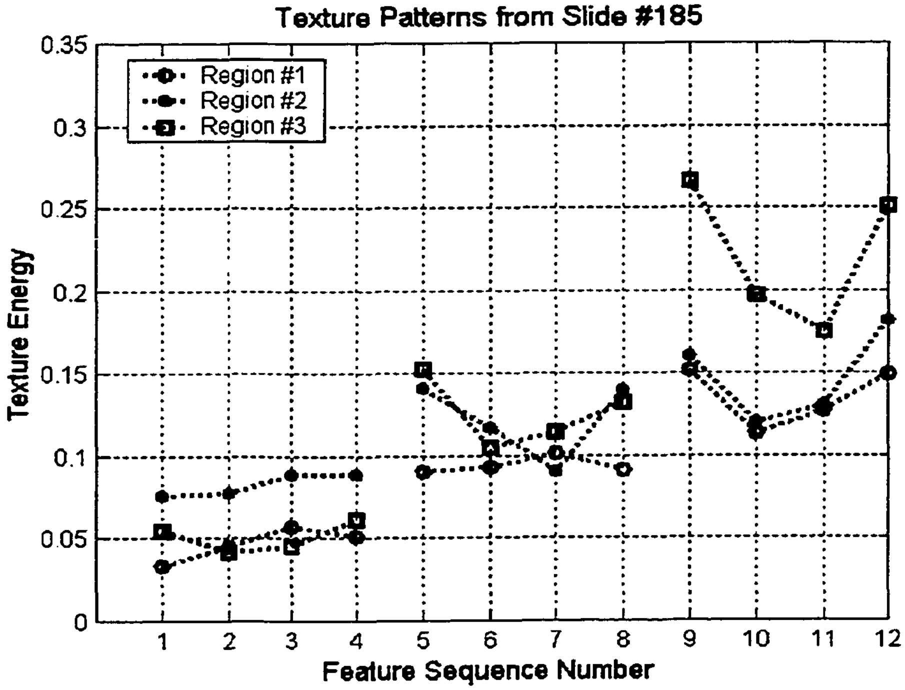

Fig. 5.22D The plot of the texture feature of region #1~3 in slide #185

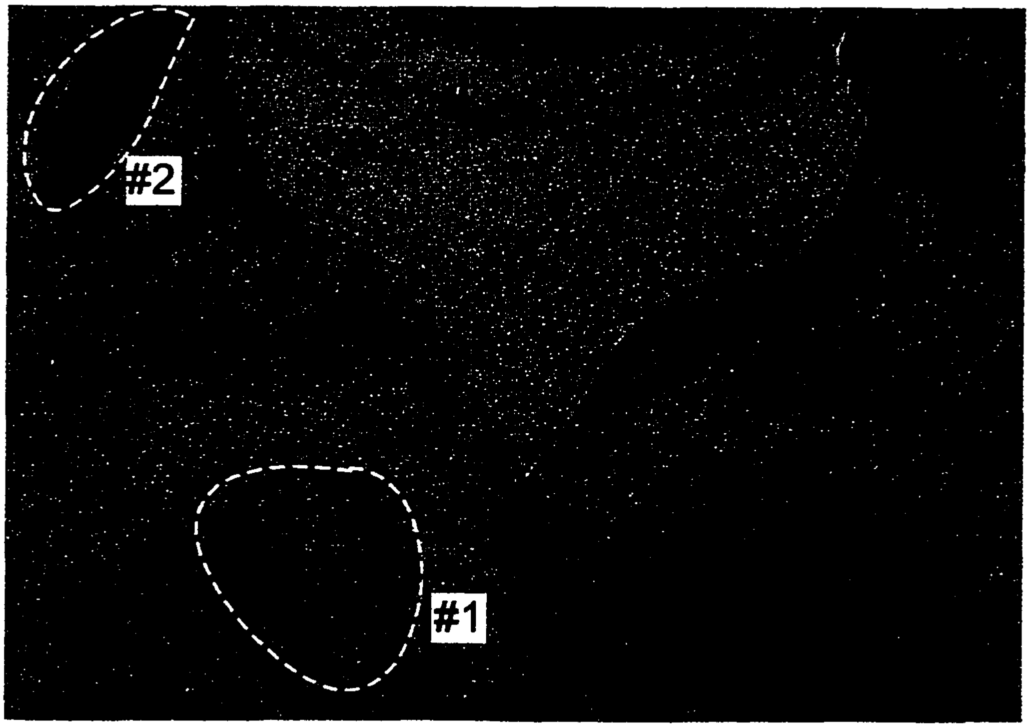

Fig. 5.23A The original image of slide #190

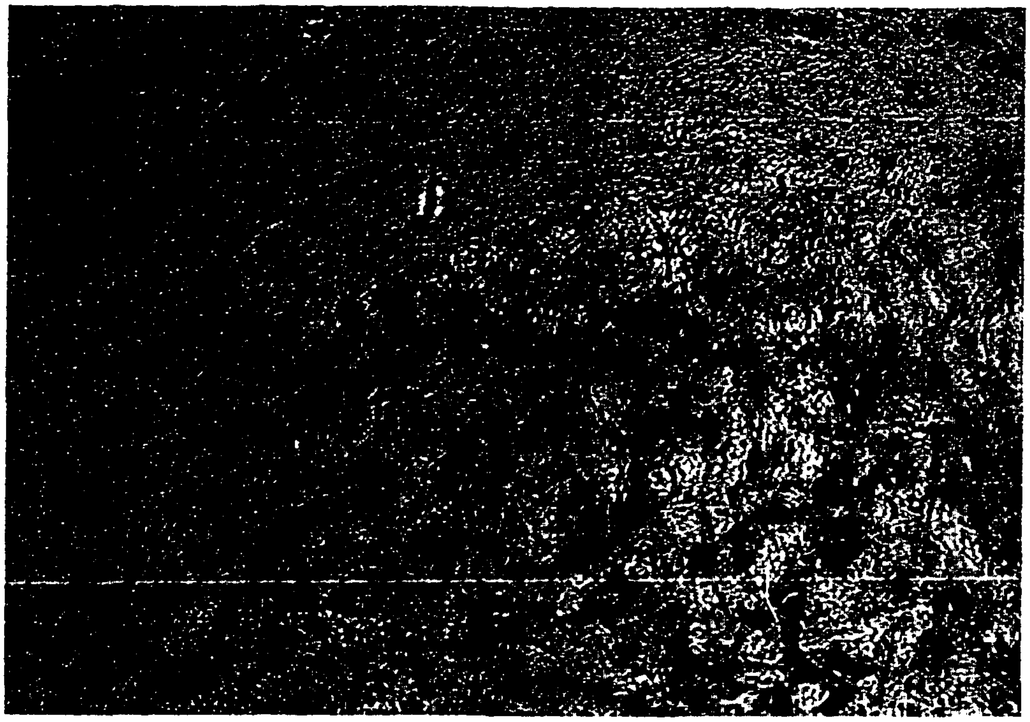

Fig. 5.23B The 10x magnification image of region #1 in slide #190

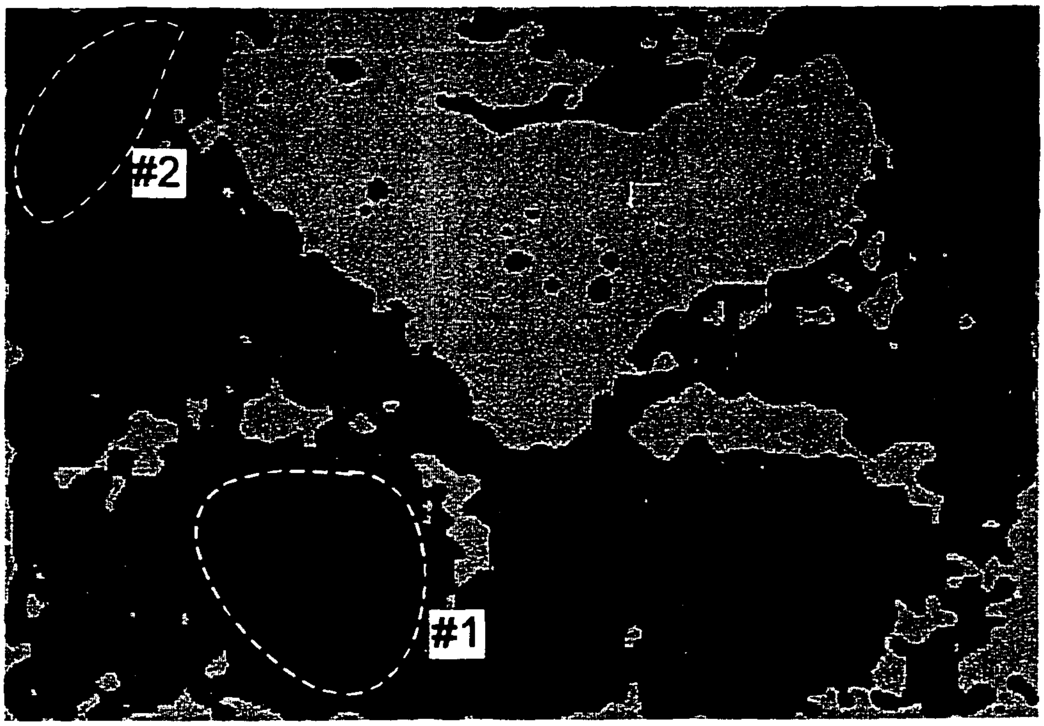

Fig. 5.23C The segmentation image of slide #190

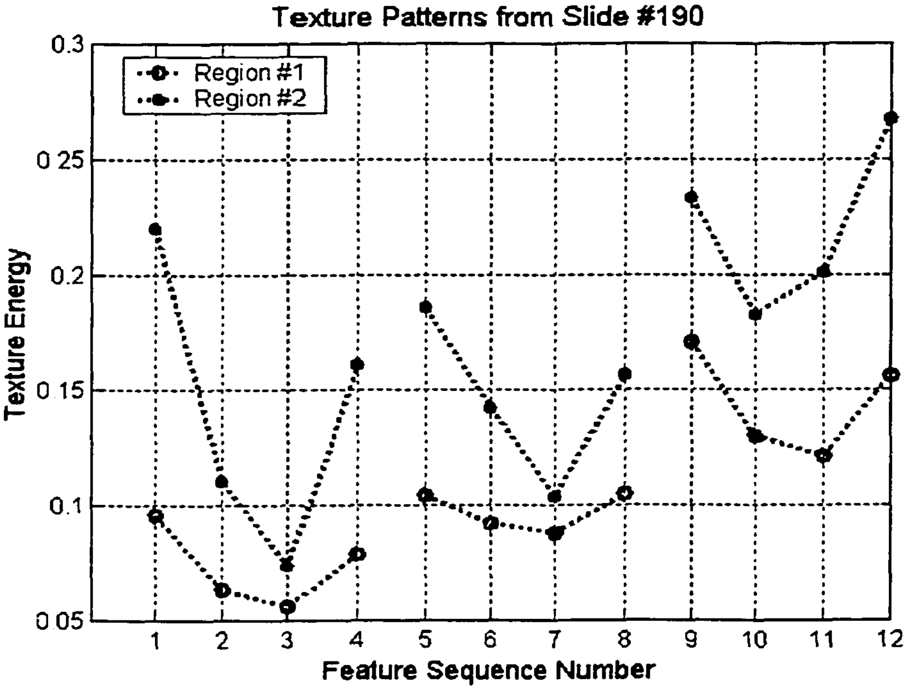

Fig. 5.23D The plot of the texture feature of region #1~2

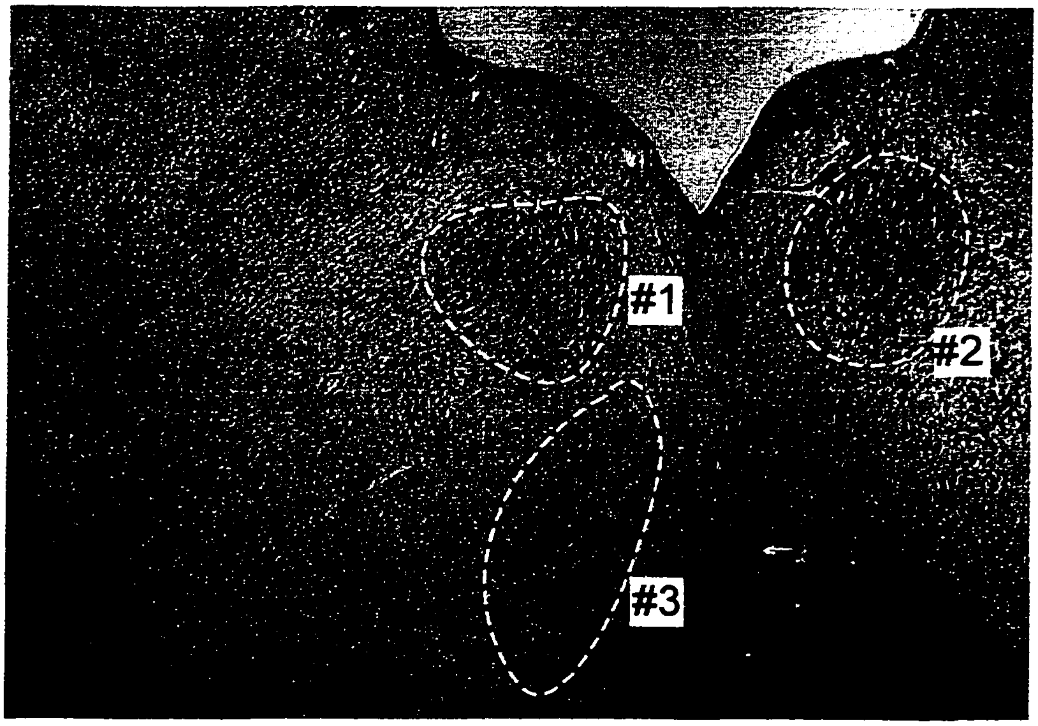

Fig. 5.24A The original image of slide #195

Fig. 5.24B The 10x magnification image of region #1 in slide #195

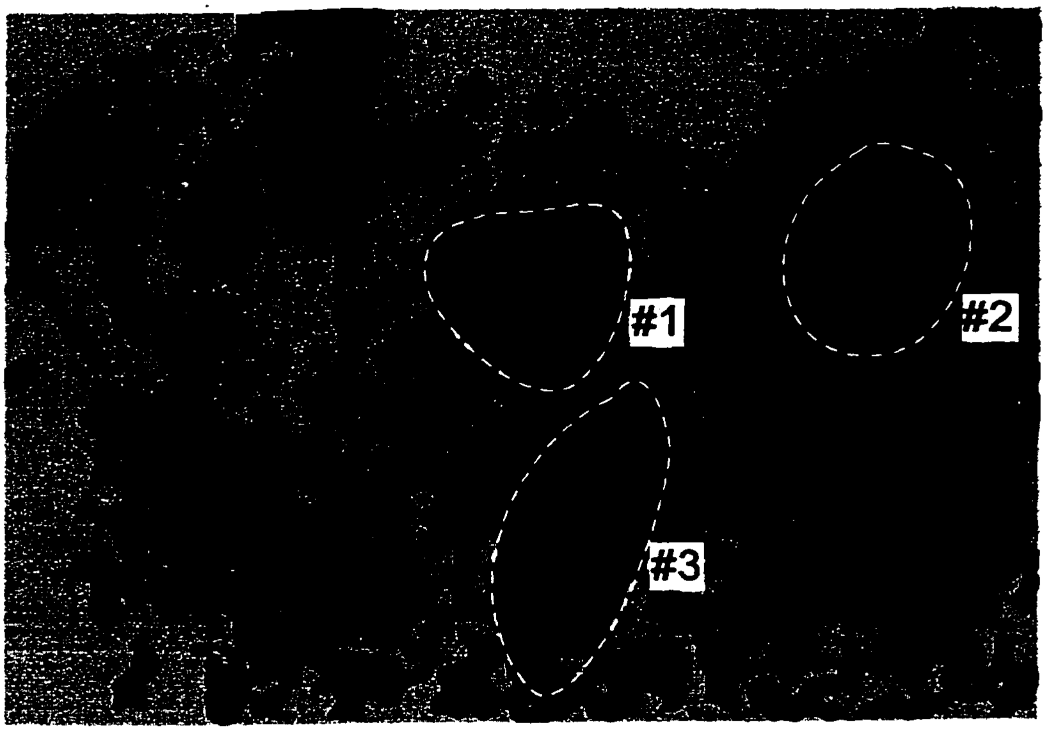

Fig. 5.24C The segmentation image of slide #195

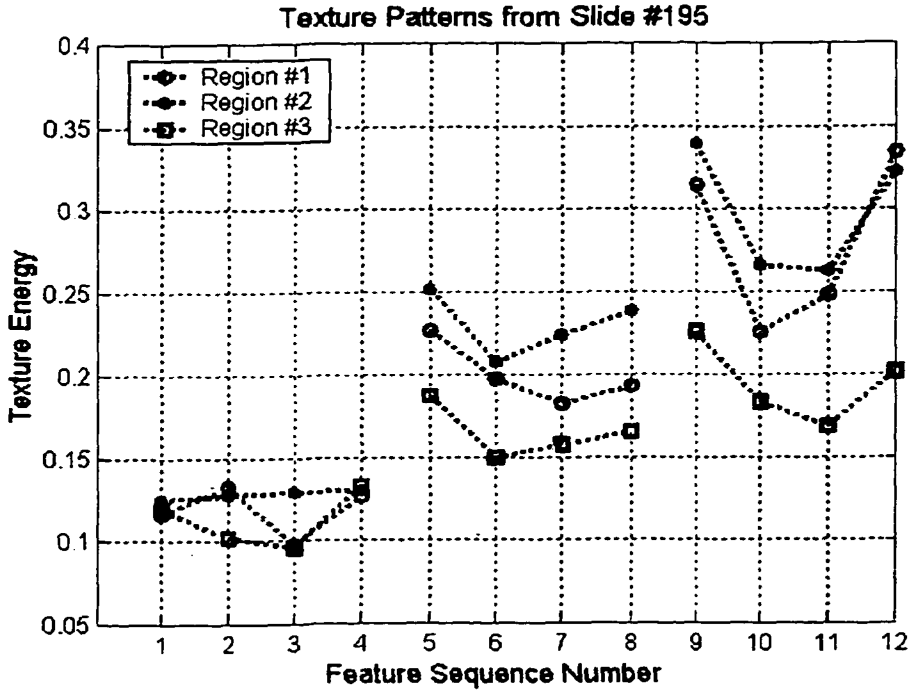

Fig. 5.24D The plot of the texture feature of region #1~3 in slide #195

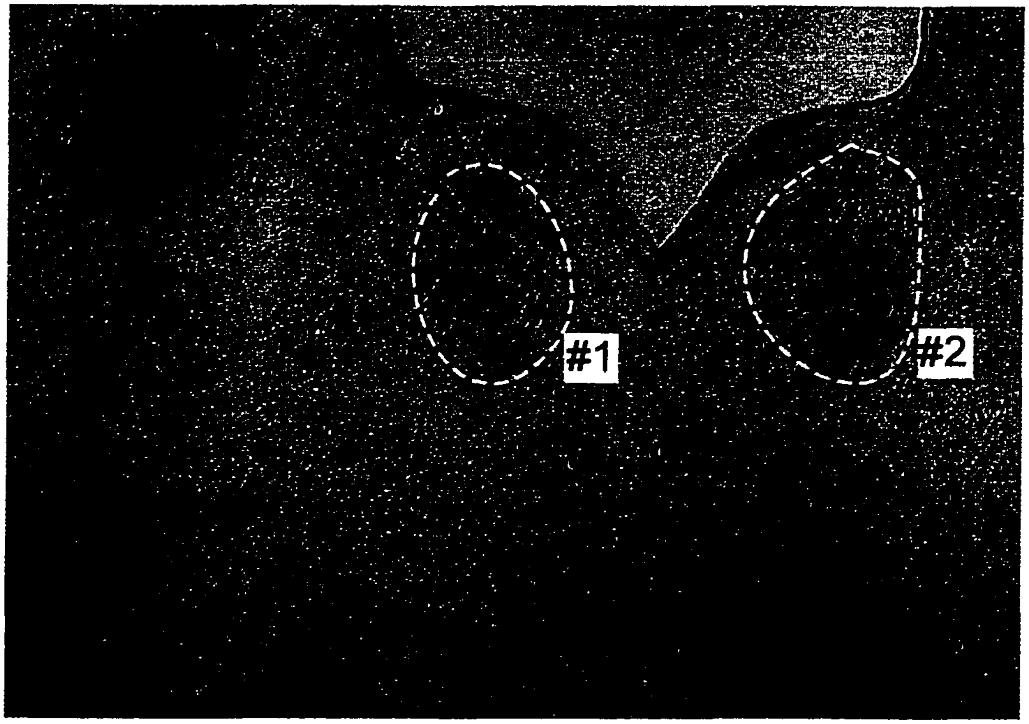

Fig. 5.25A The original image of slide #200

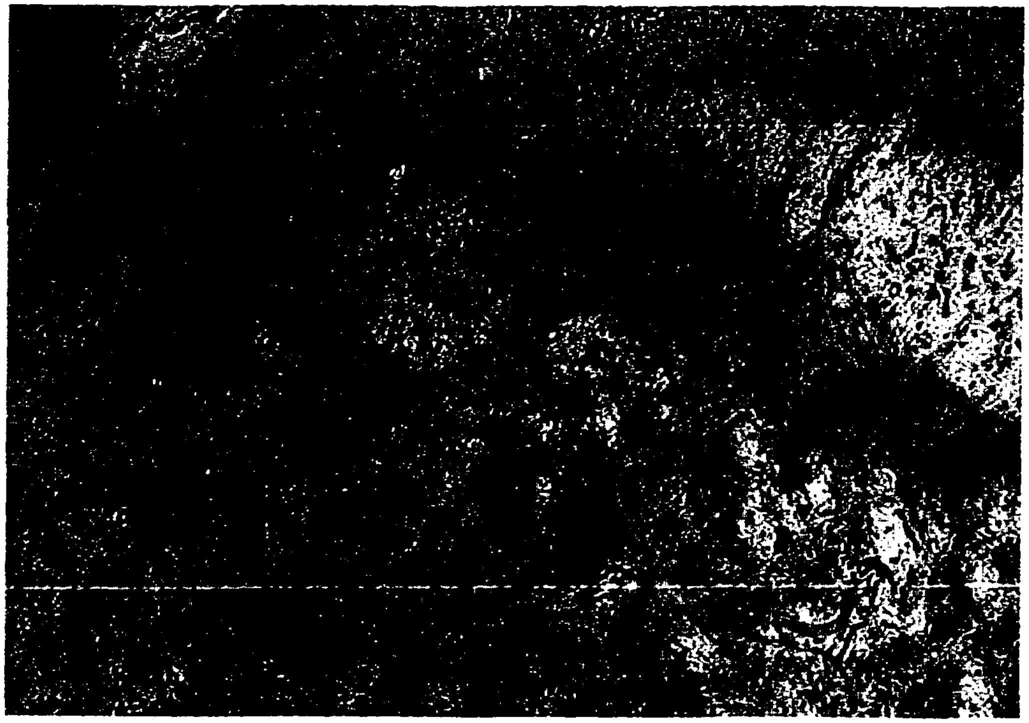

Fig. 5.25B The 10x magnification image of region #1 in slide #200

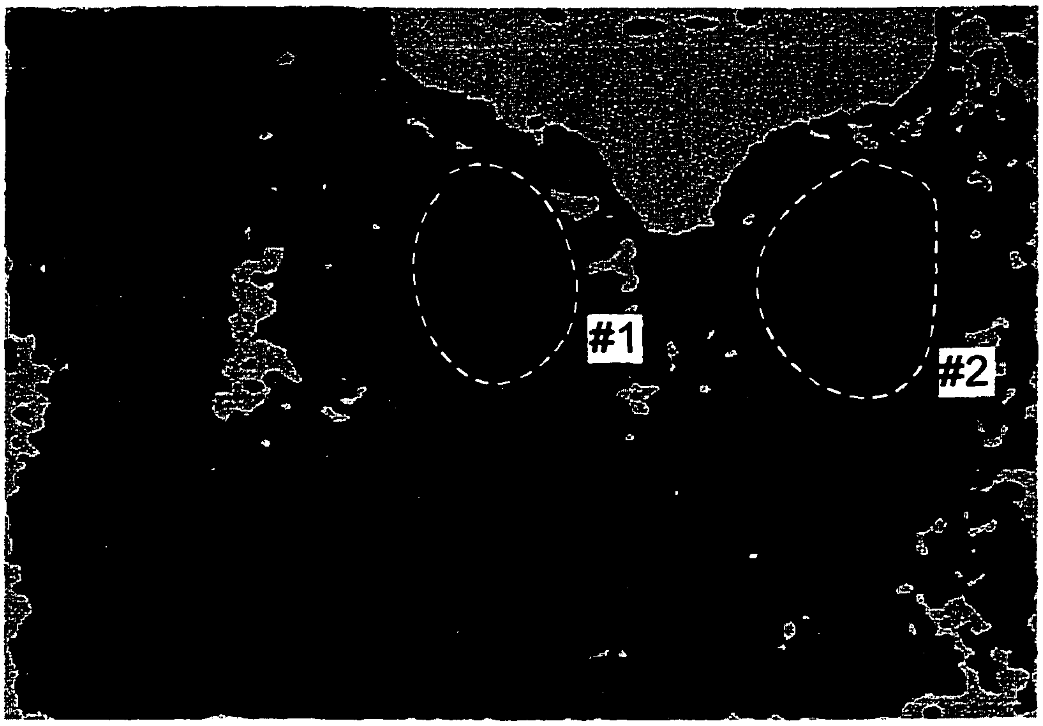

Fig. 5.25C The segmentation image of slide #200

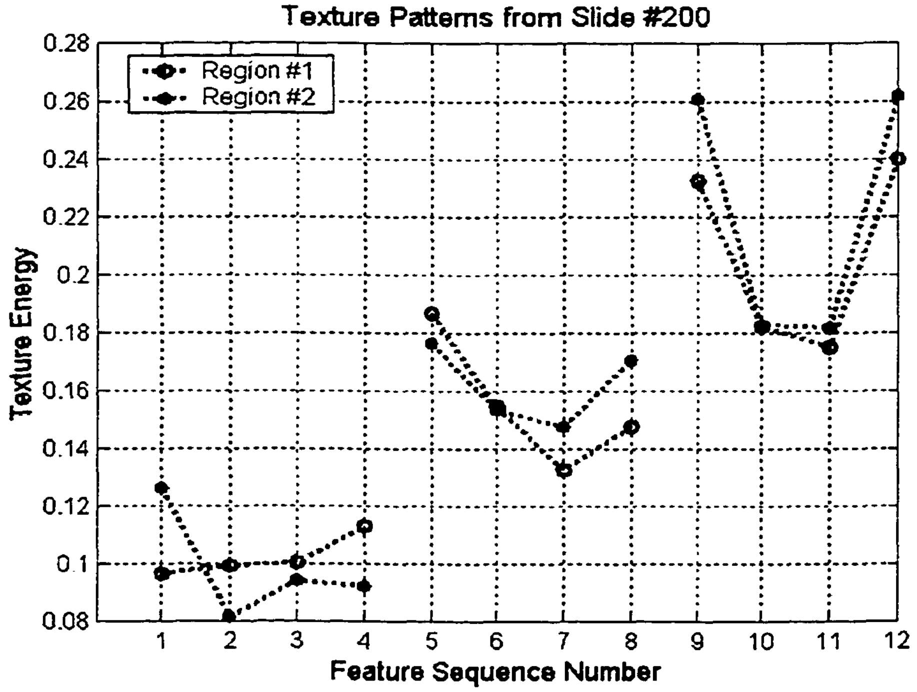

Fig. 5.25D The plot of the texture feature of region #1~2 in slide #200

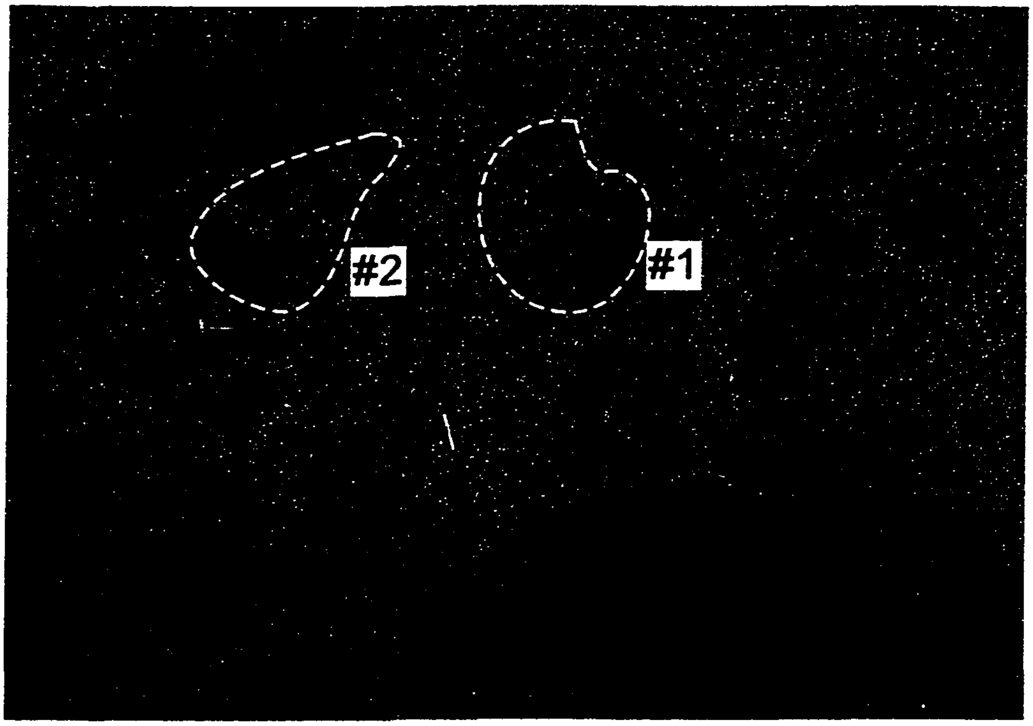

Fig. 5.26A The original image of slide #205

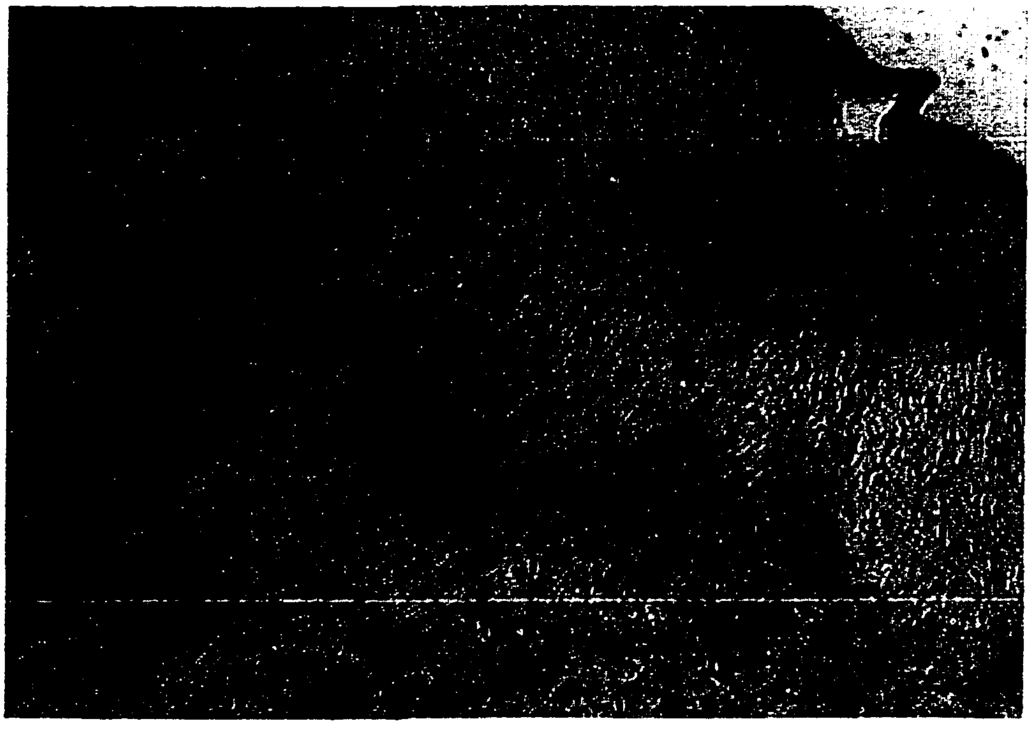

Fig. 5.26B The 10x magnification image of region #1 in slide #205

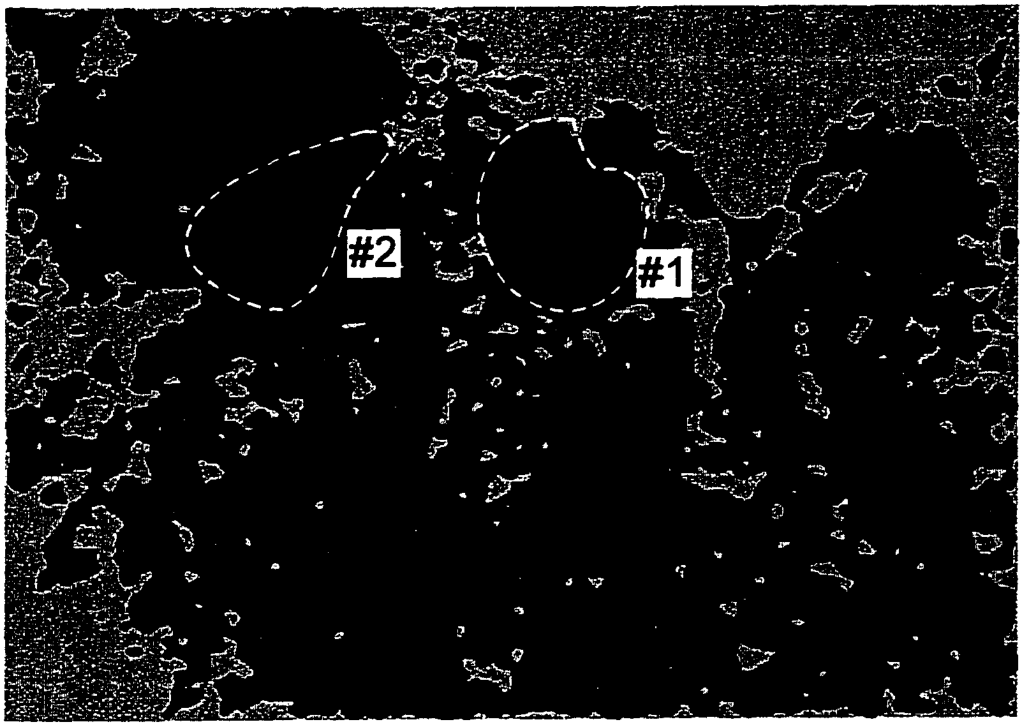

Fig. 5.26C The segmentation image of slide #205

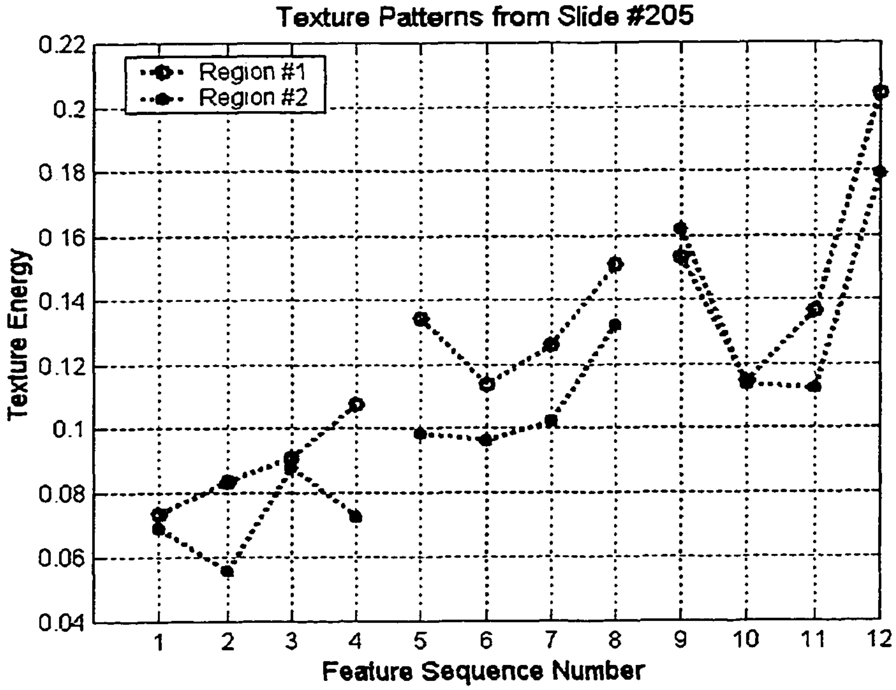

Fig. 5.26D The plot of the texture feature of region #1~2 in slide #205

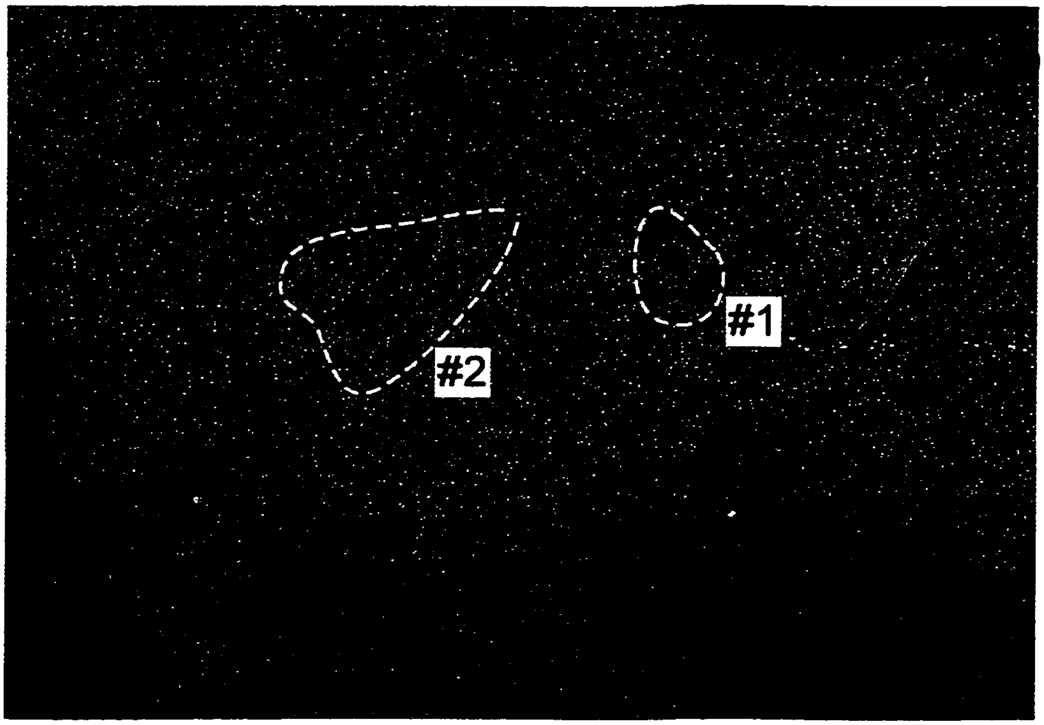

Fig. 5.27A The original image of slide #210

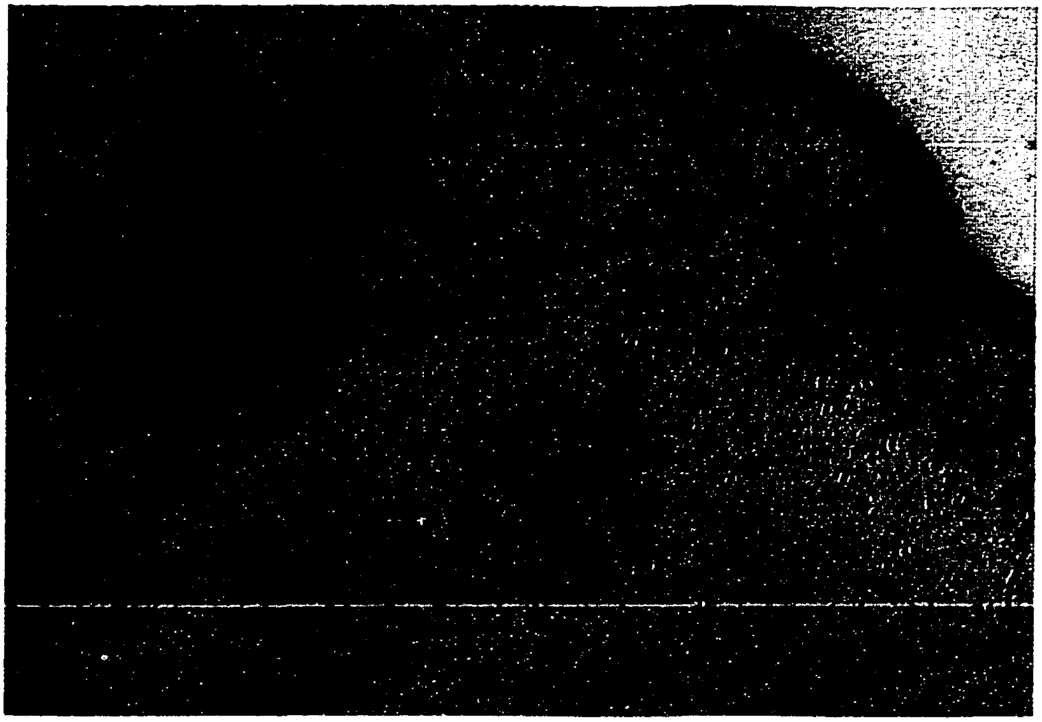

Fig. 5.27B The 10x magnification image of region #1 in slide #210

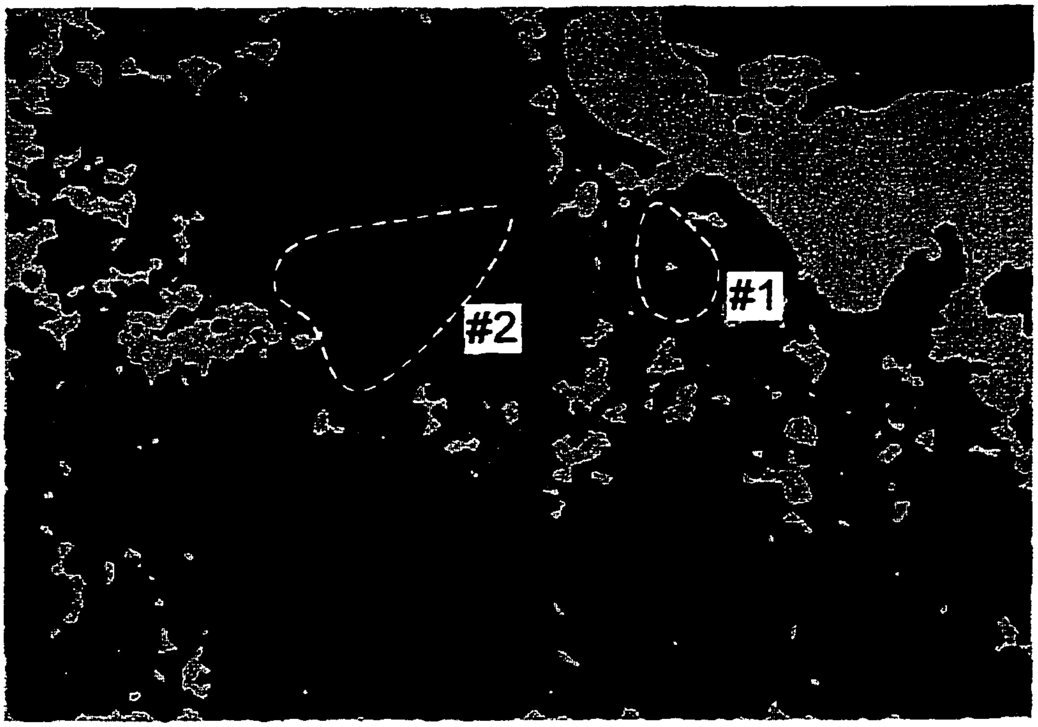

Fig. 5.27C The segmentation image of slide #210

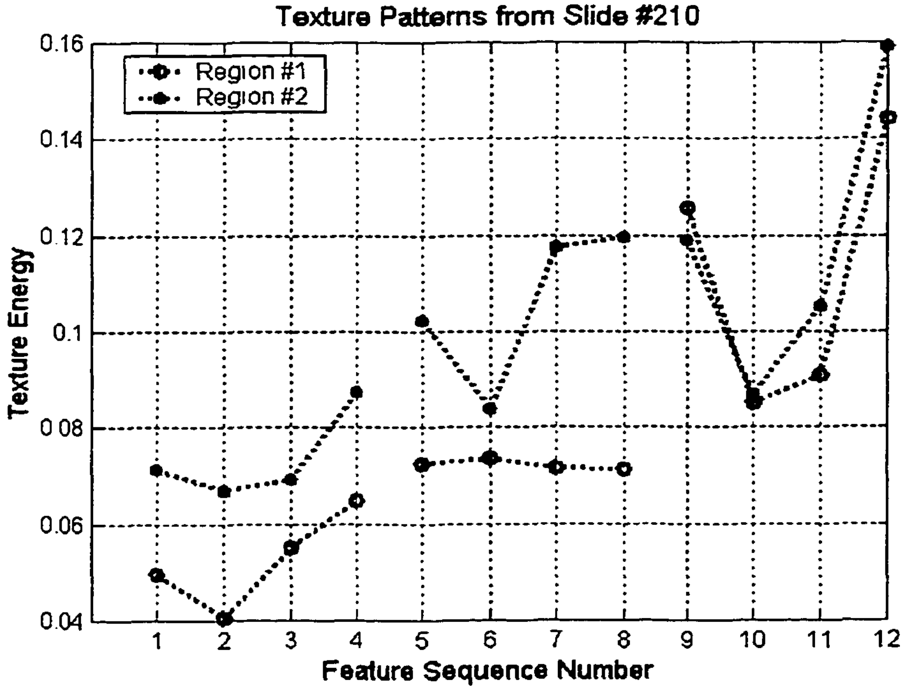

Fig. 5.27D The plot of the texture feature of region #1~2 in slide #210

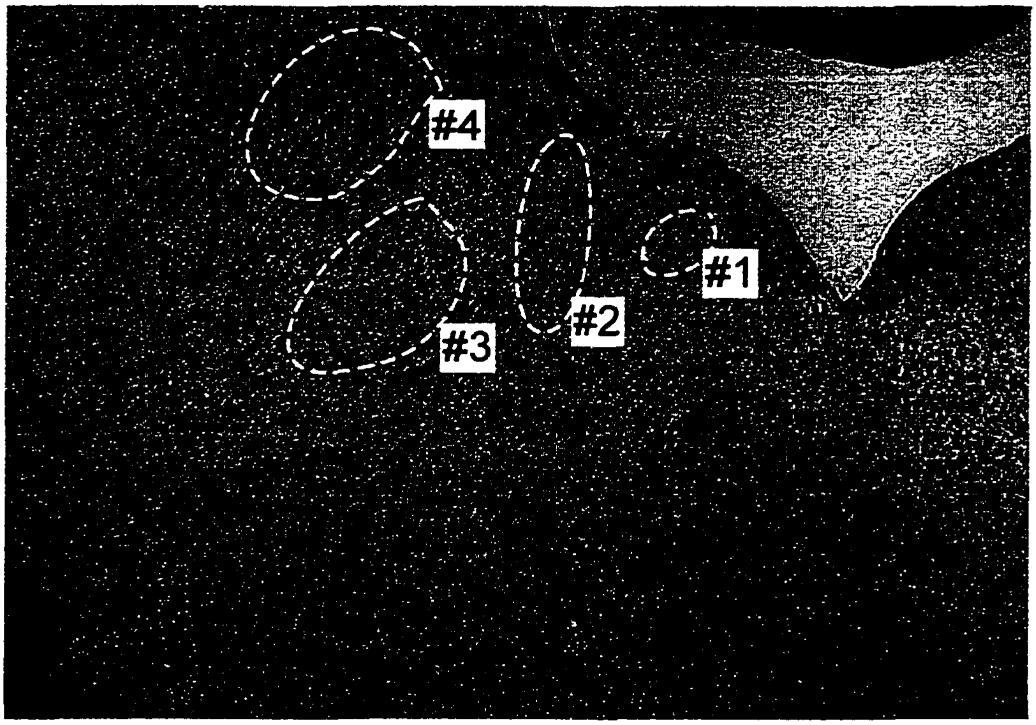

Fig. 5.28A The original image of slide #215

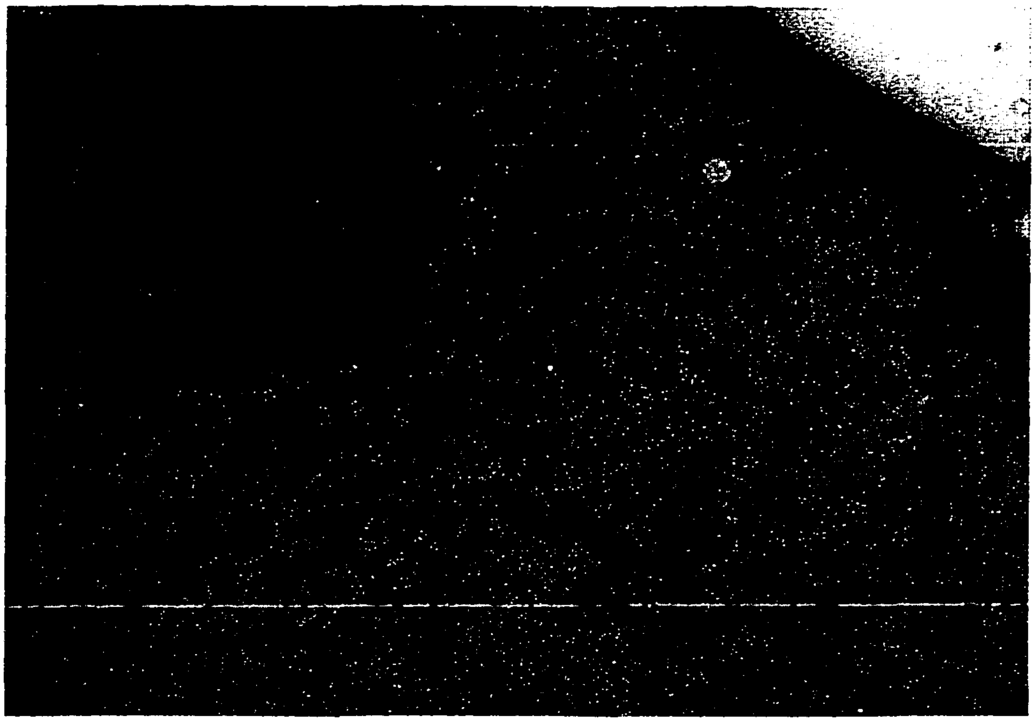

Fig. 5.28B The 10x magnification image of part of region #2 in slide #215

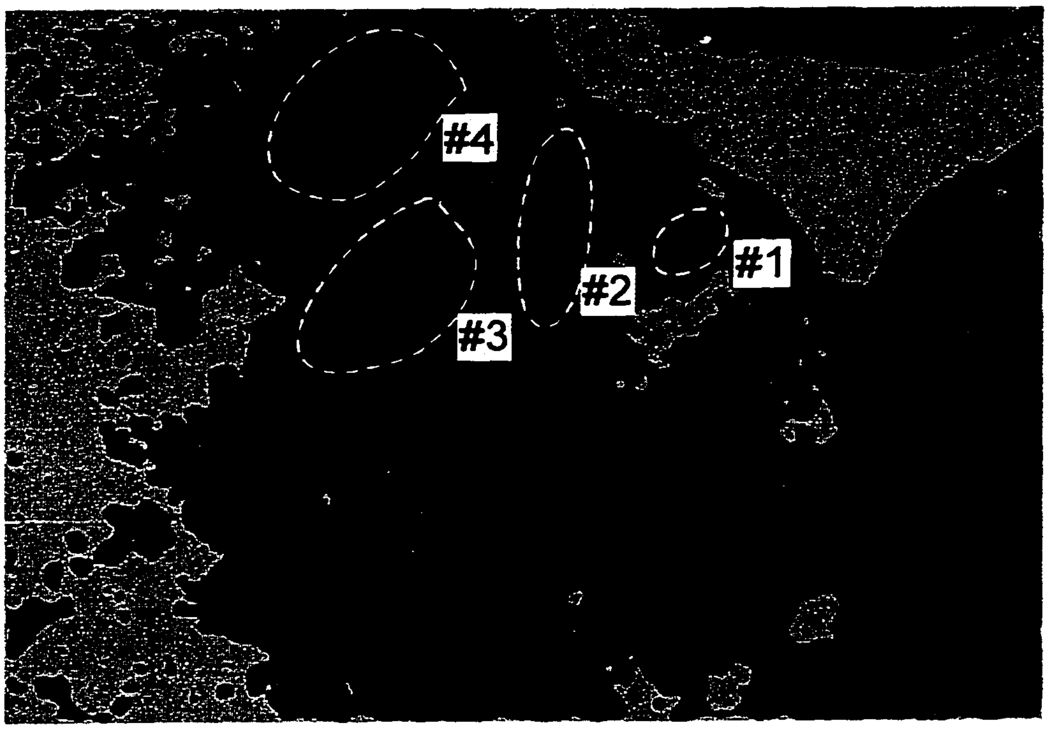

Fig. 5.28C The segmentation image of slide #215

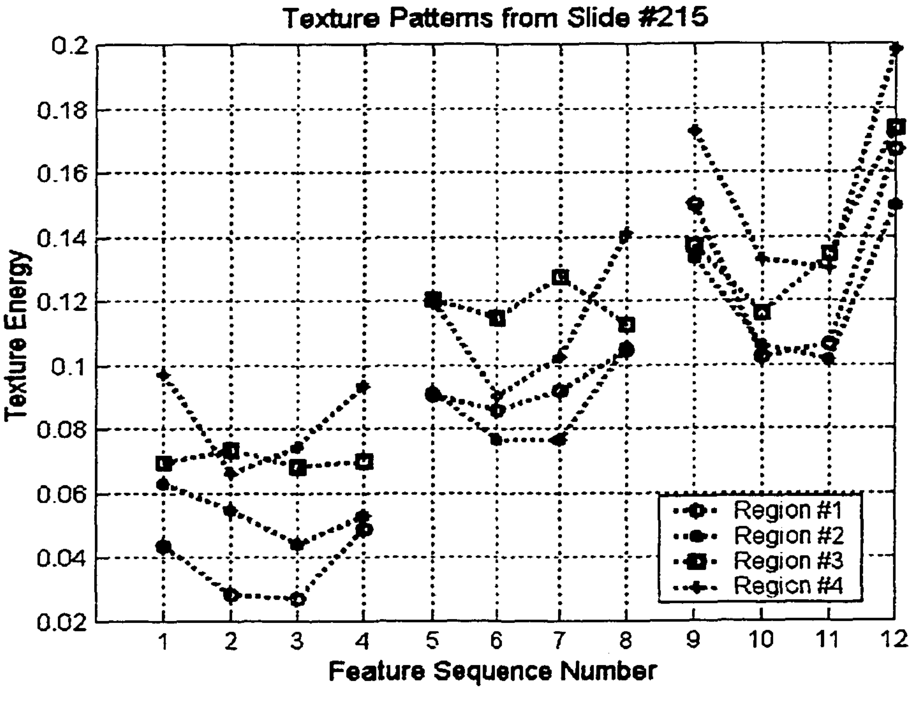

Fig. 5.28D The plot of the texture feature of region #1~4 in slide #215

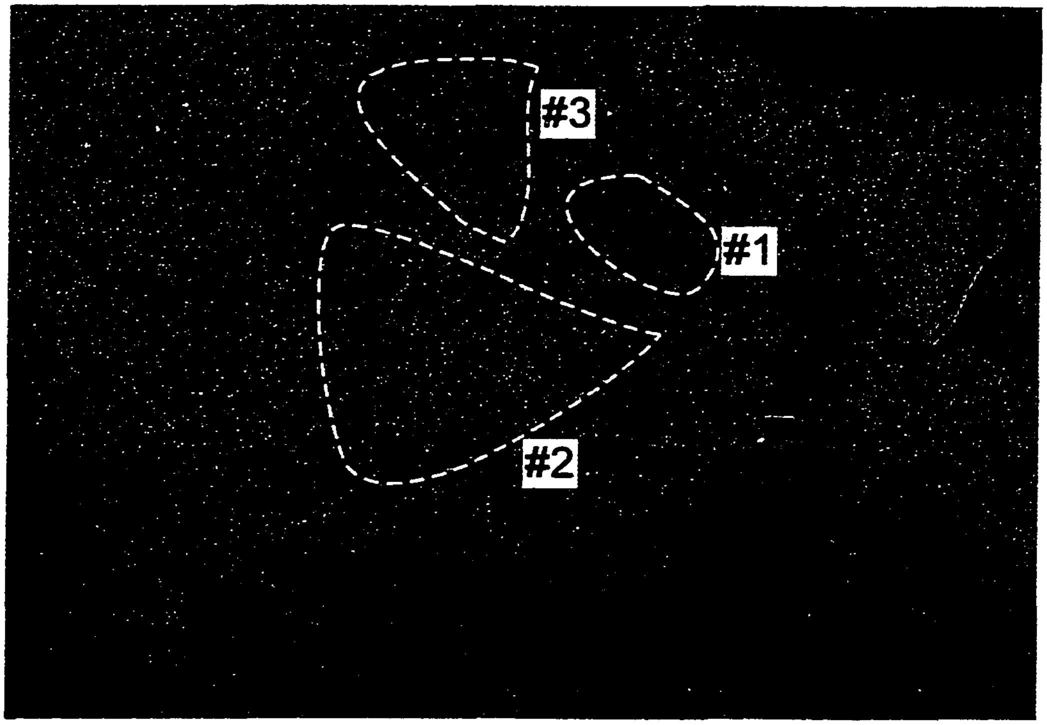

Fig. 5.29A The original image of slide #220

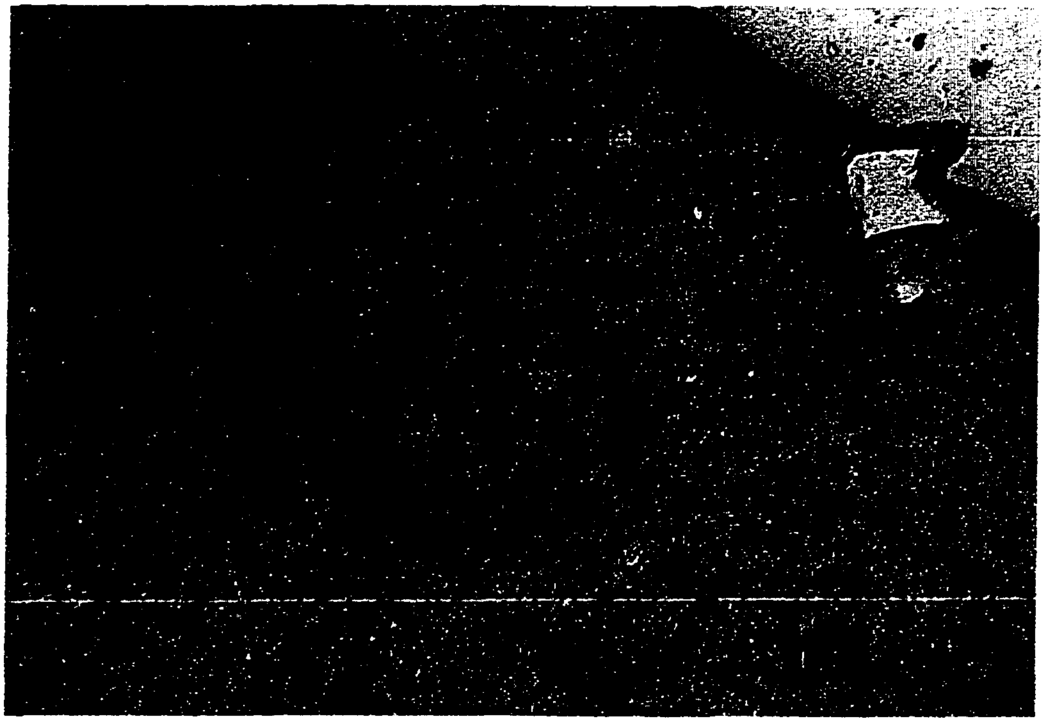

Fig. 5.29B The 10x magnification image of region #1 in slide #220

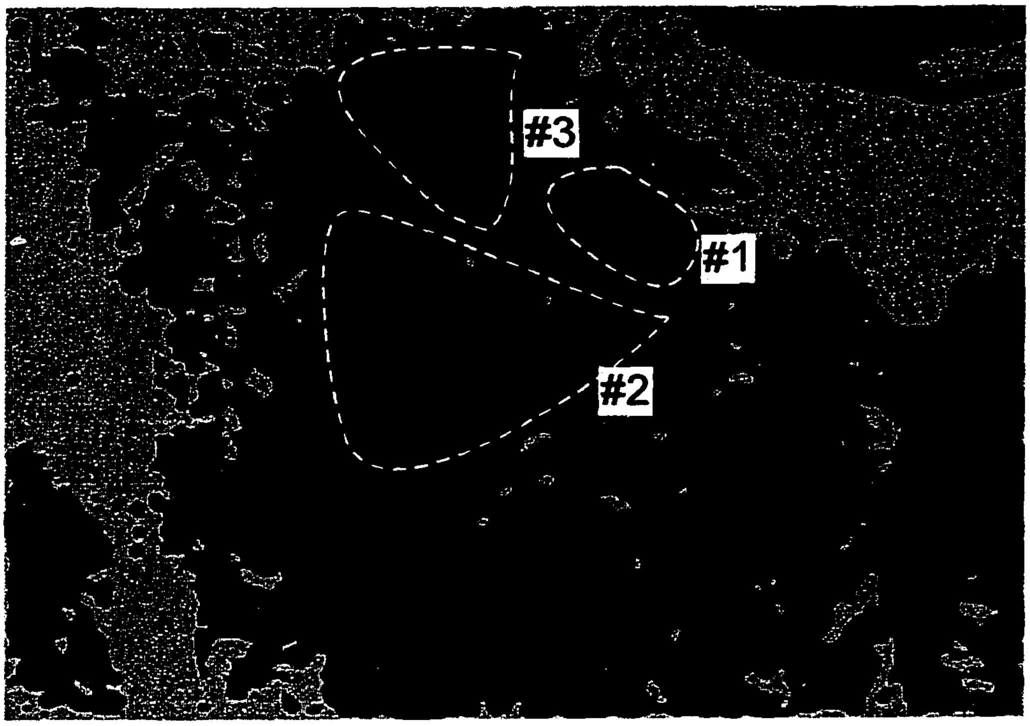

Fig. 5.29C The segmentation image of slide #220

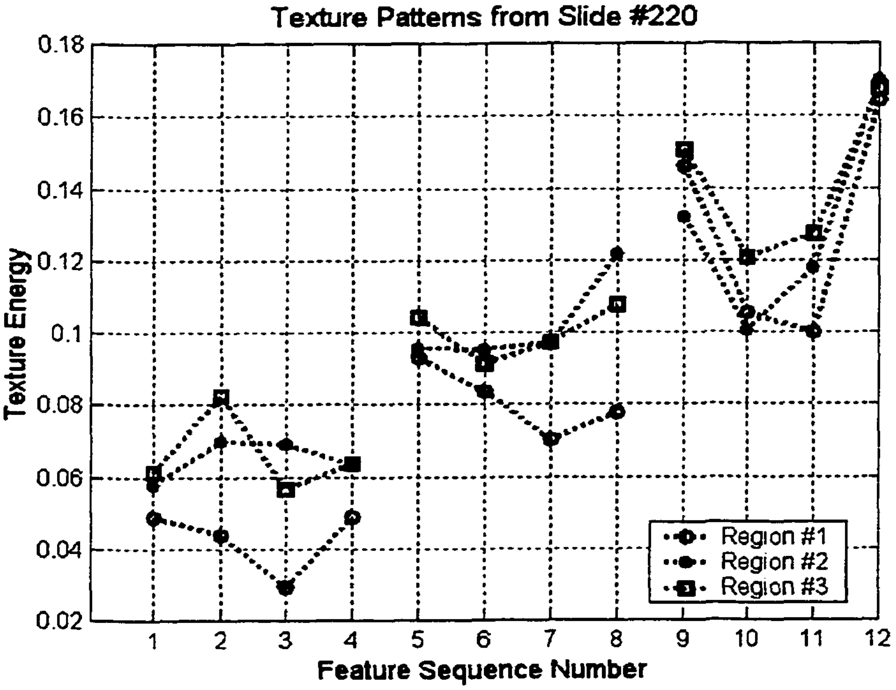

Fig. 5.29D The plot of the texture feature of region #1~3 in slide #220

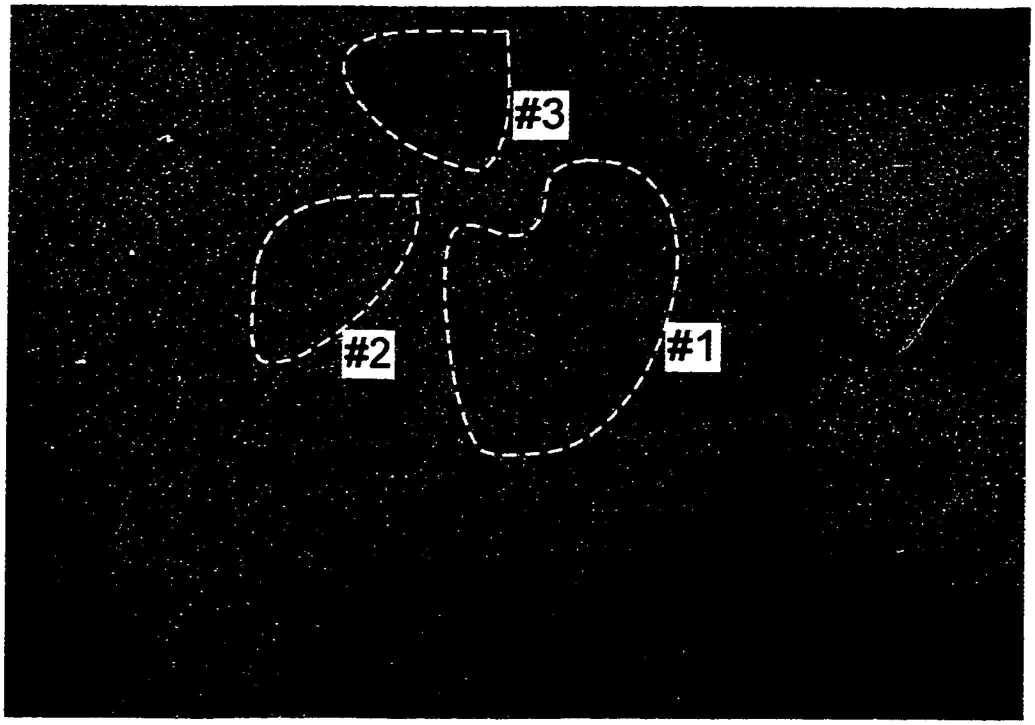

Fig. 5.30A The original image of slide #225

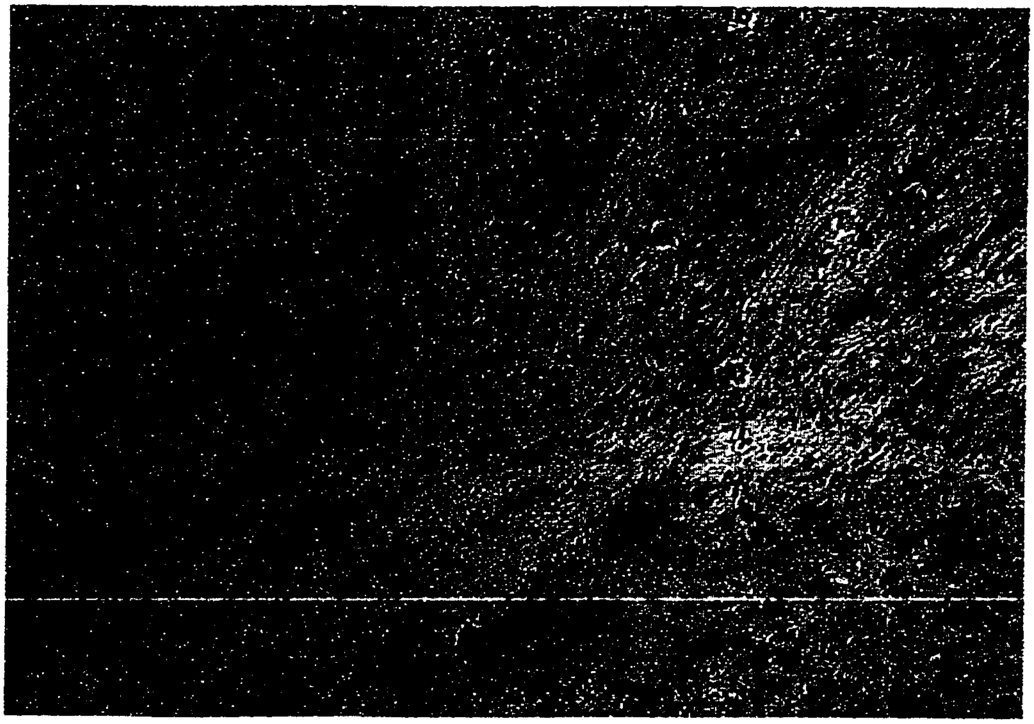

Fig. 5.30B The 10x magnification image of region #2 in slide #225

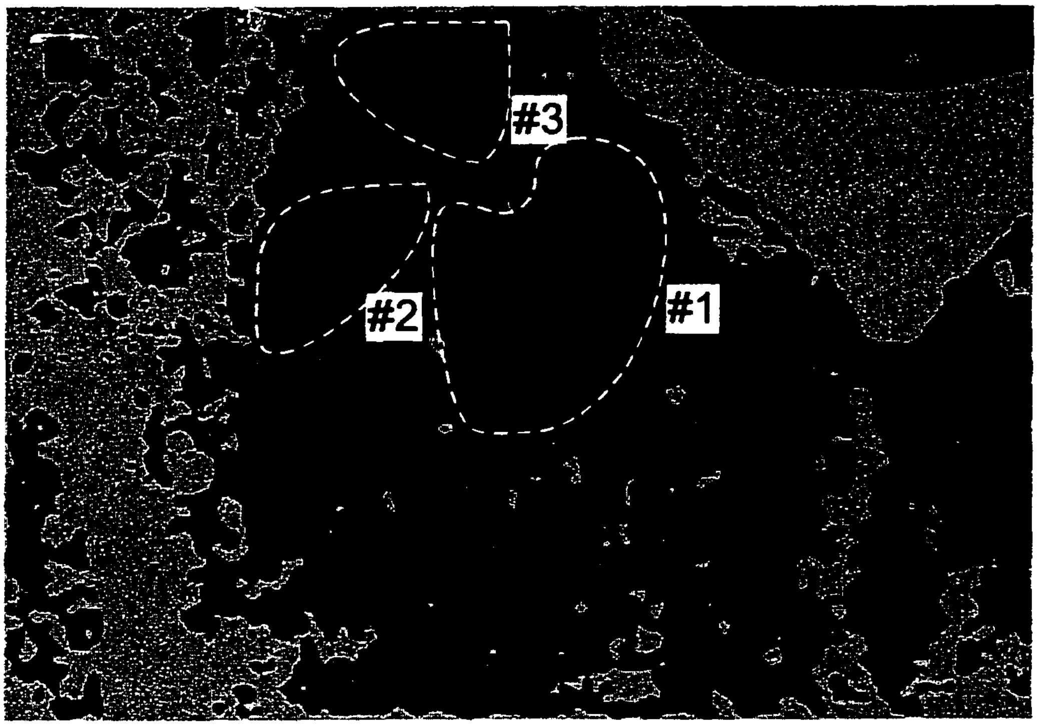

Fig. 5.30C The segmentation image of slide #225

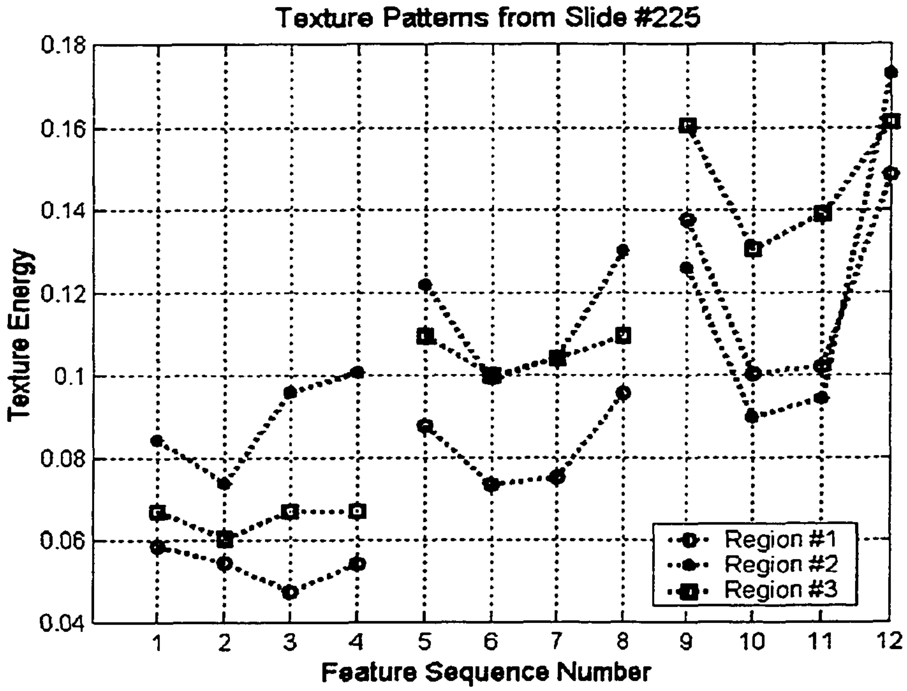

Fig. 5.30D The plot of the texture feature of region #1~3 in slide #225

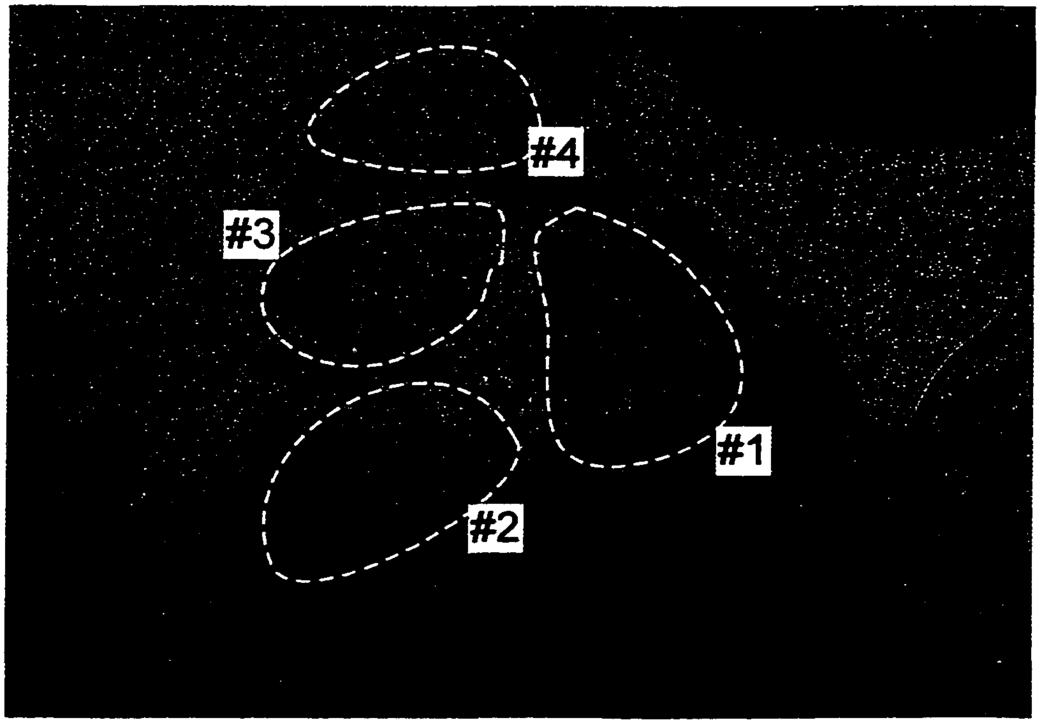

Fig. 5.31A The original image of slide #230

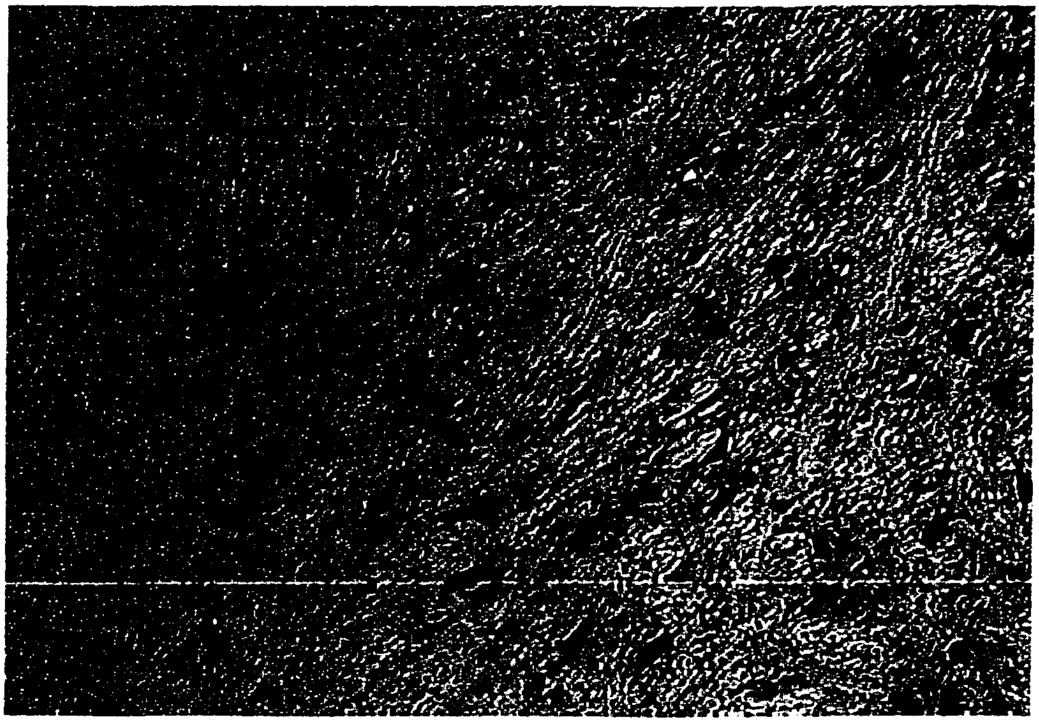

Fig. 5.31B The 10x magnification image of region #3 in slide #230

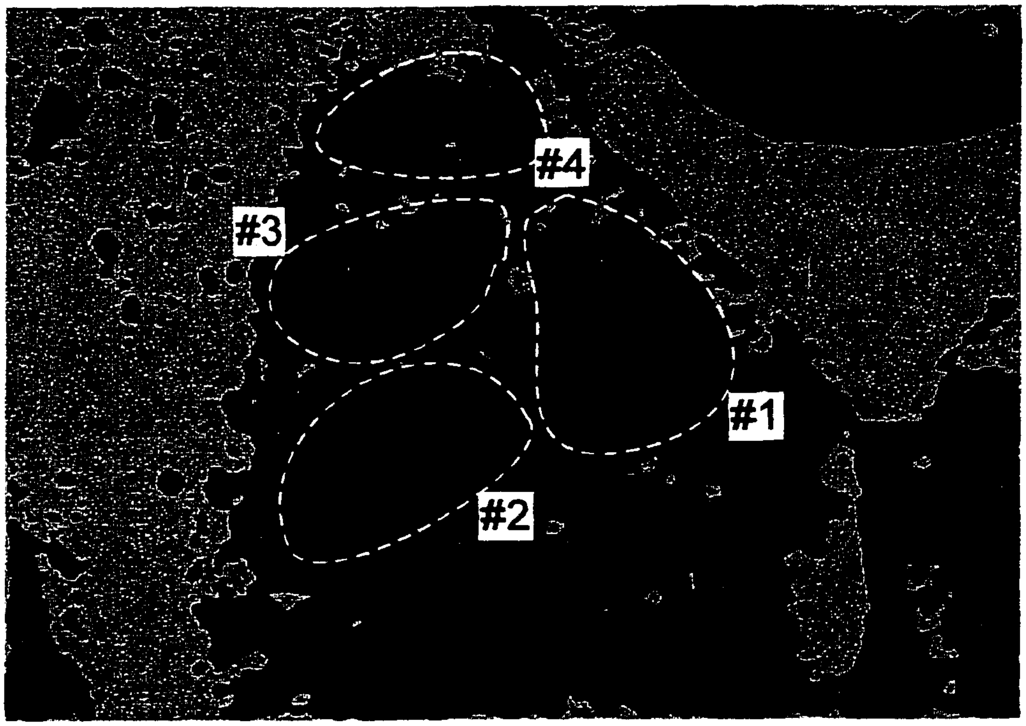

Fig. 5.31C The segmentation image of slide #230

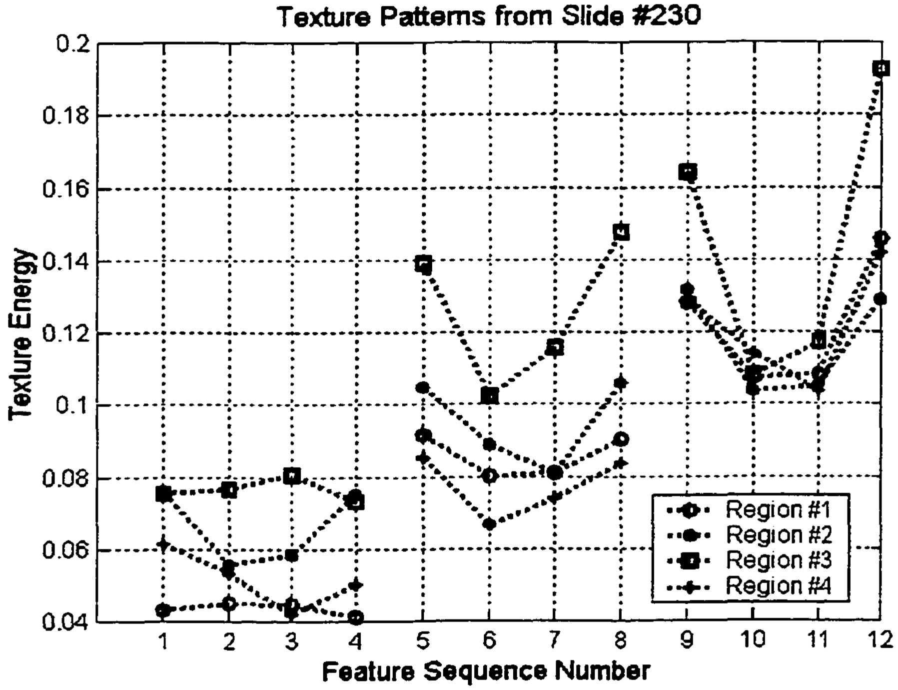

Fig. 5.31D The plot of the texture feature of region #1~4 in slide #230

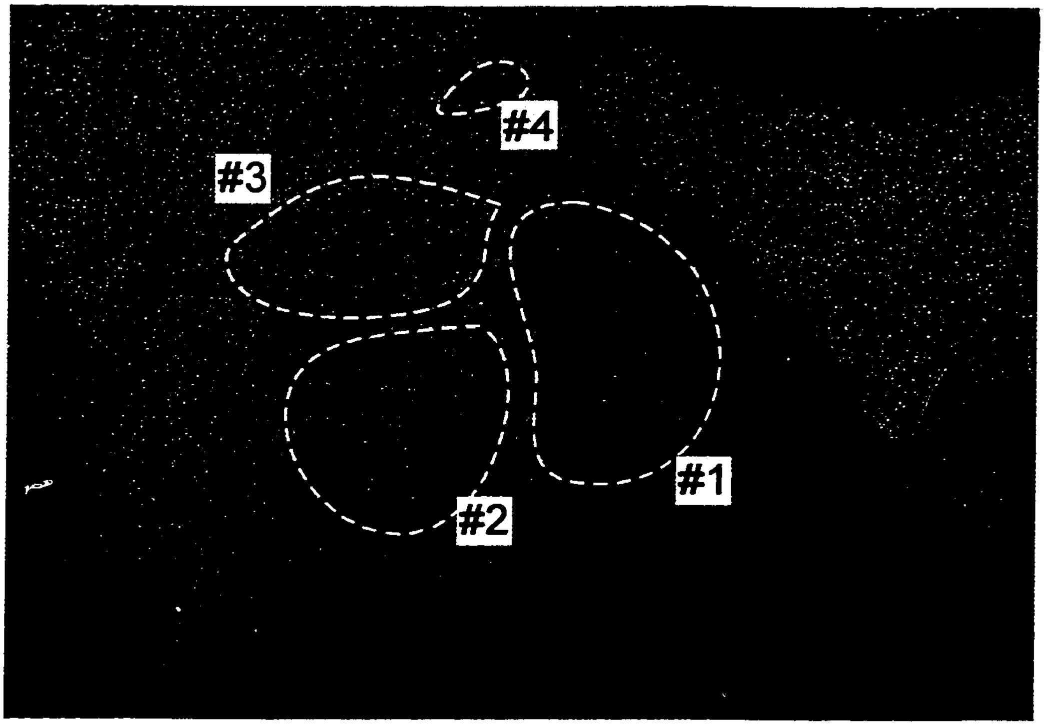

Fig. 5.32A The original image of slide #235

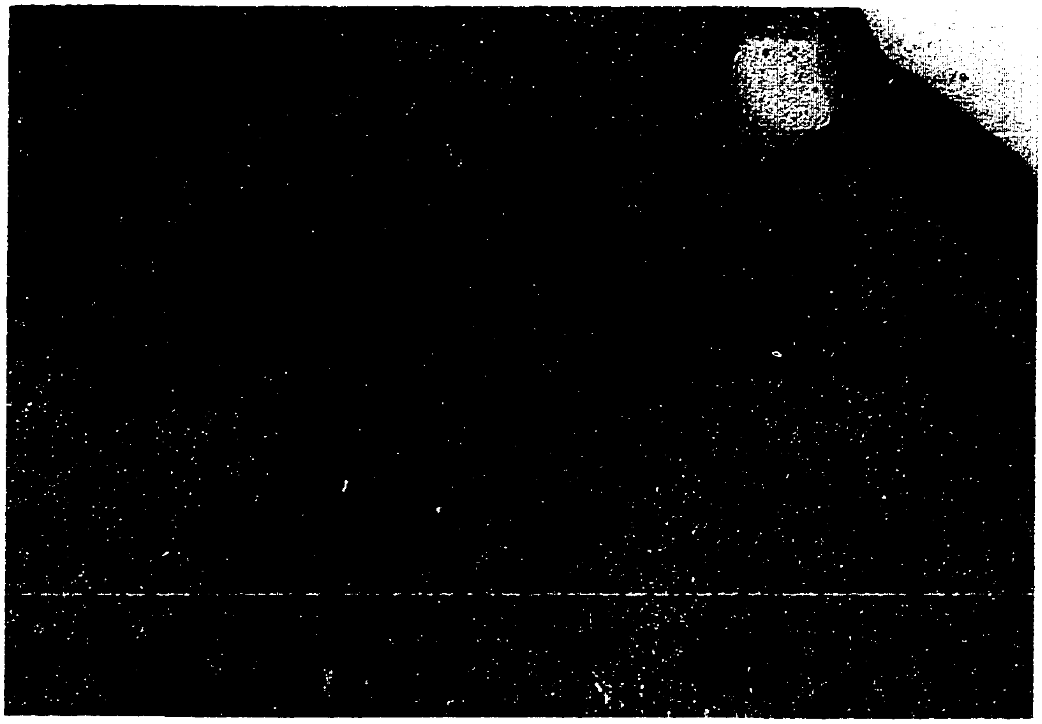

Fig. 5.32B The 10x magnification image of region #1 in slide #235

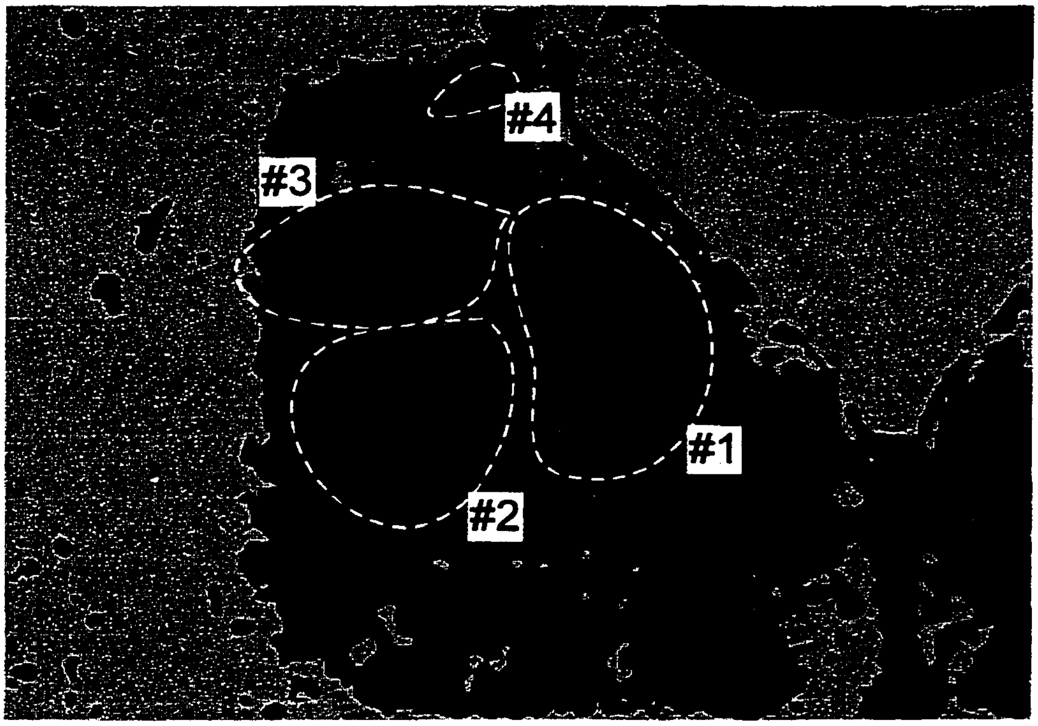

Fig. 5.32C The segmentation image of slide #235

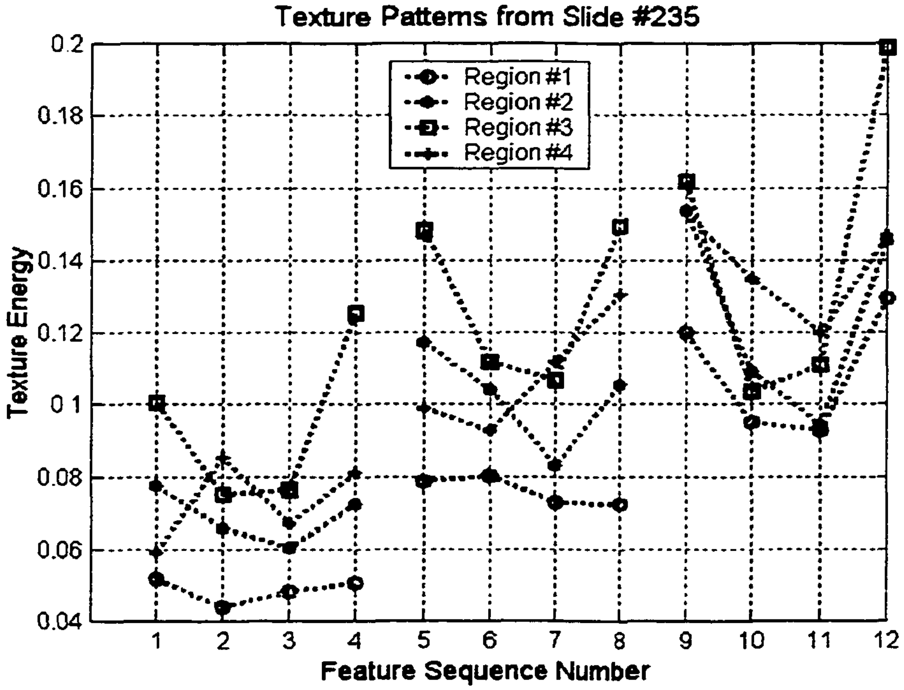

Fig. 5.32D The plot of the texture feature of region #1~4 in slide #235

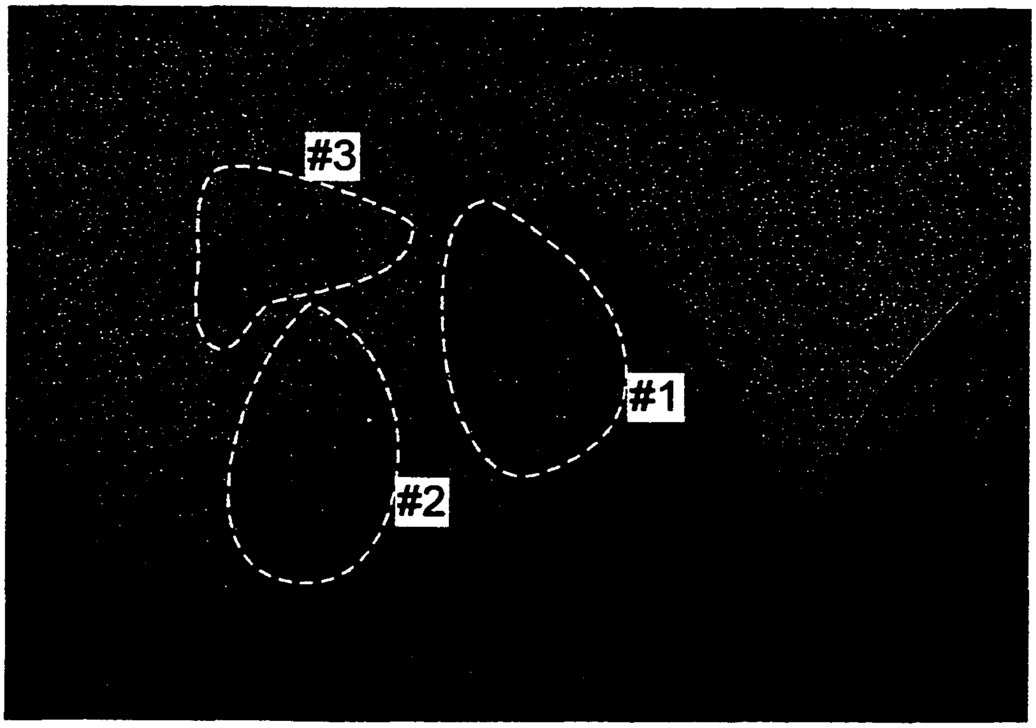

Fig. 5.33A The original image of slide #245

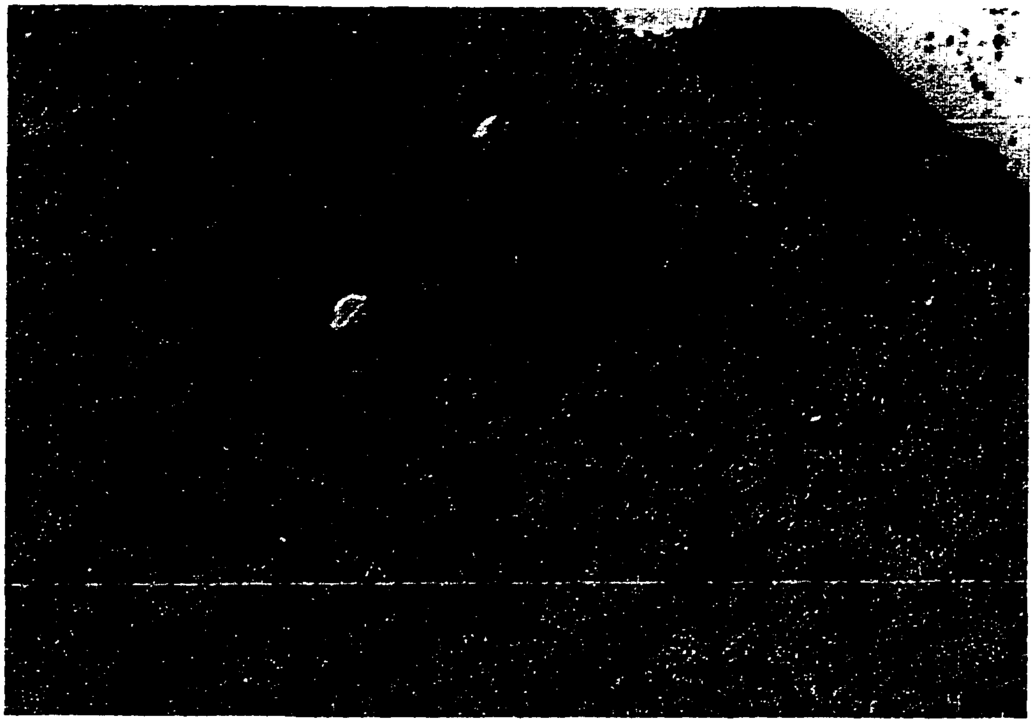

Fig. 5.33B The 10x magnification image of region #1 in slide #245

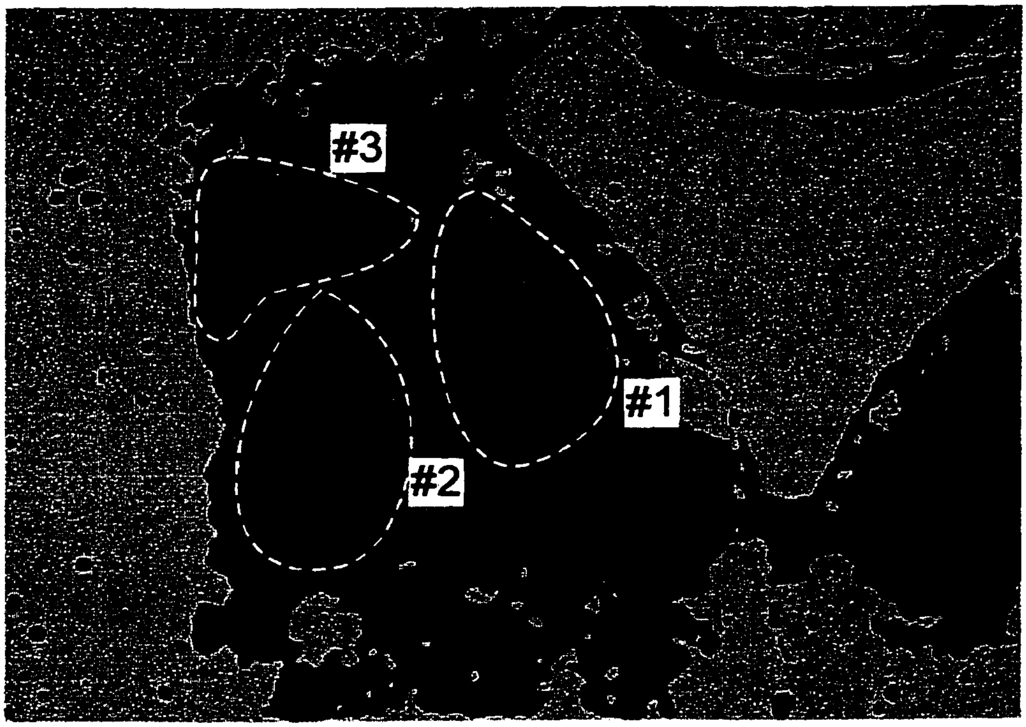

Fig. 5.33C The segmentation image of slide #245

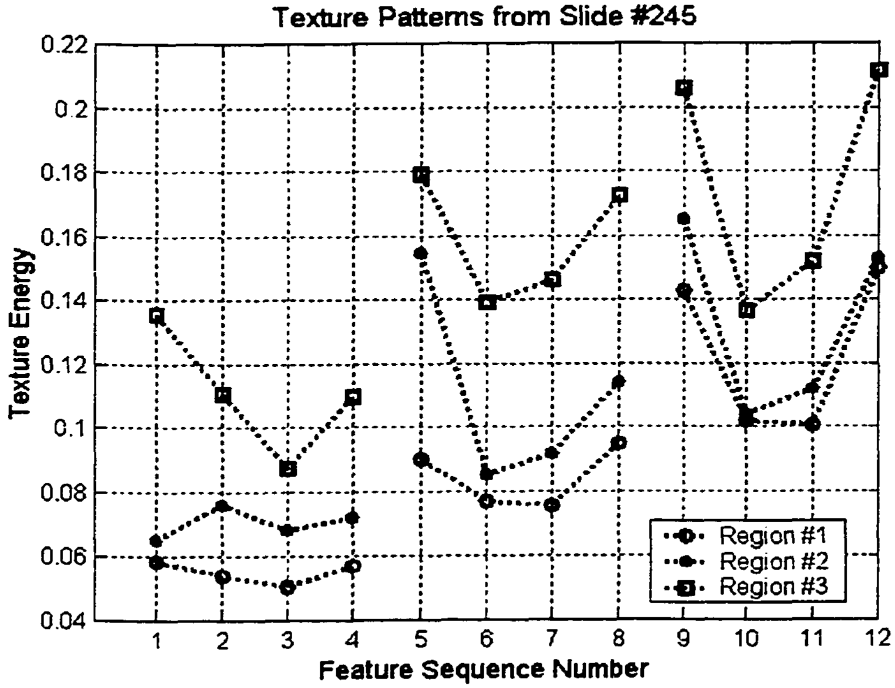

Fig. 5.33D The plot of the texture feature of region #1~3 in slide #245

Fig. 5.34 The 5× magnification image of the abducens nucleus in slide #195.

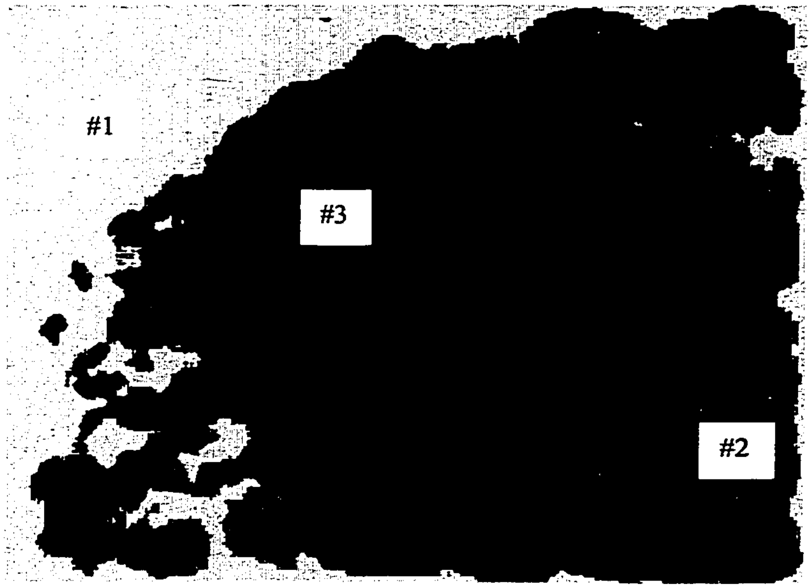

Fig. 5.35 The first level segmentation of Fig. 5.34. It divides the original image into three regions including the abducens (region #3) and two surrounding tissues (regions #1 and #2).

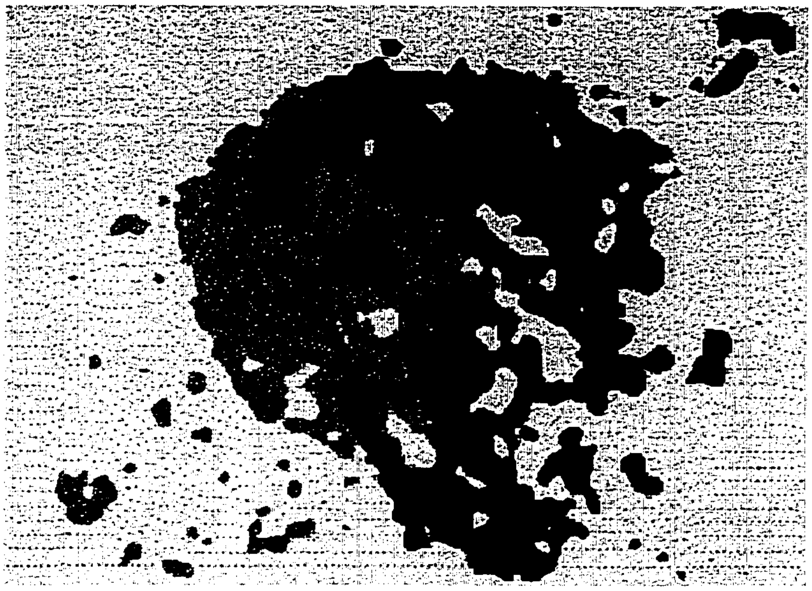

Fig. 5.36 The second level segmentation inside the abducens nucleus in Fig. 5.35. Four sub-regions were specified, and the subdivisions indicate the texture difference between the ventral and the dorsal portions of the abducens nucleus and some heterogeneity inside the dorsal portion of the abducens nucleus.

In conclusion, the sequential processing of brainstem sections with abducens and vestibular nuclei proved that the texture features we used indeed are representative of the texture appearance of our human perception. The identification of dominant cell groupings and the boundaries of the identified regions would be useful for further studies by anatomists in further classifying these regions.

CHAPTER 6. APPLICATION OF TEXTURE FEATURE ANALYSIS TO UNDERSTANDING BONE STRUCTURE

Bone structure has architectural features that are dependent on orientation and density, which is the discriminatory foundation of the wavelet texture analysis. To show the general applicability of our texture analysis approach, we have utilized the program to analyze the structure of bone and define a future utilization of texture based approach.

6.1 Background

Bone is a complex body tissue, which regulates its volume and architecture to accommodate two competing responsibilities: structural and metabolic [15]. The structure of bone provides the framework of the body to protect organs and facilitate locomotion, while the metabolic duty of the bone maintains the essential minerals the body needs. This dual responsibility is manifested by the fact that bone tissues are constantly remodeling in the regulated processes of formation and resorption. The body will resorb the bone by consuming the mineral, and in return, it will stimulate the bone to regenerate more of itself. In the cellular level, the two bone-cell types responsible for formation and resorption are osteoblast and osteoclast respectively. The viability of the bone system depends on a regulated balance of the two processes.

Bone structure analysis plays an important role in describing bone activities and is an effective tool in the diagnosis of bone diseases such as osteoporosis, which is a symptom arising from the reduction of calcified bone tissues. The essential aspect of bone analysis is to quantify bone structure based on its biological and mechanical differences. Of all the structure measurement methods, bone histomorphometry, based on classic stereology, makes a measurement at the intermediary level of organization of bone. It has been the only method that gives access to a direct and precise analysis of the cellular and tissue mechanisms of bone [16].

The methodology entails taking bone biopsies and making sections to be analyzed under a microscope. The sample will be prepared prior to decalcification and stained before being analyzed. Some important parameters that have been defined to represent the static and dynamic properties of bone structures are: 1) the amount of bone, 2) the micro-architecture of spongy bone, 3) bone formation and resorption parameters. Manual measurement, such as point counting of bone that intersects a grid placed on top of the biopsy sample, has almost been abandoned due to the tedious nature of the method. Methods based on automated or semi-automated image analyzing system have been more favored to reduce the analysis time.

In terms of composition, the majority of bone is made of inorganic mineral, together with organic matrix, cells and water. It is the architecture of bone, however, that gives it structural resiliency and strength. Architecturally, bone is comprised of two types of structural forms: cortical and cancellous. Together, they constitute 80% and 20% of the whole skeleton respectively, and are strategically arranged to evenly distribute functional stresses [101]. One of the important subjects of bone analysis is the organization of cancellous bone [17]. The question is how the constituent trabecular struts are oriented and inter-connected, and how they react to change their alignment as the result of disease or fracture. At the microscopic level, bone takes on either the well-organized lamellar bone, which has a layered appearance or the disorganized woven bone. The irregular woven bone is the product of rapid bone formation and will eventually be remodeled into denser lamellar bone. Fig. 6.1 shows a schematic of a long bone shaft and the anatomy of cortical and trabecular bone. Fig. 6.2 shows in details some of the forms of the typical cortical and cancellous structures, and that of lamellar and woven bone [15].

It is believed that the traditional bone histomorphometry provides effective information concerning the biological properties of bone, as it measures the parameters related to the bone cell-surface activities. Particularly, it gives the quantitative description of the amount, patterns and rates of bone formation and resorption as the results of osteoblastic and osteoclastic interactions. However, these measurements are not genuinely meant to fully describe the bone structure and the mechanical properties of the bone development [15]. In fact, the practice of setting up test points in stereological study effectively eliminates the anisotropic variations to focus on the cell-surface activities [15]. Additionally, while some of these parameters are relatively easy to define, others are hard to define quantitatively. Take trabecular bone for example, two important measures, which many of other histomorphometric parameters are based on, are: 1) Trabecular bone volume fraction (Tb.V/TV, %), and 2) Trabecular number (Tb.N, #/mm) [15]. It is understandable that the volume fraction, which represents the percentage of the total volume of cancellous bone tissue, only measures the amount of bone materials. Although it has been found that the bone volume fraction is highly correlated with some of the mechanical properties of bone, i.e. the stiffness and strength. Still the same measurement will not give the information of how the bone tissue is morphologically arranged and connected. Trabecular bone is characterized by various arrangements and orientations of rod-like and plate-like elements of lamellar bone tissue. It is clear that the architecture and the compactness of these bone elements versus the space in between, and the orientation of their overall arrangement, are not so straightforward to describe.

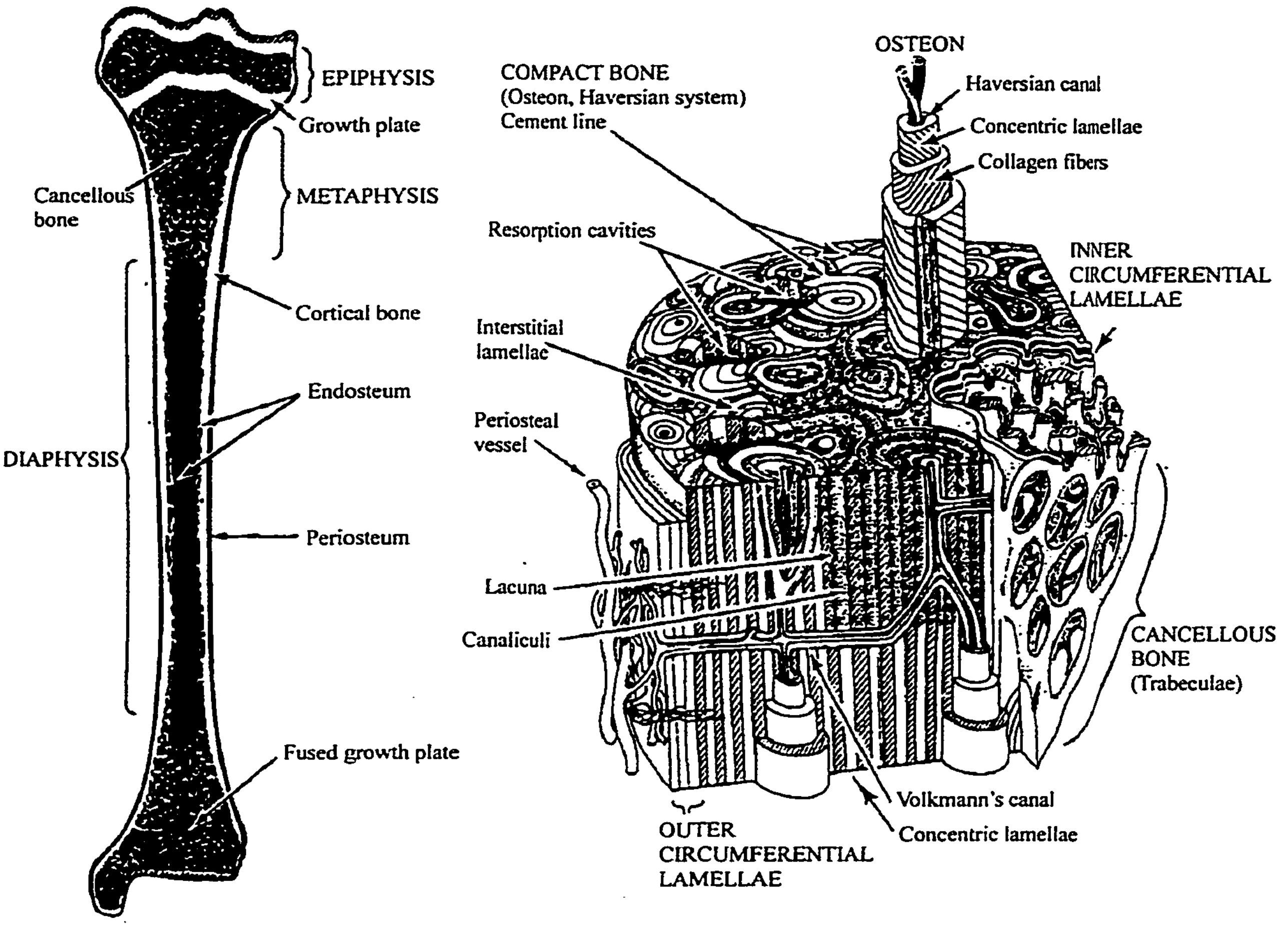

Fig. 6.1 Schematic of a long bone shaft and anatomy of cortical and trabecular bone. The cortical bone is composed mainly of haversian systems or osteons of concentric lamellae with inner and outer circumferential lamellae at the periphery. Many completed osteons can be seen, each with its central haversian canal, cement line, concentric lamellae, canaliculi, and lacunae. Note the orientation of the collagen fibers in successive lamellae in the protruding osteon. Cross connections between osteons are established by volkmann's canals. Volkmann's canals connect with periosteal vessels and the marrow cavity and, unlike the haversian canals, lack a covering of concentric lamellae. Interstitial lamellae are seen between completed haversian systems. Three resorption cavities are also depicted. *Adapted from WSS Jee, Histology, Cell and Tissue Biology* (Taken from [15])

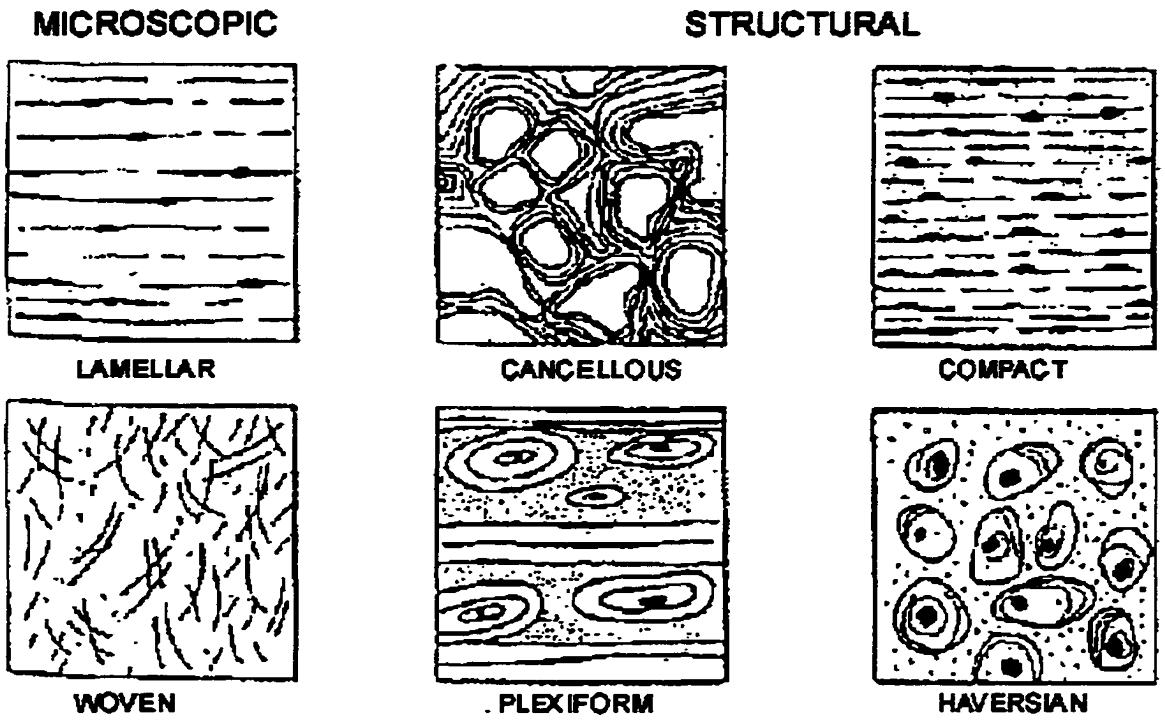

Types of Bone
Adapted from F. Kaplan, et. al., Ch.4, Orth. Bas. Sci, AAOS

Fig. 6.2 Types of bone (Taken from [15]).

Oxnard [102] used both optical and computed Fourier analysis on the human lumbar vertebra. He found out that while most of the bone is orientated at 0° and 90°, there are some portions of the cancellous structure that are orientated at about 60° to the horizontal. This was both demonstrated in the Fourier domain and visually in the electron microscopy picture. He also applied the Fourier analysis to the discrimination of patterns of normal and osteoporotic bones. The optical transforms of radiographs of bone sections of human vertebrae showed that male and female in teens had the most salient orthogonal form of power spectrum, indicating horizontal and vertical organizations. In contrast, male and female in their 70s had more diffused and anisotropic distribution, indicating smaller trabecular elements – sign of the loss of bones. More interestingly, the author found that both male and female aged 30 had contrasting patterns with orthogonal and non-orthogonal distribution respectively.

The benefit of the computational Fourier transform (FFT) is that it can break down the original radiograph into smaller regions so that it can be applied to them accordingly. This way, one could look into the regional differences. The author compared the Fourier transform of the radiographs of the thick section of the human lumbar vertebra, which were from both an 18-year-old female and a 79-year-old female with marked osteoporosis. The pattern for the one with osteoporosis clearly demonstrated degradation away from the orthogonal shape with regional variations. Oxnard's research showed that the orientation does provide an important tool in the pathological aspect of the bone analysis.

Schaffler *et al* [17] also used Fourier analysis to demonstrate the orientation disparity in terms of the power spectrum for various simulated bone cells, which exemplified one aspect of the heterogeneity of the bone morphology. It was shown that four simulated texture pattern having the same number of dots of the same size, which could not be distinguished by conventional stereology. The Fourier power spectrum plots, which illustrate the power content versus angular positions, readily demonstrated the different directionality of the four texture patterns.

Fourier analysis is a global analysis tool. While you can divide the coordinates into angular divisions, it does not provide the same locality and the versatility of wavelet analysis. Moreover, although we could see the disparity of Fourier spectrum of various bone structures, there is not a generalized quantitative way to characterize this difference. The Gabor wavelet based texture analysis scheme is able to give very localized texture information on a pixel basis, and provide more insight into bone structure as it is perfectly suited to quantifying regional variations.

6.2 Results

We used the Gabor wavelet based texture feature to analyze the density and orientation properties of bone struts. The test bone images were generated by taking microscopic photos of sections sampled from the metacarpal bones of a dog. (Bone slides courtesy of Dr. Mitch Schaffler). Four of the samples are given as Fig. 6.3 and 6.4. Fig. 6.3 shows two panels of bone samples with similar total bone density but with distinctive orientation variations. In Fig. 6.3(A), the bone struts are aligned mostly horizontally, while Fig. 6.3(B) shows mostly vertically arranged bone struts. Fig. 6.4 shows two bone samples with similar orientational variations (slightly horizontally arranged struts), but with distinctive density difference. Fig. 6.4(A) shows distinguishable signs of bone loss, while Fig. 6.4(B) shows well connected healthy bone.

We calculated the texture energy features for the bone structures in all of the four sample images, and the results are shown in Fig. 6.5, and Fig. 6.6. Fig. 6.5 shows the texture difference characterized by the orientational difference of bone structures, with the interested regions encircled by the dotted line and the solid line. The texture feature as the function of different frequency bands and orientations clearly demonstrated that the texture difference between Fig. 6.5(A) and 6.5(B) is at the orientations of 0° and 90°, while the overall energies are very similar. Fig. 6.6 shows the texture difference characterized by bone density. The bone sample (Fig. 6.6(A)) with signs of osteoporosis (bone loss) is represented by a markedly reduced texture energy along all orientation and frequency bands, compared with the healthy bone (Fig. 6.6(B)). However, the orientational variation within any frequency band remains the same. These kinds of texture pattern differences should provide important information in bone histomorphological studies.

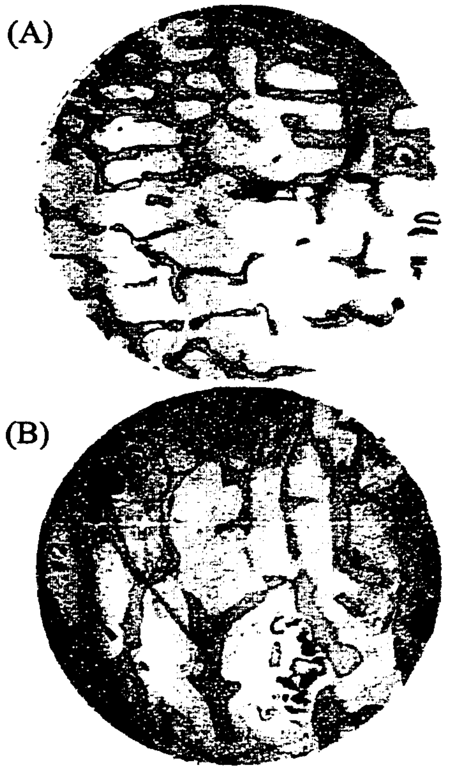

Fig. 6.3 Bone samples showing predominantly orientational difference. (A): bone struts are mostly horizontally arranged. (B): bone struts are mostly vertically arranged.

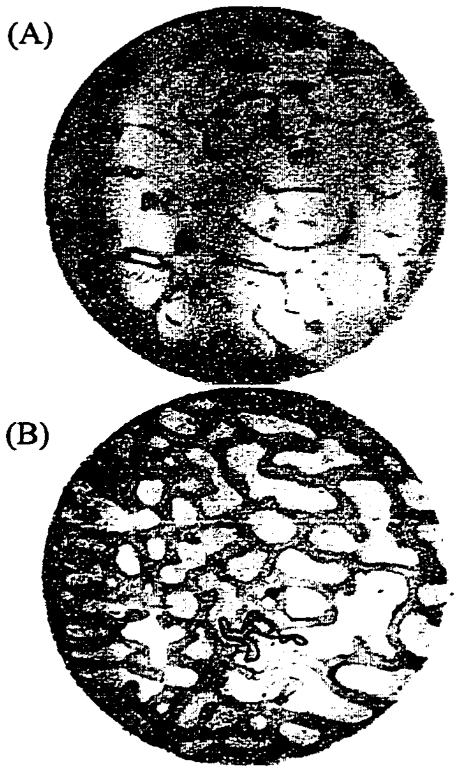

Fig. 6.4 Bone samples showing predominantly density difference. (A): bone struts are broken and reduced in total amount (signs of osteoporosis). B): healthy bone struts.

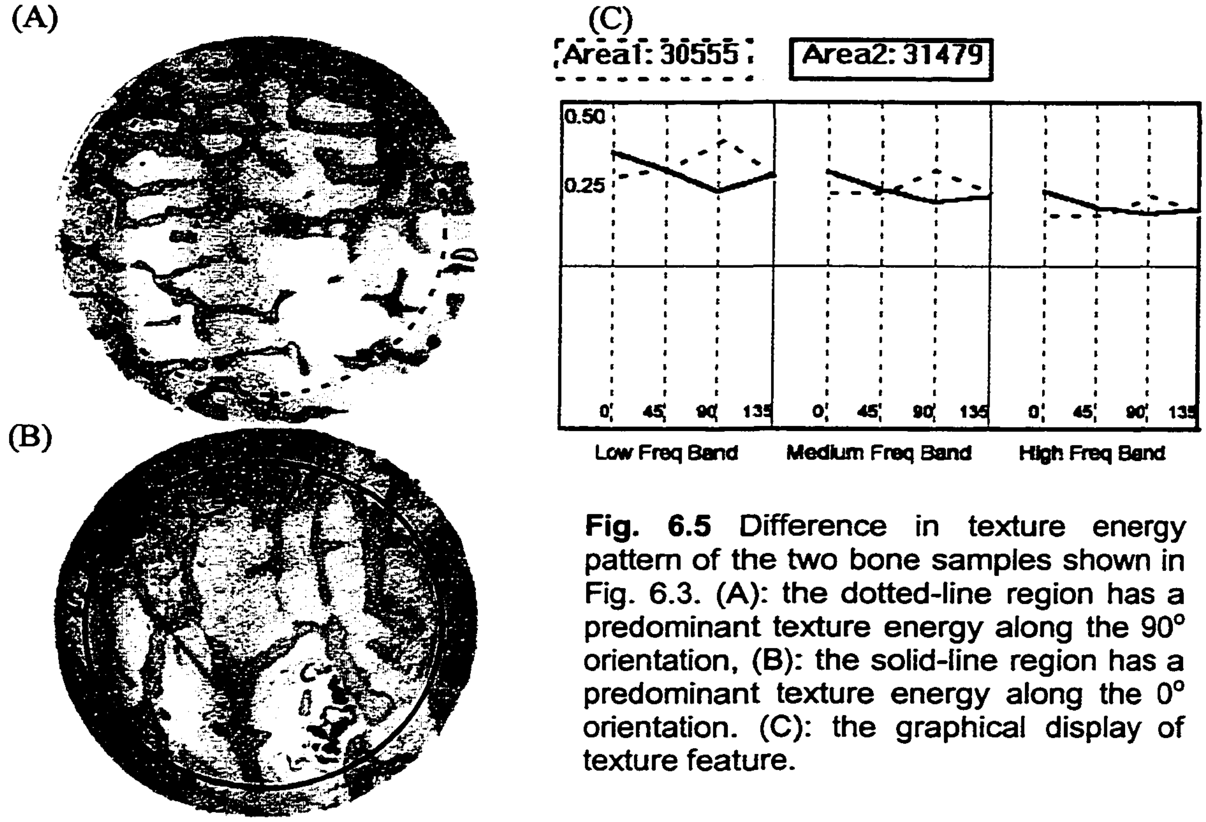

Fig. 6.5 Difference in texture energy pattern of the two bone samples shown in Fig. 6.3. (A): the dotted-line region has a predominant texture energy along the 90° orientation, (B): the solid-line region has a predominant texture energy along the 0° orientation. (C): the graphical display of texture feature.

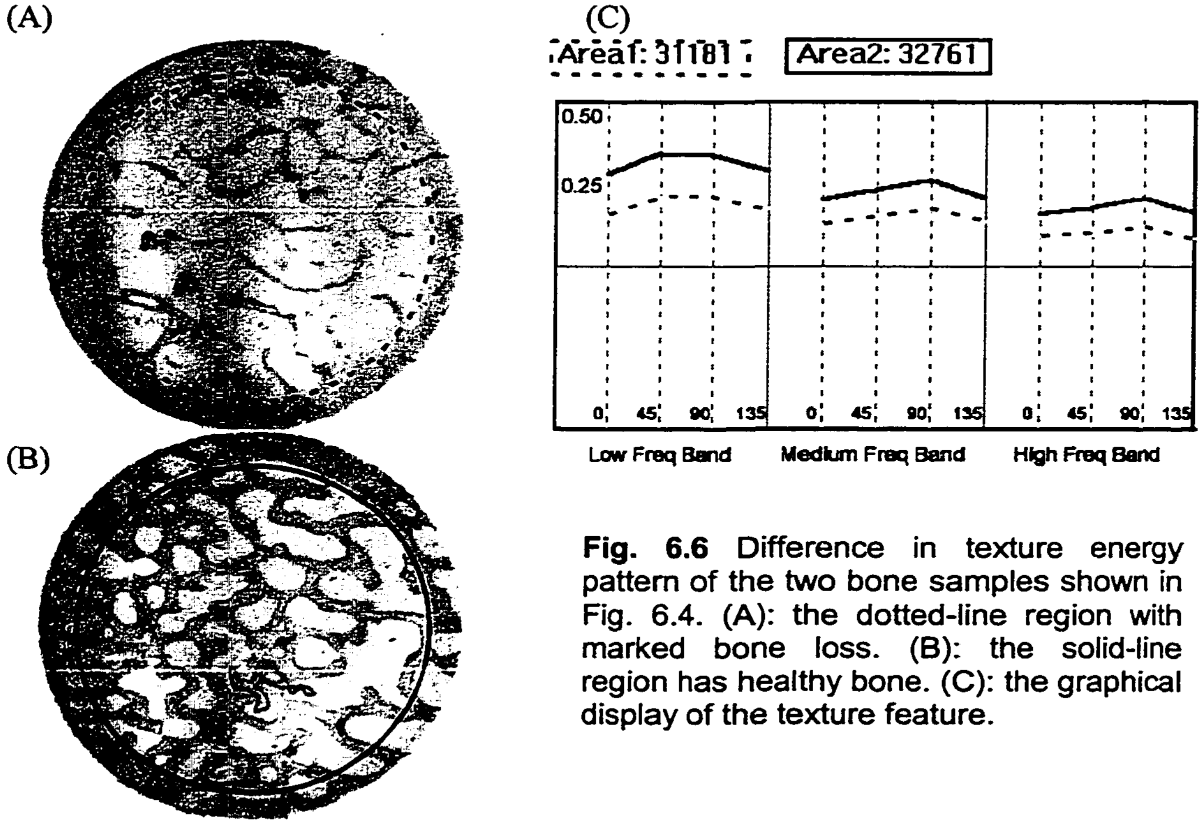

Fig. 6.6 Difference in texture energy pattern of the two bone samples shown in Fig. 6.4. (A): the dotted-line region with marked bone loss. (B): the solid-line region has healthy bone. (C): the graphical display of the texture feature.

CHAPTER 7. CONCLUSION AND DISCUSSION

In summary, we have the following conclusions: the Gabor wavelet based texture feature provides an effective measure for distinguishing neuro-anatomical structures, because of its spatial frequency and orientation discriminatory properties. Our research showed that multi-resolution texture based segmentation could identify some anatomically meaningful structures in a typical brainstem section image, especially the more prominent nucleus groups such as the abducens nucleus. It has also been useful in identifying the vestibular nuclei. In addition, it provides unique micro-architecture information of bone structures, which could assist the study in bone histomorphometry. The applicability of the Gabor wavelet based texture feature to both neural analysis and bone analysis demonstrated its potential usefulness to an even wider range of applications. Finally, the texture feature could also be used as a potential descriptor for quantifying general classes of anatomical structures.

7.1 Contribution of the Dissertation

1) We developed a methodology to analyze anatomical structures based on their texture differences. The texture feature is constructed based on the output of Gabor wavelet transform, and a texture energy extraction. We developed a heuristic way of choosing the frequency bands and designing the parameters of Gabor functions. In addition, for neuro-anatomical subjects, we developed a two-level segmentation scheme, where the second level segmentation uses a revised texture feature to better characterize the cell distribution regularity.

2) The multi-resolution implementation of the Gabor wavelet expansion greatly reduced the computation load without incurring significant information loss. That makes using more levels computationally feasible when dealing with textures having substantial low frequency contents.
3) The Gabor wavelet based texture segmentation performance is relatively poor along the region borders, especially where uniform gray-level region is adjacent with textured region. The abrupt gray-level transition falsely introduces high texture energy, and the border area can very easily be misclassified as new texture. The algorithms of uniform region exclusion and texture energy adjustment seemed to perform quite well to overcome this problem.
4) While the texture segmentation has successfully captured the dominant structures, over-segmentation occasionally occurs. This problem can be minimized by an effective relaxation method. We found that the combination of pixel coordinate information, Gaussian smoothed pixel intensity information, and a probabilistic relaxation scheme produced a more robust segmentation result, and will be the potential framework for practical identification work.

7.2 Discussion about the Quantifying Properties of the Texture Feature

The texture features not only can be used as the basis for segmentation, but can also be considered as a quantitative representation of the characteristics of the anatomical structures. The texture property of a segmented textured region can be efficiently represented by the averaged texture feature vector. There are two questions related to the quantitative properties of the texture feature. Firstly, how is the texture feature related to the anatomical parameters with which neuro-anatomists are familiar? Secondly, how uniquely is the texture region described by the averaged texture feature? We will address these questions here.

7.2.1 Interpretation of the Texture Feature

In this section, we will discuss the interpretation of the practical meaning of the feature vector. Neuro-anatomists see the difference in cell groups as the size and spacing of cells, the density and the orientation of the cell distributions, etc. These are the anatomical parameters they are familiar with, but not explicitly represented in the texture feature. However, it is still possible to build up some correlation of the feature vector and the quantification of those direct anatomical parameters.

One important measure reflected in the feature vector is the overall texture energy along all frequency bands. When weighed more towards the high frequency bands, it is a close indication of the cell density, i.e. how tightly are the cells spatially distributed. The second crucial measure, which can be obtained from the feature vector, is the most dominant orientation of the cell alignment. Closer observation revealed that the information about cell size could also be extracted from the feature vector. Usually bigger cells tend to have larger spacing. Bigger cells with larger spacing will accentuate lower frequency responses. In that regard, the frequency band which has the most energy is highly dependent on the cell size, and a large magnitude in the high frequency band indicates smaller cell size. Additionally, the total texture energy weighted towards low frequency bands affect the determination of the cell sizes.

To summarize, if the Gabor-related texture energy feature vector is denoted by Eq. 3.2.8 ($1 \sim M$ bands, $1 \sim N$ orientations), then three measures can be formulated as follows:

1) Density measure: averaged value of all Gabor-related texture energy features, weighted more towards the high frequency bands.

$$M_{density} = \frac{\sum_{m=1}^{M}\left(2^{m-1}\sum_{n=1}^{N} e_{mn}\right)}{(2^{M}-1)\cdot N} \qquad (7.2.1)$$

2) Orientation measure: the dominant orientation of the texture energy, which could be obtained by summing features of individual frequency band of the same orientation, and picking the orientation with the maximum feature summation.

$$M_{orientation} = (n_d - 1)\pi / N, \quad \{\, n_d \in (1:N) \;\; and \;\; \sum_{m=1}^{M} e_{mn_d} = \max(\sum_{m=1}^{M} e_{mn}) \,\} \qquad (7.2.2)$$

3) Cell size measure: First calculate a weighted total energy E_{lo} by summing up the energy features of all the frequency bands and orientations, with more weight put towards lower frequency bands (Eq. 7.2.3). Then, determine the energy-weighted averaged frequency F_e using (Eq. 7.2.4), where u_{0m} is the spatial frequency for band m. Finally, dividing E_{lo} by F_e will give us a measure that has a bigger value for bigger cell sizes (Eq. 7.2.5).

$$E_{lo} = \frac{\sum_{m=1}^{M}\left(2^{M-m}\sum_{n=1}^{N} e_{mn}\right)}{(2^{M}-1)\cdot N} \qquad (7.2.3)$$

$$F_e = \frac{\sum_{m=1}^{M}\left[\left(\sum_{n=1}^{N} e_{mn}\right)\cdot u_{0m}\right]}{\sum_{m=1}^{M}\sum_{n=1}^{N} e_{mn}} \qquad (7.2.4)$$

$$M_{cell-size} = \frac{E_{lo}}{F_e} \qquad (7.2.5)$$

It should be noted that these measures are relative and do not represent a metric. The quantitative nature of the texture feature other than used in segmentation has not yet been well studied. Our current work has shown some promise in that direction, and a more comprehensive study, which could provide a more accurate description of neural textures in a traditional neuro-anatomical sense, could be considered in future research.

7.2.2 A Distance Definition for Comparing Feature Patterns

An alternative quantitative approach would be to establish a distance definition to measure the closeness of a given texture pattern to a known cell group based on the texture feature vector. One common distance measure is the Euclidean distance. The problem with the Euclidean distance is that it does not account for the pattern difference as the result of the intra-feature variation. In other words, two features can have identical Euclidean distances to a third feature, but are totally different themselves. One measure that can account for the differences between two feature vectors other than the distance is the similarity coefficient. Given vectors x and y,

$$\begin{aligned} x &= (x_1, x_2, \cdots, x_n) \\ y &= (y_1, y_2, \cdots, y_n) \end{aligned} \tag{7.2.6}$$

the similarity coefficient (*SC*) can be defined as:

$$SC = \frac{xy}{|x| \cdot |y|} = \frac{x_1 y_1 + x_2 y_2 + \cdots + x_n y_n}{\sqrt{x_1^2 + x_2^2 + \cdots + x_n^2} \cdot \sqrt{y_1^2 + y_2^2 + \cdots + y_n^2}} \tag{7.2.7}$$

There is a problem with this similarity coefficient, which is essentially the *cos()* of the angle between two vectors. It tends to be very close to 1 in the case of texture feature vectors when representing the texture patterns of neural tissues. Since our texture feature vector has all positive elements, another similarity measure, which spreads the (0, 1) range more aggressively is the *Tanimoto* measure [103]. The *Tanimoto* measure (*T*) was initially defined to measure the similarity between bit vectors. It can be extended to deal with real-valued vectors, and is given as:

$$\begin{aligned} T &= \frac{xy}{xx + yy - xy} \\ &= \frac{x_1 y_1 + x_2 y_2 + \cdots + x_n y_n}{(x_1 x_1 + x_2 x_2 + \cdots + x_n x_n) + (y_1 y_1 + y_2 y_2 + \cdots + y_n y_n) - (x_1 y_1 + x_2 y_2 + \cdots + x_n y_n)} \end{aligned} \tag{7.2.8}$$

To convert this similarity measure to a dissimilarity measure, the *Soergel* measure (*S*) is defined as:

$$S = 1 - T \qquad (7.2.9)$$

We would like to combine the effects of both the Euclidean distance and the *Soergel* measure. A combined distance can be defined as:

$$D_{combined} = \sqrt{E^2 + S^2} \qquad (7.2.10)$$

Based on this definition of distance, we can compare texture feature of a given texture region with patterns of known cell groups.

Initial usage of this combined distance for the images of slide 180~245 (Fig. 5.21~Fig. 5.33), have indicated that the distance value provides some direct indication of our perception of the pattern difference. Thus, it should be a convenient and efficient way of quantitatively comparing texture features. The results are summarized in Tables 7.1.

Slide # **Rgn Pairs**	**180**	**185**	**190**	**195**	**200**	**205**	**210**
Region 1 – Region 2	0.302	0.152	0.265	0.132	0.077	0.106	0.163
Region 2 – Region 3	0.136	0.204	×	0.345	×	×	×
Region 1 – Region 3	0.445	0.301	×	0.245	×	×	×
Slide # **Rgn Pairs**	**215**	**220**	**225**	**230**	**235**	**245**	×
Region 1 – Region 2	0.054	0.082	0.123	0.066	0.106	0.091	×
Region 2 – Region 3	0.083	0.031	0.101	0.124	0.193	0.197	×
Region 1 – Region 3	0.118	0.078	0.080	0.136	0.317	0.287	×

Table 7.1 The combined distance of texture features between the marked regions in each slide. Non-existent region pairs are marked by "×".

7.2.3 A General Approach to the Textured Image Representation

It is important to indicate that the averaged texture feature vector is a convenient representation of the overall texture property of the region being averaged. However, it is presently not possible to uniquely describe a random pattern of texture region with a single texture feature. That is because there are numerous ways of distributing texture feature vectors which could end up producing the same averaged feature vectors. If we can assume that the texture feature is uniformly distributed in space and the feature value follows a specific probabilistic distribution such as Gaussian, synthesis from a single feature vector is possible. In that case, a single feature vector is a definitive quantitative description of the underlying texture pattern. However, it is not clear what kind of freedom we can have to manipulate the spatial distribution of the texture feature and still generate a similar texture. In real-world images, especially the neuro-anatomical images, local spatial variations of the texture within a supposedly homogeneous textured region do exist, thus making it impossible to accurately reconstruct image based on the averaged texture feature alone. Similarly, while we can use pixel intensity variance to measure a region's smoothness, it is impossible to reconstruct an image based on its mean and/or variance alone, because of the infinite possibilities of pixel permutations. A more realistic way of quantifying a texture region while still maintaining the necessary spatial information for possible reconstruction would be to employ a quad-tree structure to represent a textured image (Fig. 7.1). The root $T_0(0, 0)$ of the quad-tree is the single averaged texture feature vector of the whole region, and it has four children, $T_1(0, 0)$, $T_1(0, 1)$, $T_1(1, 0)$, $T_1(1, 1)$, each represents the averaged texture of one of the sub-regions obtained by dividing the original image into four equal pieces. Each of the four children can then be further divided into four grandchildren. The total number of levels to be used will depend on the image size and image contents. With this scheme, two textures can be compared in a hierarchical way. The comparison starts form the top level. If the texture features representing two entire textured images are different, the two textures in question are considered different, otherwise, comparisons will be continued to the lower levels, until differences are found. If all levels have identical features, we can definitively claim the identity of the two textures. A quad-tree structure also makes it possible to approximately reconstruct the original image when it is required. The lowest level (all leaves) will provide the nearest approximation when compared to the original textured image.

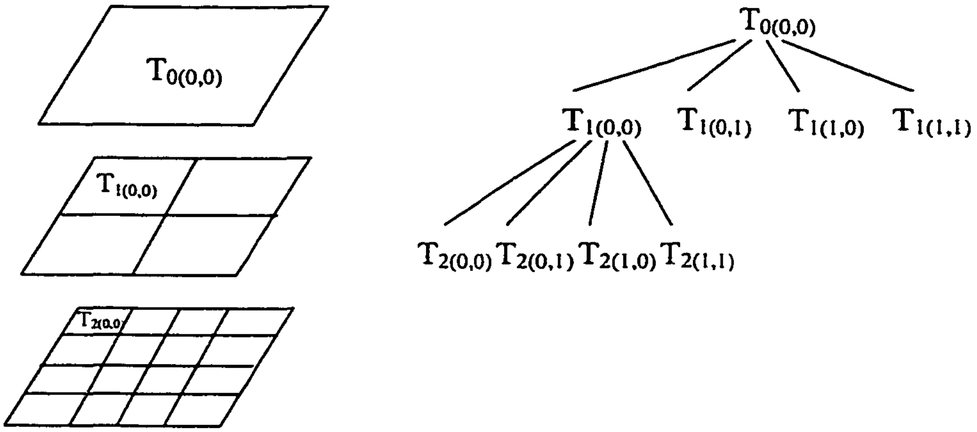

Fig. 7.1 A quad-tree representation of textured image. $T_n(x, y)$ means the averaged Gabor wavelet based texture feature at the n^{th} level with the grid (x, y).

7.3 Future Research

We will explore the following areas for future research:

1) Improve the clustering algorithm to make it possible for unsupervised segmentation, so that it is unnecessary to prescribe the number of clusters, and the system can be run in an unattended way.
2) Develop a general scheme for quantifying spatially varying texture regions that also retain the information for possible reconstruction of texture regions.
3) Try to establish a more accurate correlation between the texture feature vector and the anatomical parameters.
4) Explore some aspects of the three-dimensional nuclear representation from serial sections. This will be important in identifying electrode penetration during single cell recording experiments.

APPENDIX

A. The Basic Structure of the Computer Program

Most of the work in this thesis was implemented in a texture segmentation program called Tseg.exe, which is a Win32 application with about 12,000 lines of code developed under the Microsoft Visual C++ environment. The Microsoft Foundation Class (MFC) framework was used, which enforces a Document-View architecture for application development. Consequently, majority of the functionality of the program goes in three MFC derived classes: `CTsegDoc`, `CTsegView` and `CClstView`. The Document class `CTsegDoc` encapsulates most of the data processing functions, while the two view classes, `CTsegView` and `CClstView`, deal with all the data visualization tasks. Because of the nature of the Windows programming, most of the functions are implemented as Windows message handlers, which respond to user inputs or command message handlers, which respond to menu commands. In particular, `CTsegView` provides an interactive way for user to manually draw regions of arbitrary shapes and sizes to analyze and compare the texture feature data within those regions. The data can be displayed either in text or as a graphical plot, and can be recorded for further processing. Table A.1 lists the essential components of the application and their duty of work. A diagram illustrating the overall structure and the interaction of constituent components is shown in Fig. A.1.

Tseg Classes	**Functionality**
`CTsegApp`	Application initialization and command line processing.
`CTsegDoc`	70+ member functions constitute the essential parts of the application, including Gabor transform, texture feature generation and normalization, and data clustering, etc.
`CTsegView`	Provides interactive user interface to select arbitrary regions with any size and shape, and display the averaged texture features in text and in graphics, or export them into a file.
`CClstView`	Provides a color-coded data view of the result of the segmentation and the feature images.
`C2ndClstDlg`	Dialog for choosing the target region and the parameters for second segmentation.
`CAutoareaDlg`	Dialog for automatically setting area to be processed.
`CFeatViewDlg`	Dialog for selecting which feature element to display.
`CNtpDlg`	Dialog for setting parameters for non-textured region pre-processing.
`CPrmSetDlg`	Dialog for setting all parameters related to Gabor feature generation and data clustering.
`CSbsDlg`	Dialog for setting parameters for small-blob-sifting.
`CMilApp`	Utility class for setting up the Matrox Meteor-II frame grabber
`CMilGrab`	Utility class for grabbing images from video signal.
`CDib`	Helper class for opening, saving and printing Windows Device-Independent Bitmap Objects and files.

Table A.1 Some of the Tseg classes and the summary of their functionality.

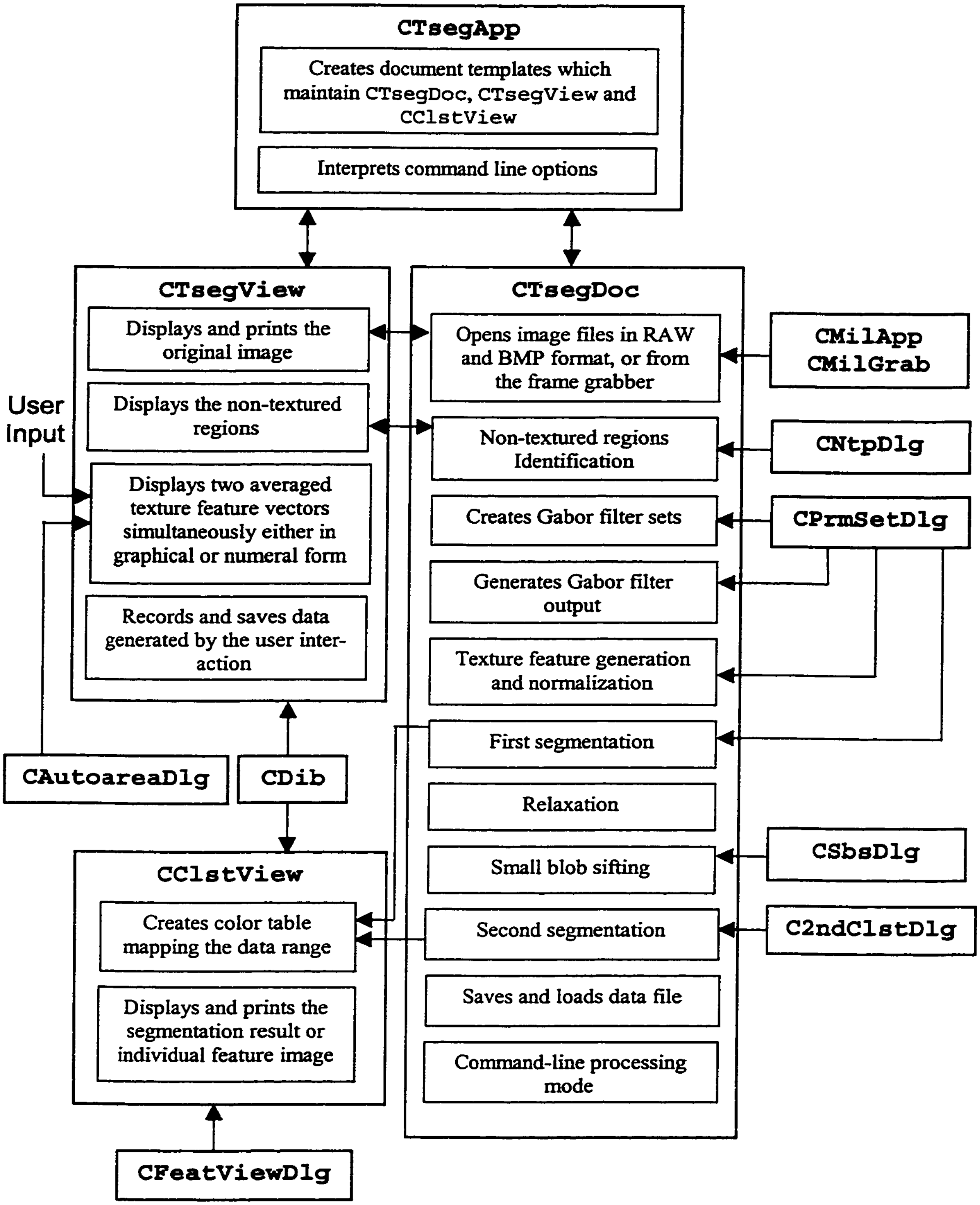

Fig. A.1 Structural diagram of the Tseg application.

BIBLIOGRAPHY

1. Rosenfeld, A. and A.C. Kak, *Digital picture processing*. 1982, Orlando: Academic Press. 435.

2. Castleman, K.R., *Digital Image Processing*. 1996: Prentice-Hall, Inc.

3. Gonzalez, R.C. and P. Wintz, *Digital Image Processing*. 1987: Addison-Wesley. 503.

4. Xiang, Y., *et al.*, *Image-quality enhancement of objects in turbid media by use of a combined computational-photonics approach.* Applied Optics, 1997. **36**(5): p. 1045-1053.

5. Kobashi, M. and L.G. Shapiro, *Knowledge-Based Organ Identification from CT Images.* Pattern Recognition, 1995. **28**(4): p. 475-491.

6. Tsai, C., B.S. Manjunath, and R. Jagadeesan, *Automated Segmentation of Brain MR-Images.* Pattern Recognition, 1995. **28**(12): p. 1825-1837.

7. Acharya, R.S., P. Heffernan, and R.A. Robb, *High-Speed 3D Imaging of the Beating Heart Using Temporal Estimation.* CVGIP: Computer Vision Graphics and Image Processing, 1987. **39**(3): p. 279-290.

8. Li, H., *et al.*, *Object Recognition in Brain CT-Scans: Knowledge-Based Fusion of Data from Multiple Feature Extractors.* IEEE Transactions on Medical Imaging, 1995. **14**(2): p. 212-229.

9. Brodal, A., *Neurological Anatomy: in Relation to Clinical Medicine*. Third ed. 1981: Oxford Press.

10. Merkle, R.C., *Large Scale Analysis of Neural Strutures*, . 1989, Xerox Palo Alto Research Center: Palo Alto, CA.

11. Kandel, E.R., J.H. Schwartz, and T.M. Jessell, eds. *Principles of Neural Science*. Third ed. . 1991, Appleton & Lange: Norwalk. 1135.

12. Martin, J.H., *Neuroanatomy: Text and Atlas*. 1989, New York: Elsevier Science Publishing Co., Inc. 483.

13. Langer, T., *et al.*, *Afferents to the Abducens Nucleus in the Monkey and Cat.* The Journal of Comparitive Neurology, 1986(245): p. 379-400.

14. Capowski, J.J., *Computer Techniques in Neuroanatomy*. 1989, New York: Plenum Press. 483.

15. Rubin, C.T. and J.E. Rubin, *The Biology, Physiology and Morphology of Bone*, . 1996.

16. Meunier, P.J., *Bone Histomorphometry*, in *Osteoporosis: Etiology, Diagnosis, and Management*, B.L. Riggs and L.J.I. Melton, Editors. 1997, Lippincott-Raven Publishers: Philadelphia. p. 299-318.

17. Schaffler, M.B., *et al.*, *Which Steriological Methods Offer the Greatest Help in Quantifying Trabecular Structure from Biological and Mechanical Perspectives?* Forma, 1997(12): p. 197-207.

18. Koch, J.C., *The laws of bone architecture.* Am. J. Anat., 1917. **21**: p. 177.

19. Turner, M.R., *Texture Discrimination by Gabor Functions.* Biological Cybernetics, 1986. **55**: p. 71-82.

20. Bovik, A.C., M. Clark, and W.S. Geisler, *Multichannel Texture Analysis Using Localized Spatial Filters.* IEEE Trans. Pattern Anal. Machine Intell., 1990. **12**(1): p. 55-73.

21. Carter, P.H., *Texture discrimination using wavelets.* SPIE Applications of Digital Image Processing XIV, 1991. **1567**: p. 432-438.

22. Jain, A.K. and F. Farrokhnia, *Unsupervised Texture Segmentation Using Gabor Filters.* Pattern Recognition, 1991. **24**(12): p. 1167-1186.

23. Laine, A. and J. Fan, *Texture Classification by Wavelet Packet Signatures.* IEEE Trans. Pattern Anal. Machine Intell., 1993. **15**(11): p. 1186-1191.

24. Manjunath, B.S. and W.Y. Ma, *Texture Features for Browsing and Retrieval of Image Data.* IEEE Trans. Pattern Anal. Machine Intell., 1996. **18**(8): p. 837-842.

25. Azencott, R., J.-P. Wang, and L. Younes, *Texture Classification Using Windowed Fourier Filters.* IEEE Trans. Pattern Anal. Machine Intell., 1997. **1997**(2): p. 148-153.

26. Schulerud, H. and J.M. Carstensen. *Multiresolution Texture Analysis of four classes of Mice Liver cells using different cell cluster representations.* in *Proceedings of 9th Scandinavian Conference on Image Analysis.* 1995. Uppsala, Sweden.

27. Bamford, P. and B. Lovell. *Improving the robustness of cell nucleus segmentation.* in *Proceedings of the Nineth British Machine Vision Conference.* 1998. Southampton, UK.

28. Snider, R.S. and J.C. Lee, *A Stereotaxic Atlas of the Monkey Brain.* 1961, Chicago, Illinois: The University of Chicago Press.

29. Raphan, T. and B. Cohen, *How does the vestibulo-ocular reflex work?*, in *Disorders of the vestibular system*, R.W. Baloh and G.M. Halmagyi, Editors. 1996, Oxford University Press. p. 20-47.

30. Szentagothai, J., *The elementary vestibulo-ocular reflex arc.* J. Neurophysiol., 1950. **13**: p. 395-407.

31. Cohen, B., V. Matsuo, and T. Raphan, *Quantitative analysis of the velocity characteristics of optokinetic nystagmus and optokinetic after-nystagmus.* J. Physiol. (Lond.), 1977. **270**: p. 321-344.

32. Raphan, T., V. Matsuo, and B. Cohen, *Velocity storage in the vestibulo-ocular reflex arc (VOR).* Exp. Brain Research, 1979. **35**: p. 229-248.

33. Cohen, B., *The vestibulo-ocular reflex arc*, in *Handbook of Sensory Physiology. Vestibular System. Basic Mechanisms*, H.H. Kornhuber, Editor. 1974, Springer-Verlag: Berlin. p. 477-540.

34. Yokota, J.I., H. Reisine, and B. Cohen, *Stimulation of the vestibular nuclei and the nucleus prepositus hypoglossi.* Soc. Neurosci. Abstr, 1991. **17**: p. 314.

35. Reisine, H. and T. Raphan, *Neural basis for eye velocity generation in the vestibular nuclei during off-vertical axis rotation.* Exp. Brain Res., 1992. **92**: p. 209-226.

36. Fuchs, A.F. and J. Kimm, *Unit activity in the vestibular nucleus of the alert monkey during horizontal angular acceleration and eye movement.* J. Neurophysiol., 1975. **38**: p. 1140-1161.

37. Wearne, S., T. Raphan, and B. Cohen, *Nodulo-uvular control of central vestibular dynamics determines spatial orientation of the angular vestibulo-ocular reflex (aVOR).* Ann. N.Y. Acad. Sci., 1996. **781**: p. 364-384.

38. Wearne, S., T. Raphan, and B. Cohen, *Control of Spatial Orientation of the Angular Vestibuloocular Reflex by the Nodulus and Uvula.* J. Neurophysiol, 1998. **79**: p. 2690-2715.

39. Büttner-Ennever, J.A., A.K.E. Horn, and K. Schmidtke, *Cell Groups of the Medial Longitudinal Fasciculus and Paramedian Tracts.* Rev. Neurol., 1989. **145**(8-9): p. 533-539.

40. Büttner-Ennever, J.A., ed. *Paramedian tract cell groups: A review of connectivity and oculomotor function.* Vestibular and Brain Stem Control of Eye-Head and Body Movements, ed. H. Shimazu and Y. Shinoda. 1992, Japan Scientific Societies Press: Tokyo. 323-330.

41. Büttner-Ennever, J.A. and A.K.E. Horn, *Pathways from cell groups of the paramedian tracts to the floccular region.* N.Y. Acad. Sci., 1996. **781**: p. 532-540.

42. Büttner-Ennever, J.A. and U. Büttner, *The reticular formation*, in *Neuroanatomy of the Oculomotor System*, J.A. Büttner-Ennever, Editor. 1988, Elsevier Science Publishers: Amsterdam. p. 119-176.

43. Belknap, D.B. and R.A. McCrea, *Anatomical Connections of the Prepositus and Abducens Nuclei in the Squirrel Monkey.* The Journal of Comparative Neurology, 1988(268): p. 13-28.

44. IEEE Standard 610.4, *IEEE Standard Glossary of Image Processing and Pattern Recognition Terminology*, . 1990, IEEE Press: New York.

45. Haralick, R.M., *Statistical and Structural Approaches to Texture.* Proceedings of IEEE, 1979. **67**(5): p. 786-804.

46. Wechsler, H., *Texture analysis - A survey.* Signal Processing, 1980. **2**: p. 271-282.

47. van Gool, L.J., P. Dewaele, and A. Oosterlinck, *Texture Analysis Anno 1983.* Computer Vision Graphics and Image Processing, 1985. **29**(3): p. 336-357.

48. Tuceryan, M. and A.K. Jain, *Texture Analysis.* Handbook of Pattern Recognition and Computer Vision, 1993. **II-1**: p. 235-276.

49. Randen, T. and J.H. Husoy, *Filtering for Texture Classification: A Comparative Study.* IEEE Transactions on Pattern Analysis and Machine Intelligence, 1999. **21**(4): p. 291-310.

50. Lu, S.Y. and K.S. Fu, *A syntactic approach to texture analysis.* CGIP, 1978. **7**(3): p. 303-330.

51. Nalwa, V.S., *A Guided Tour of Computer Vision.* 1993: Addison-Wesley. 361.

52. Julesz, B., *Visual Pattern Discrimination.* IRE Transactions on Information Theory, 1962. **IT-8**(2): p. 84-92.

53. Haralick, R.M., K. Shanmugam, and I. Dinstein, *Textural Features for Image Classification.* IEEE Transactions on Systems, Man, and Cybernetics, 1973. **SMC-3**(6): p. 610-621.

54. Julesz, B., *Textons, the elements of texture perception, and their interactions.* Nature, 1981. **290**(12 March): p. 91-97.

55. Tsatsanis, M.K. and G.B. Giannakis, *Object and Texture Classification Using Higher Order Statistics.* IEEE Trans. Pattern Anal. Machine Intell., 1992. **14**(7): p. 733-750.

56. Swami, A., G.B. Giannakis, and J.M. Mendel, *Linear Modeling of Multidimensional non-Gaussian processes using cumulants.* Multidimensional Syst. Signal Processing, 1990. **1**: p. 11-37.

57. Lendaris, G.G. and G.L. Stanley, *Diffraction-Pattern Sampling for Automatic Pattern Recognition.* Proceedings of the IEEE, 1970. **58**(2): p. 198-216.

58. Patel, D. and T.J. Stonham. *Unsupervised/Supervised texture segmentation and its application to real-world data.* in *Visual Communications and Image Processing.* 1992. Boston , Massachusetts: SPIE.

59. Reed, T.R. and J.M.H. Du Buf, *A Review of Recent Texture Segmentation and Feature Extraction Techniques.* CVGIP: Image Understanding, 1993. **57**(3): p. 359-372.

60. Caelli, T., *Texture Classification and Segmentation Algorithms in Man and Machine.* Spatial Vision, 1993. **7**: p. 277-292.

61. Wang, Z.L., A. Guerriero, and M. Desario, *Comparison of Several Approaches for the Segmentation of Texture Images.* Pattern Recognition Letters, 1996. **17**(5): p. 509-521.

62. He, D.-C. and L. Wang, *Texture Unit, Texture Spectrum, and Texture Analysis.* IEEE Transactions on Geoscience and Remote Sensing, 1990. **28**(4): p. 509-512.

63. McCormick, B.H. and S.N. Jayaramamurthy, *A Decision Theory Method for the Analysis of Texture.* International Journal of Computer and Information Science, 1974. **3**: p. 329-343.

64. Manjunath, B.S. and R. Chellappa, *Unsupervised Texture Segmentation Using Markov Random Field MOdels.* IEEE Transactions on Pattern Analysis and Machine Intelligence, 1991. **13**(5): p. 478-482.

65. Pentland, A.P., *Fractal-based description of natural scenes.* IEEE Transactions on Pattern Analysis and Machine Intelligence, 1984. **6**(6): p. 661-674.

66. Chaudhuri, B.B. and N. Sarkar, *Texture Segmentation Using Fractal Dimension.* IEEE Transactions on Pattern Analysis and Machine Intelligence, 1995. **17**(1): p. 72-77.

67. Laws, K.I., *Textured Image Segmentation*, . 1980, Dept. of Elec. Eng., Image Processing Institute, Univ. of Southern California, Los Angeles.

68. Unser, M., *Local linear transforms for texture measurements.* Signal Processing, 1986(11): p. 61-79.

69. Hsiao, J.Y. and A.A. Sawchuk, *Unsupervised Textured Image Segmentation Using Feature Smoothing and Probabilistic Relaxation Techniques.* Computer Vision, Graphics, and Image Processing, 1989. **48**: p. 1-21.

70. Bajcsy, R. and L. Lieberman, *Texture gradient as a depth cue.* Comput. Graphics Image Processing, 1976. **5**: p. 52-67.

71. Reed, T.R. and H. Wechsler, *Segmentation of Textured Images and Gestalt Organization Using Spatial/Spatial-Frequency Representations.* IEEE Trans. Pattern Anal. Machine Intell., 1990. **12**(1): p. 1-12.

72. Daugman, J.G., *Two-dimensional spectral analysis of cortical receptive field profiles.* Vision Res., 1980. **20**: p. 847-856.

73. Marr, D., *Vision.* 1982: W. H. Freeman and Company. 397.

74. Dunn, D. and W.E. Higgins, *Optimal Gabor Filters for Texture Segmentation.* IEEE Transactions on Image Processing, 1995. **4**(7): p. 947-964.

75. Teuner, A., O. Pichler, and B. Hosticka, *Unsupervised Texture Segmentation of Images Using Tuned Matched Gabor Filters.* IEEE Transactions on Image Processing, 1995. **4**(6): p. 863-870.

76. Chang, T. and C.-C.J. Kuo, *Tree-Structured wavelet transform for textured image segmentation.* Proceedings of SPIE, 1992. **1770**: p. 394-405.

77. Greiner, T., *Orthogonal and biorthogonal texture-matched wavelet filterbanks for hierarchical texture analysis.* Signal Processing, 1996. **54**(1): p. 1-22.

78. Wang, J.W., *et al.*, *Texture classification using non-separable two-dimensional wavelets.* Pattern Recognition Letters, 1998. **19**(13): p. 1225-1234.

79. Unser, M., *Texture Classification and Segmentation Using Wavelet Frames.* IEEE Transactions on Image Processing, 1995. **4**(11): p. 1549-1560.

80. Chitre, Y. and A.P. Dhawan, *M-band wavelet discrimination of natural textures.* Pattern Recognition, 1999. **32**(5): p. 773-789.

81. Vautrot, P., N. Bonnet, and M. Herbin. *Comparative Study of Different Spatial/Spatial-Frequency Methods (Gabor Filters, Wavelets, Wavelets Packets) for Texture Segmentation/Classification.* in *International Conference on Image Processing.* 1996. Lausanne, Switzerland: IEEE.

82. Brodatz, P., *Textures: A Photographic Album for Artists and Designers.* 1966, New York: Dover.

83. Du Buf, J.M.H., M. Kardan, and M. Spann, *Texture Feature Performance for Image Segmentation.* Pattern Recognition, 1990. **23**(3/4): p. 291-309.

84. Young, R.K., *Wavelet theory and its applications*. 1993, Norwell, MA: Kluwer Academic Publishers. 223.

85. Chui, C.K., *An Introduction to wavelets*. 1992, Boston: Academic Press. 264.

86. Daubechies, I., *Ten Lectures on Wavelets*. 1992: the Society for Industrial and Applied Mathematics. 357.

87. Daubechies, I., ed. *Different Perspectives on Wavelets*. Proceedints of Symposia in Applied Mathematics. Vol. 47. 1993, American Mathematical Society: Providence, Rhode Island. 205.

88. Strang, G. and T. Nguyen, *Wavelets and Filter Banks*. 1996, Wellesley, MA: Wellesley-Cambridge Press. 490.

89. Gabor, D., *Theory of communication*. J. Inst. Electr. Eng., 1946. **93**: p. 429-457.

90. Daugman, J.G., *Uncertainty relation for resolution in space, spatial-frequency, and orientation optimized by two-dimensional visual cortical filters*. J. Opt. Soc. Am., 1985. **2**: p. 1160-1169.

91. Javid, M. and E. Brenner, *Analysis, transmission and filtering of signals*. 1963, New York: McGraw-Hill. 462.

92. Malik, J. and P. Perona, *Preattentive texture discrimination with early vision mechanisms*. Journal of the Optical Society of America, 1990. **7**(5): p. 923-932.

93. Campbell, F.W. and J.G. Robson, *Application of Fourier analysis to the visibility of gratings*. J. Physiol., 1968. **197**: p. 551-566.

94. Rumelhart, D.E., J.L. McClelland, and P.R. Group, *Parallel Distributed Processing: Explorations in the microstructures of cognition*. Vol. 1 and 2. 1986, Cambridge, Mass: MIT Press. 1-12.

95. Jain, A.K. and R.C. Dubes, *Algorithms for clustering data*. 1st ed. Prentice Hall advanced reference series, Computer Science. 1988, Englewood Cliffs, New Jersey: Prentice-Hall, Inc. 320.

96. Rosenfeld, A., ed. *Multiresolution image processing and analysis*. Springer series in information sciences; 12. 1984, Springer-Verlag: New York. 385.

97. Davis, L.S. and A. Rosenfeld, *Cooperating Processes for Low-level Vision: A Survey*. Artificial Intelligence, 1981. **17**: p. 245-263.

98. Rosenfeld, A., R. Hummel, and S. Zucker, *Scene labeling by relaxation algorithms*. IEEE Trans. Systems Man Cybernet., 1976. **SMC-6**: p. 420-433.

99. Hsiao, J.Y., *Textured Image Segmentation Using Feature Smoothing and Probabilistic Relaxation Techniques*, 1987, Univ. of Southern California: Los Angeles.

100. Peleg, S., *A new probabilistic relaxation scheme.* IEEE Trans. Pattern Anal. Mach. Intell., 1980. **PAMI-2**: p. 362-369.

101. Lanyon, L.E., *Analysis of surface bone strain in the calcaneus of sheep during normal locomotion. Strain analysis of the calcaneus.* J. Biomech., 1973. **6**: p. 41-49.

102. Oxnard, C.E., *Bone and Bones, Architecture and Stress, Fossils and Osteoporosis.* Journal of Biomechanics, 1993. **26**(1): p. 63-79.

103. Tou, J.T. and R.C. Gonzalez, *Pattern recognition principles*. 2nd ed. Applied Mathematics and Computation, ed. R. Kalaba. 1974, Reading, Massachusetts: Addison-Wesley Publishing Company. 377.